INFORMATION TO USERS

This manuscript has been reproduced from the microfilm master. UMI films the text directly from the original or copy submitted. Thus, some thesis and dissertation copies are in typewriter face, while others may be from any type of computer printer.

The quality of this reproduction is dependent upon the quality of the copy submitted. Broken or indistinct print, colored or poor quality illustrations and photographs, print bleedthrough, substandard margins, and improper alignment can adversely affect reproduction.

In the unlikely event that the author did not send UMI a complete manuscript and there are missing pages, these will be noted. Also, if unauthorized copyright material had to be removed, a note will indicate the deletion.

Oversize materials (e.g., maps, drawings, charts) are reproduced by sectioning the original, beginning at the upper left-hand corner and continuing from left to right in equal sections with small overlaps.

Photographs included in the original manuscript have been reproduced xerographically in this copy. Higher quality 6" x 9" black and white photographic prints are available for any photographs or illustrations appearing in this copy for an additional charge. Contact UMI directly to order.

ProQuest Information and Learning
300 North Zeeb Road, Ann Arbor, MI 48106-1346 USA
800-521-0600

Advanced Diffraction and Wave Propagation Models for Characterization of Wireless Communication Channels

by

Il-Suek Koh

A dissertation submitted in partial fulfillment
of the requirements for the degree of
Doctor of Philosophy
(Electrical Engineering)
in The University of Michigan
2002

Doctoral Committee:

Professor Kamal Sarabandi, Chair
Associate Professor Brian Gilchrist
Emeritus Professor Thomas B.A. Senior
Professor Wayne E. Stark
Research Scientist M. D. Casciato

ProQuest Information and Learning Company
300 North Zeeb Road
P.O. Box 1346
Ann Arbor, MI 48106-1346

To my parents and wife

ACKNOWLEDGEMENTS

First I would like to acknowledge my parents, JaeWoo Koh, and YoungNim Kim, and my wife, Myungsin Song, for their support and encouragement during my Ph.D study. Also I'd like to acknowledge my academic advisor, Prof. Kamal Sarabandi, for his guidance and mentorship, and all of my committee members for their suggestions. I'd like to thank Mark D. Casciato for his kind help and proofreading of this thesis, and Leland Pierce for his help for computer problems. I'd like to thank my Korean friends, especially Yongshik Lee, and radlab students and staff for their help and support. Finally I'd like to thank and acknowledge National Science Foundation for their support, without which this project would have not been possible (contract ECS-9979376).

TABLE OF CONTENTS

LIST OF TABLES

LIST OF FIGURES

LIST OF APPENDICES

Appendix

CHAPTER 1

Introduction

Over the past two decades telecommunication has experienced significant changes, and its paradigm has moved from wire to wireless communications. Unlike other technologies that have had a significant effect on human life style, such as the personal computer or internet, wireless communications have penetrated into the general public irrespective of age or social class. The idea of wireless communications itself is quite old and its theoretical foundation can be dated back to 1678 when Huygens discovered the phenomena of light reflection and refraction. After that, many scientists tried to build a governing equation for electrical and magnetic phenomena in vain. Finally in 1865 Maxwell established his famous equations and from these predicted the existence of electromagnetic waves. Hertz showed the feasibility of transmitting and detecting an electomagnetic wave and so proved the theoretical conjecture. After Hertz's historical experiment Marconi created a radio that could communicate between two points up to 3km apart in 1896. In the beginning of the 20th century, in 1901, Marconi successfully transmitted Morse code for the letter S across the Atlantic Ocean using very low frequency (< 1MHz).

The size of the transmitter and receiver required prohibited an immediate spread of the new technology. After the second World War, with the development of new technologies, the size restraints had been reduced considerably, and wireless radio communications were available for general civilian use (business, health care, etc.). Until the first commercial

analog cellular network was built in 1980, based on the Advanced Mobile Phone Service (AMPS), the general public did not have access to wireless technology. During the 1980s, several countries introduced their own analog system, such as Scandinavia's Nordic Mobile Telephone (NMT), Japan's High Capacity Mobile Telephone System (HCMTS), France's Radicom 2000, etc.. However since cellular phone service was expensive, unstable, and the number of subscriber s supported by the technology (based on an analog modulation scheme) was very limited, the mobile phone was not very popular.

True evolution of wireless systems in all senses has occurred during the 1990s. For example the wireless communication market grew by approximately 70% in Western Europe, 50% in Northern American, 55% in Asia and more than 200% in the largest Latin American countries during one year, 1997. This kind of growth may have been a result of the second-generation (2G) service, launched during the 1990s. The 2G system has different features from the first-generation system (analog cellular system) which are summarized below [1].

1. Use of digital modulation which provides robustness of signal (acceptance of lower C/I ratio than analog frequency modulation), a higher capacity, and better compatibility with modern digital fixed infrastructure.

2. Two frequency bands (800 and 900 MHz, 1.8 and 1.9 GHz) which can reduce the size of systems.

3. Near standardization with Global System for Mobile communications (GSM) which allows service providers to be able to purchase equipment from several manufacturers, and so enhances the management of roaming and handover.

4. Use of multiplexing schemes such as Time Division Multiple Access (TDMA), and Code Division Multiple Access (CDMA) which increases capacity.

Using the 2G system, limited data communications like two way text transmission are possible over the voice channel. However data communication in a strict sense is achieved

in the third-generation (3G) system that has recently been standardized, and currently services Japan based on WCDMA (Wideband CDMA) and a technology called cHTML (Compact HyperText Markup Language). Key features of 3G system are

1. A high degree of commonality of design, worldwide.
2. Compatibility of service with fixed networks .
3. High quality .
4. Use of small pocket-terminals with worldwide roaming capability.
5. Capability for multimedia applications, and a wide range of services like paging, voice telephony, digital data, audio and visual communications

To achieve these goals the target bit rates are 144kb/s or higher in high mobility (vehicular) traffic, 386kb/s or higher in slow mobility, and 2Mb/s or higher for indoor traffic. The most important improvement in the 3G system over the 2G system is usage of packet-switched connections including the internet protocol (IP), which means a 3G terminal is virtually always connected to the fixed network. For this purpose many schemes have been proposed by various groups including Bluetooth and Wireless Application Protocol (WAP) for WCDMA. Additionally there are two more major trends that are supported by Microsoft, and NTT DoCoMo. These two schemes are extended from the traditional HTML technology used in the wire internet to implement wireless data communications.

Another main motive force for development of advanced wireless communications systems comes from military needs. According to the doctrine adopted by the Army for Future Combat Systems (FCS), reliable and secure wireless data communications are essential among a heterogeneous mixture of soldiers, ground vehicles, manned and unmanned airborne platforms, robotics, and unattended networks of microsensors. For this purpose it is very clear that low power, very reliable, high data rate, and hence wideband communica-

tions are required. Unlike commercial communications, this type of military communications will be generally established in a more harsh environment, like a deep woods.

The wireless network is different from the fixed network in a following senses [1].

1. Limited spectrum which is determined by national and international regulations. To support an increasing number of subscribers more advanced techniques are required like more spectrally efficient modulation schemes, source compression coding, etc..

2. Fluctuating quality of radio links that is caused by movement of users or changes in environment (moving scatterers, various types of interferers), i.e., channel characteristics.

3. Unknown and various access points.

Characteristics of a communication channel as well as various communication techniques have a significant effect on the performance of a communications system. Therefore accurate prediction of radio wave propagation in a communication channel is essential in the development and design of advanced wireless communication systems. To assess performance of advanced communication systems and complex modulation schemes, information about the wireless channel over wide frequency range is required. A wideband channel model should estimate accurately various properties of a communication channel including deterministic characteristics such as path-loss (mean-field), and also statistical properties like coherency, field variations, short- or long-term fading due to multi-path, dispersive (path delay) effects, etc.. Current channel models for urban and rural areas are heuristic in nature, and give only narrow-band properties. Therefore they have limited applicability for a modern wireless communication networks such as 3G communication, wireless LAN, Wireless Local Loop (WLL), etc., or even simple digital voice communication.

Commonly used channel models can be categorized into two main groups: 1) deterministic, and 2) statistical [2, 3, 4, 5]. The deterministic models are developed based on

extensive narrow-band measurements or basic electromagnetic wave theory and are generally used for the prediction of path-loss. The statistical models are based on statistics derived from measurements or some non-physical assumptions. As an example of this, some current channel models are assumed to be an assembly of independent scatterers that are not affected by the existence of other scatterers, and the locations of these scatterers are randomly distributed for a simplicity of analysis [3]. Some of general statistical properties of a channel can be derived from assuming simple probability density functions (PDF), for example spatial correlation statistics can be derived by known fading distributions such as log-normal, Rayleigh, Rice, or Nakagami distribution [6, 7]. However, there may be no clear criterion of choosing a proper PDF for a given channel. Choice of a PDF for fading estimation, for example, is usually done based on experience and some heuristic and qualitative methods. But this may not be always be possible: for example in an environment like a subway tunnel, conventional PDFs for fading statistics don't fit well with measured results over the entire comparison region [8]. However ray-tracing techniques, which account for physical location and size of scatterers within a channel, can generate results which are in good agreement with measured data.

1.1 Existing Channel Models & Their Limitation

1.1.1 Rural Areas

The most important issue with regard to modeling of wave propagation in rural environments is the interaction of electromagnetic waves with vegetation. Tree stands can affect radio wave propagation significantly, due to strong scattering and absorption, which are dependent on the frequency, bandwidth, and propagation path length through the vegetation. In the 1960s and 1970s a deterministic model of wave propagation in a forest environment was introduced by Tamir [9]. This model described the absorption and diffraction effects of vegetation when a transmitter and receiver are within the tree stand. Trees are modeled as

a homogeneous dielectric slab above a dielectric half-space (three-layered model) that is a good approximation for a forest up to 500MHz. This model was later modified noting that the effective dielectric constant of the crown layer is different from that of the trunk layer and the fact that these layers are anisotropic dielectrics, due to the preferred orientation of the vegetation components of tree structures. At these frequencies a four-layered model, introduced by Cavalcante in 1983, is used to predict the path-loss [10]. In the four-layered model, the crown and trunk layer are modeled by anisotropic media with different dielectric tensors, respectively. The three- and four- layered models can predict only path-loss and cannot provide the complete characteristics of the propagation channel. Both of these models assume a dielectric slab with a planar boundary ignoring the rough canopy-air interface that appears in nature. Since at frequencies higher than 500MHz, the dimensions of tree structures are comparable to or larger than the wavelength, diffuse scattering in the canopy and trunk layers far exceeds the mean-field due to higher attenuation caused by scattering extinction. Hence the models which predict only mean-field are of little use. An empirical model, proposed by Weissberger is based on available measured data and some simplified theoretical predictions, but can only predict path-loss [11]. A theoretical stochastic model for one tree was introduced by Torrico *et al.* [12, 13], based on analytical wave theory to predict the effect of a tree on radio wave propagation in residential environments. In this model the crown of the tree is modeled as an ellipsoidal region containing branches and leaves which are assumed to be randomly located inside the crown region. From the assumed geometry, the mean field emerging from the crown layer of a tree is calculated. Torrico's model differs from the previously mentioned models, in that it can estimate field fluctuations. Its accuracy however is questionable since the assumed geometry is unlike real tree structures.

1.1.2 Urban Areas

One of the more well known deterministic models for urban environments is the Okumura-Hata model, which Hata developed by applying a curve fitting algorithm to measured data for Tokyo, taken by Okumura[4]. The model is a simple algebraic equation, which is a function of operating frequency, distance between transmitter and receiver, and relative transmiter/receiver heights and can be used for the prediction of path-loss at 1.5 to 2GHz. It is very obvious that the Okumura-Hata model cannot generate information such as coherence bandwidth, depolarization, etc., which are necessary in order to completely characterize the communication channel. Since the model is independent of regional planning in a city, several researchers have extended this model to include the effects of heights and locations of buildings, by introducing a loss factor between transmitter and receiver [3, 14]. This loss factor is generally calculated based on measurements and again non-physical assumptions. For example, this model assumes that waves encountering a building go around the building to reach the receiver beyond it, to include extended path length [14].

These types of simple models including general statistical models cannot accurately estimate the phenomena of radio wave propagation in urban environments, as they are not based on the physics of the problem [2]. For example the received fields in an urban environment, at heights lower than roof level, are mainly caused by radio waves reflected from wall and/or diffracted around corners. However all of the described models inherently ignore these kinds basic physical mechanisms and hence fail to give the model the fidelity needed to accurately predict propagation in urban environments. In more recent literature, techniques to rigorously analyze this kind of phenomena, and based on physical optics and geometrical optics, have been applied. One of these models is a combination of ray-tracing and the Uniform Theory of Diffraction (UTD) which is currently in wide use [2, 3, 4, 15], and can predict path-loss and statistical properties of the channel using Monte Carlo simulations. The combination was applied successfully to 2D channel estimation but it becomes very inefficient for a 3D problem. A major reason for this inefficiency is that

in a 3D problem, the complexity of the search algorithm of all possible paths from transmitter to receiver increases very rapidly. This method also assumes that the buildings are impenetrable and have smooth surfaces which again is not physical. It is well known that the reflection coefficient from a non-smooth building surface is substantially smaller than that of a smooth surface. Hence these kind non-physical assumptions make the accuracy of this method degenerate. UTD was originally designed for a perfect electrical conducting (PEC) wedge diffraction problem and so its accuracy degenerates when applied to a lossy dielectric diffraction problem. Recently another hybrid technique was proposed to remedy these problems. It is a combination of ray-tracing and finite difference time domain method (FDTD) techniques [16]. This method was applied to the 2D indoor propagation problem. It is doubtful, however, that FDTD can be applied to an electrically large problem since FDTD is so computationally extensive.

1.2 Motivation & Approach

As explained in the previous section, traditional methods for modeling propagation lack the fidelity to generate fully sufficient information about a wireless communication channel. This deficiency is due to the fact that these existing models are not based on the physics of the problem to be solved and therefore are not suitable for the performance assessment of a communication system. A method is required, more directly based on the physical mechanisms of propagation and which sufficiently accounts for propagation mechanisms such as reflection, diffraction, and attenuation in the propagation environments. With this as a motivation a more rigorous approach, based on the physics of the problem, is applied in this thesis work. This physics-based methodology is different from the previously mentioned models in that it predicts the fields based on site-specific information such as real terrain data, dimensions of buildings, walls, forests and so on.

1.2.1 Approach: Forested Environment

As mentioned earlier, a commonly used propagation model in an urban area is the combination of the ray-tracing technique and UTD. However in forested environments this method can't be applied due to the complexity of tree structures. Also, a point to point link where both transmitter and receiver are embedded in the forest (ground-to-ground scenario) requires a somewhat different approach from the case of one radio, either transmitter or receiver, external to the forest, especially above the forest (air-to-ground scenario) and in this thesis two models are developed in order to characterize both scenarios. Due to the severe attenuation in the highly scattering environment of a forest, ground-to-ground communication over some distance can only be achieved at UHF frequencies or lower (say $f < 500MHz$). For this point-to-point communication within a forest, (a receiver and a transmitter both are embedded in the forest), a lateral wave propagates along the canopy-air interface and is the most dominant contributor to distant communication. The tree trunks, which are comparable to a wavelength, contribute mainly to field fluctuations. Hence, the basic model for a forest is that of a dielectric slab representing the canopy, in which cylinders, representing the tree trunks are embedded. Interactions among the tree trunks are calculated by applying the Method of Moments (MoM) numerical solution. The roughness of the canopy-air interface is accounted for by applying the distorted Born approximation. Results show that roughness of the canopy-air interface can result in additional attenuation of up to 5dB in the lateral wave component of the received field. For the second case, that of either transmitter or receiver external to the forest, the proximity of a radio to the tree trunks and large lower branches is the main cause of field fluctuations. To accurately estimate this fluctuation, tree shape should be considered in an exact manner because the radio terminal may be very close to the trees. Mathematically, the most suitable way to model a tree structure is by using a fractal geometry technique [17]. As is obvious, the application of any numerical method to this kind of large, and complex structure will be very inefficient. Therefore, by applying a fractal tree model and single scattering theory a

coherent channel model for this scenario can be developed. To obtain the desired statistics, Monte Carlo simulation is used to vary the tree position, size, and basic structure (position of branches etc.). This model is applicable through mm-wave, provided details of the forest, which become electrically large at higher frequencies, are accounted for.

1.2.2 Approach: Urban Environments

For urban areas, and as mentioned earlier, ray-tracing technique may be inaccurate. At low frequencies the assumptions made about impenetrable scatterers result in some considerable errors and at high frequency the effect of building surface roughness must be accounted for. In order to more accurately represent an urban environment a MoM technique may be applied. MoM is an integral equation technique which requires knowing the Green's function or system transfer function of the problem and MoM usually has two major disadvantages. The first is that as the problem size increases the problem in terms of computer resources becomes intractable. The second is the difficulty of computation of the Green's function in the presence of a dielectric half space. This Green's function contains Sommerfeld type integrals which are difficult to evaluate numerically. To circumvent this problem an integral transform technique known as Exact Image theory is applied for an impedance half-space. The assumption of an impedance half-space is an acceptable one for a highly-lossy ground, and the Exact Image technique transforms the Sommerfeld type integrals into a form that is highly efficient for numerical computation. To alleviate the inherent problem with MoM in terms of object size, more efficient numerical methods such as Fast Multipole Method (FMM), Adaptive Integral Method (AIM), etc. can be applied in order to reduce the complexity of the traditional MoM formulation. In this thesis, a new FMM identity for a half-space medium using the exact image theory expressions for the Green's function is formulated in order to apply an FMM algorithm to the problem of an object (buildings, etc.) above an impedance surface.

1.3 Relevant Assumptions

In this thesis the convention of $e^{-j\omega t}$ is assumed, and suppressed throughout the thesis. For the forest models, the biophysical structure of individual components of a tree are summarized in [18]. Also tree trunks, branches, and twigs are modeled as circular finite dielectric cylinders with a smooth surface. Leaves are modeled as a thin dielectric disk. Empirical formulations for the dielectric constant of these objects are found in [19]. The ground plane, for the forest models, is approximated by a dielectric half-space with a smooth boundary whose dielectric constant is calculated from a formula given in [19].

1.4 Thesis Outline

This thesis is composed of 7 chapters that deal with different problems encountered in physic-based channel modeling. In the next two chapters a model for point-to-point communication, in which both transmitter and receiver are embedded in the forest environment, is developed. In Chapter 2 the problem of VHF-UHF wave propagation in forested environments is considered. Using the model, the mean-field can be accurately calculated, and the effect of the roughness of the air-canopy interface included. An analytic expression of the mean-field and its asymptotic expression are formulated, which are based on the distorted Born approximation. In Chapter 3 a complete channel model for a forest at HF-UHF band is introduced. This model provides for an efficient and fast solution for the characterization of a forested environment including all field statistics. Desired statistics are calculated based on Monte Carlo simulation for a single antenna and then extended to antenna arrays. A non-uniform sampling scheme is proposed which converts a wideband frequency-domain response to time-domain with a minimum number of samples. As an application of this model, performance of antenna diversity schemes is also assessed. In Chapter 4 a model is developed for the scenario of either transmitter or receiver external to the forest. As explained, the model is based on a fractal geometry for an accurate description of trees,

and single scattering theory. This model is applied to determine the characteristics of wave propagation in two types of forests, coniferous and deciduous. The model is fully polarimetric and determines both mean-field and field fluctuations at the receiver. Applying this simulation, performance of a GPS system under tree canopies is assessed. In addition the ultra-wideband responses of a forest is also investigated. To show the applicability of these developed models for assessment of a communication system in a realistic scenario, a novel hierarchical modulation scheme is proposed for ultra-wideband communications. Performance of this proposed system is assessed for the case of a transmitter and receiver, both embedded inside a forest, and compared with that of an impulse radio system in Chapter 5. In Chapter 6 an FMM identity based on a simplified form of the exact image method is formulated. This simplified form of the exact image expressions is derived in Appendix D. Finally cosite interference in a CDMA system is simulated in a simple environment, where channel characteristics are calculated by the conventional moment method. Figure 1.1 outlines this thesis in a simple block diagram.

In Chapter 7 this thesis work is summarized and conclusions are drawn as well as suggestions for future work.

Figure 1.1: Outline of thesis

CHAPTER 2

Estimation of Mean-field for HF-VHF Wave Propagation in a Rural Environment

2.1 Introduction

It is well known that at HF through VHF frequencies the propagation between two distant points within a forest experiences significantly less attenuation than that predicted by direct path field calculation. That is the predicted attenuation of the direct wave far exceeds the attenuation values obtained from experimental results. A very interesting model was first developed by Tamir [9] which describes the phenomena and attributes the wave propagation in forest to lateral wave. In this approach, the forest is modeled by a homogeneous half-space dielectric medium with a planar interface and a permittivity equal to the effective dielectric constant of the foliage medium. This effective dielectric constant can be obtained using a dielectric mixing formula [20] or the formulation for calculation of propagation constant in random media [21, 22, 23]. The former is appropriate for low frequencies when typical dimensions of the constitutive particles are small compared to the wavelength whereas the latter is useful for sparse media and accounts for scattering losses. Tamir's formulation gives the field of dipole within the effective medium at an observation point near the interface using an asymptotic integral evaluation [24, 25]. This solution

shows that the field at the observation point is dominated by a ray emanated from the source point and traveled in the direction of the critical angle toward the interface and along the interface before leaving it in the direction of critical angle, in order to reach the observation point.

Due to renewed interest in wireless communications at HF through UHF, recently the problem of wave propagation in forested areas has gained some prominence. The effective dielectric model for canopy is believed to be valid below 500MHz where the dimensions of leaves and branches are smaller than a wavelength. At higher frequencies significant volume scattering takes place and the mean field is no longer dominant. The original Tamir's model is extended in [26, 27, 28] by representing the forest by a two-layer anisotropic dielectric medium. These models account for the anisotropy that exists in the trunk layer and to a much lesser extent in the canopy layer. It is shown that up to UHF(assuming the dielectric model is valid) the effect of anisotropy can be ignored [26].

In reality, the interface between forest canopies and air is not flat, hence it is not clear whether the lateral wave can be excited and if it can, how the surface roughness affects it. In this chapter, the effect of roughness of interface between canopy and air on the wave propagation in forested area is investigated. In Section 2.2, analytical formulation using the volumetric integral equation in conjunction with the distorted Born approximation is presented. An expression for the mean-field of an infinitesimal dipole of arbitrary orientation is derived by obtaining a partial second order solution of the distorted Born approximation. In Section 2.3, a sensitivity analysis is carried out to demonstrate the variations of the mean-field to physical parameters such as a effective permittivity, location of the dipole and observation points, and surface roughness.

2.2 Analytical Formulation

In this section, an analytical formulation for the evaluation of mean field generated by a small dipole in a homogeneous half-space dielectric medium with rough interface is derived. The effective permittivity of forest canopies is slightly higher than that of free space since the vegetation particle density is very low [9]. In this case, distorted Born approximation may be used to evaluate the scattered fields. The geometry of the diffraction problem is shown in Fig.2.1 where the dipole and the observation point are respectively located at h and h' inside a canopy with an effective dielectric constant ε_1. The envelope

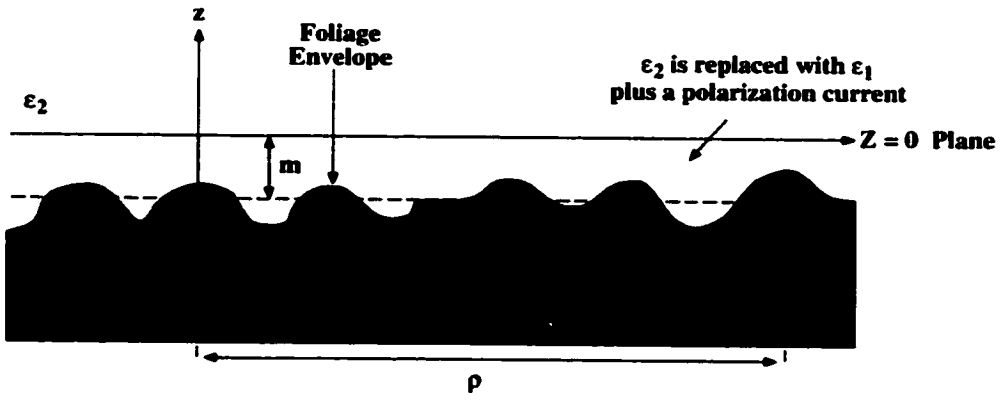

Figure 2.1: A short dipole embedded in a forest canopy with rough interface modeled by an effective dielectric constant ε_1. A layer above the canopy is, equivalently, replaced with a dielectric slab with planar interface(z = 0 plane) and permittivity ε_1 in addition to a polarization current, $\vec{\mathbf{J}} = ik_1 Y_1(\varepsilon_2 - \varepsilon_1)\vec{\mathbf{E}}^t$.

of the canopy-air interface is denoted by a random process, $d(x,y)$. The permittivity of the upper medium(air) is denoted by ε_2. We modify the problem by extending the canopy to z = 0 plane and assume that in this region, there exists a volumetric polarization current, $\vec{\mathbf{J}} = ik_1 Y_1(\varepsilon_2 - \varepsilon_1)\vec{\mathbf{E}}^t$, where $\vec{\mathbf{E}}^t = \vec{\mathbf{E}}^i + \vec{\mathbf{E}}^r + \vec{\mathbf{E}}^s$. The unknown total internal field can be obtained from the following integral equation

$$\vec{\mathbf{E}}^t(\vec{r}) = \vec{\mathbf{E}}^i(\vec{r}) + \vec{\mathbf{E}}^r(\vec{r}) + k_0^2(\varepsilon_2 - \varepsilon_1)\int_{-\infty}^{\infty}\int_{-\infty}^{\infty}\int_{-d(x,y)}^{0} \bar{\bar{G}}(\vec{r},\vec{r}')\vec{\mathbf{E}}^t(\vec{r}')dx'dy'dz'$$

where $\vec{\mathbf{E}}^i$ is the incident field, $\vec{\mathbf{E}}^r$ is the reflected wave from the planar interface(z = 0), and $\vec{\mathbf{E}}^s$ is the scattered field generated by $\vec{\mathbf{J}}$ itself and $\bar{\bar{G}}$ is the dyadic Green's function of the half space dielectric medium(see (2.4) [29, 30]).

To the first order in $(\varepsilon_2 - \varepsilon_1)$, the distorted Born approximation can be used to find the scattered field

$$\vec{\mathbf{E}}^s \approx k_0{}^2(\varepsilon_2 - \varepsilon_1)\int_{-\infty}^{\infty}\int_{-\infty}^{\infty}\int_{-d(x,y)}^{0}\bar{\bar{G}}(\vec{r},\vec{r}')\cdot[\vec{\mathbf{E}}^i(\vec{r}')+\vec{\mathbf{E}}^r(\vec{r}')]dx'dy'dz' \tag{2.1}$$

In (2.1), $d(x,y)$ is a two dimensional random process describing the interface between the canopy and air and is assumed to be Gaussian with a mean value of m (a positive number) and a standard deviation of σ. Noting that the z-dependence of $\vec{\mathbf{E}}^i$ and $\vec{\mathbf{E}}^r$ are of the form of $e^{\pm jk_{2z}^i z'}$, where $k_{2z}^i = \sqrt{k_2^2 - k_x^{i\,2} - k_y^{i\,2}}$, the integration with respect to z' can be carried out analytically. This integration would result in an algebraic expression in terms of $d(x,y)$ which is amenable for the calculation of statistical average of $\vec{\mathbf{E}}^s$. It is shown that the distorted Born approximation provides a more accurate solution for $\vec{\mathbf{E}}^s$. In this approximation, a phase correction term is incorporated into the approximate expressions for the internal field to account for the difference in the propagation constant between the air and the canopy. The explicit expressions for the incident and reflected fields, including the appropriate phase correction terms for a plane wave illumination, are given by

$$\vec{\mathbf{E}}^i = \hat{\mathbf{P}}(k_{1z}^i)e^{j[k_x^i x' + k_y^i y' + k_{2z}^i z']}\cdot e^{j(k_{2z}^i - k_{1z}^i)m} \tag{2.2}$$

$$\vec{\mathbf{E}}^r = \hat{\mathbf{P}}(-k_{1z}^i)R_{v,h}e^{j[k_x^i x' + k_y^i y' - k_{2z}^i z']}\cdot e^{j(k_{2z}^i - k_{1z}^i)m} \tag{2.3}$$

where $\hat{\mathbf{P}}(k_{1z})$ is a unit vector indicating polarization of the incident wave ($\hat{\mathbf{P}} = \hat{\mathbf{v}}$ or $\hat{\mathbf{h}}$) and $R_{v,h}$ is the Fresnel reflection coefficient for vertical or horizontal polarization.

The unit horizontal and vertical polarization vectors are defined with respect to the plane

of incidence and given by

$$\hat{h}(k_{1z}) = \frac{\hat{k}_1^i \times \hat{z}}{|\hat{k}_1^i \times \hat{z}|}, \qquad \hat{h}(-k_{1z}) = \hat{h}(k_{1z})$$
$$\hat{v}(k_{1z}) = \hat{h}(k_{1z}) \times \hat{k}_1^i, \quad \hat{v}(-k_{1z}) = \hat{h}(k_{1z}) \times \hat{k}_1^r,$$

where $\hat{k}_1^r = \hat{k}_1^i - 2(\hat{k}_1^i \times \hat{z})\hat{z}$ denotes the direction of the reflected wave.

Since the layer thickness is not uniform, the phase correction terms in (2.3) and (2.3) are chosen for a layer with a uniform thickness m. The dyadic Green's function for the half-space dielectric medium when $z \leq z'$ (observation point inside the foliage) is given by [29, 30]

$$\bar{\bar{G}} = -\hat{z}\hat{z}\frac{\delta(\vec{r}-\vec{r}')}{{k_2}^2} + \frac{j}{8\pi^2}\int_{-\infty}^{\infty}\int_{-\infty}^{\infty} dk_x dk_y e^{j[k_x(x-x')+k_y(y-y')]}\frac{1}{k_{1z}}\left\{\hat{h}(-k_{1z})\left[R_h\hat{h}(k_{1z})\cdot e^{-jk_{1z}z'} + \hat{h}(-k_{1z})e^{jk_{1z}z'}\right] + \hat{v}(-k_{1z})\left[R_v\hat{v}(k_{1z})e^{-jk_{1z}z'} + \hat{v}(-k_{1z})e^{jk_{1z}z'}\right]\right\} e^{-jk_{1z}z} \tag{2.4}$$

After substituting (2.4) into (2.1), the integration with respect to z' is carried out analytically. After performing this integration, evaluation of $\langle \vec{E}^s \rangle$ is attempted which requires computation of terms like $\langle e^{\pm js_i d} \rangle$. Assuming a Gaussian p.d.f. for d, it can easily be shown that

$$\langle e^{js_i d} \rangle = \frac{e^{js_i m}}{2}\left[e^{-\frac{\sigma^2 s_i^2}{2}} erfc(-j\frac{\sigma s_i}{\sqrt{2}}) + e^{-\frac{\sigma^2 s_i^{*2}}{2}} erfc(j\frac{\sigma s_i^*}{\sqrt{2}})\right] \tag{2.5}$$

$$\langle e^{-js_i d} \rangle = \frac{e^{-js_i m}}{2}\left[e^{-\frac{\sigma^2 s_i^{*2}}{2}} erfc(-j\frac{\sigma s_i^*}{\sqrt{2}}) + e^{-\frac{\sigma^2 s_i^2}{2}} erfc(j\frac{\sigma s_i}{\sqrt{2}})\right] \quad i = 1,2 \tag{2.6}$$

where the complex variable s_i can be either $s_1 = k_{2z}^i + k_{1z}^i$ or $s_2 = k_{2z}^i - k_{1z}^i$, and $erfc(\cdot)$ is the complementary error function defined by [31]:

$$erfc(z) = 1 - \frac{2}{\sqrt{\pi}}\left[\int_0^{\alpha} e^{-t^2} dt + je^{-\alpha^2}\int_{-\beta}^{0} e^{t^2 + j2\alpha t} dt\right]$$

where $z = \alpha + j\beta$. Noting that $erfc(jx) = 1 - \frac{2}{\sqrt{\pi}} j \int_{-x}^{0} e^{t^2} dt$ for real x, it can readily be shown that $\langle e^{-js_i d} \rangle$ reduces to the more familiar expression, $\langle e^{-js_i d} \rangle = e^{-js_i m - \frac{\sigma^2 s_i^2}{2}}$.

The integration with respect to x' and y' can now be carried out analytically which results in $\delta(k_x - k_x^i) \cdot \delta(k_y - k_y^i)$. This, in turn, simplifies the integration with respect to k_x and k_y. The final result is a plane wave propagating along k_1^r. Hence the total field in medium 1 is the sum of two plane waves: 1) the reflected wave at the hypothetical planar interface at z = 0, and 2) the mean scattered field. In other words, to the first order in $k_0^2(\varepsilon_2 - \varepsilon_1)$,

$$\vec{\mathbf{E}}^t = \vec{\mathbf{E}}^r + \langle \vec{\mathbf{E}}^s \rangle \approx (R_{ref} + R_{Born}^{(1)}) e^{j[k_{1x}^i x + k_{1y}^i y - k_{1z}^i z]} \tag{2.7}$$

where R_{ref} is the Fresnel reflection coefficient for the hypothetical planar interface.

After some algebraic manipulations, the first order reflection coefficients (referenced to z = 0 plane) for the mean field are obtained and given by

$$\begin{aligned} R_{Born(v)}^{(1)} = \frac{(\varepsilon_2 - \varepsilon_1)}{2k_{1z}^i} \Bigg\{ & \frac{1}{s_1} (1 - R_v^2 + R_v^2 \langle e^{js_1 d} \rangle - \langle e^{-js_1 d} \rangle) \cdot \frac{k_\rho{}^2 - k_{1z}{}^2}{\varepsilon_1} \\ & + \frac{R_v}{s_2} (\langle e^{js_2 d} \rangle - \langle e^{-js_2 d} \rangle) k_0{}^2 \Bigg\} e^{js_2 m} \end{aligned} \tag{2.8}$$

$$\begin{aligned} R_{Born(h)}^{(1)} = \frac{k_0{}^2(\varepsilon_2 - \varepsilon_1)}{2k_{1z}^i} \Bigg\{ & \frac{1}{s_1} (1 - R_h^2 + R_h^2 \langle e^{js_1 d} \rangle - \langle e^{-js_1 d} \rangle) \\ & + \frac{R_h}{s_2} (\langle e^{is_2 d} \rangle - \langle e^{-js_2 d} \rangle) \Bigg\} e^{js_2 m} \end{aligned} \tag{2.9}$$

Close examination of $R_{Born}^{(1)}$ reveals that $R_{ref} + R_{Born}$ is accurate enough for horizontal polarization, but its accuracy is not sufficient for the vertical polarization incidence. The discrepancy is more obvious around the Brewster angle(θ_b) where it is found that $R_{Born(v)}^{(1)}(\theta_b) \neq 0$. To rectify this difficulty, higher order solutions must be obtained. This is accomplished by obtaining a partial second order solution for the vertical polarization. The second order

solution for $\vec{\mathbf{E}}^s$ is given by

$$\vec{\mathbf{E}}^{s(2)}(\vec{r}) = k_0^4(\varepsilon_2-\varepsilon_1)^2 \int_v \bar{\bar{G}}(\vec{r},\vec{r}') \cdot \left\{ \int_{v'} \bar{\bar{G}}(\vec{r},\vec{r}') \cdot [\vec{\mathbf{E}}^i(\vec{r}') + \vec{\mathbf{E}}^r(\vec{r}')] \right\} dv' dv \tag{2.10}$$

Using only $-\hat{z}\hat{z}\frac{\delta(\vec{r}-\vec{r}')}{k_z^2}$ term of the dyadic Green's function (see (2.4)) in the integrand of the inner integral, a partial second order solution is obtained.

$$\vec{\mathbf{E}}^{s(1.5)}(\vec{r}) = -k_0{}^2 \frac{(\varepsilon_2-\varepsilon_1)^2}{\varepsilon_2} \int_v \bar{\bar{G}}(\vec{r},\vec{r}') \cdot \left[\hat{z}\hat{z} \cdot (\vec{\mathbf{E}}^i(\vec{r}') + \vec{\mathbf{E}}^r(\vec{r}')) \right] dv' \tag{2.11}$$

The complexity of this integral is of the same order as that of (2.1) and the ensemble average of $\vec{\mathbf{E}}^{s(1.5)}$ can be obtained in a manner similar to what was used in computation of $\langle \vec{\mathbf{E}}^{s(1)} \rangle$. Including the partial second-order term, the reflection coefficient for the vertical polarization is modified as follows.

$$\begin{aligned} R_{Born(v)}^{(1.5)} = & \frac{(\varepsilon_2-\varepsilon_1)}{2k_{1z}^i \varepsilon_1} \left\{ \frac{R_v}{s_2} (\langle e^{js_2 d} \rangle - \langle e^{-js_2 d} \rangle) \cdot (\frac{\varepsilon_1}{\varepsilon_2} k_\rho{}^2 + k_{1z}^i{}^2) \right. \\ & \left. + \frac{1}{s_1} (1 - R_v^2 + R_v^2 \langle e^{js_1 d} \rangle - \langle e^{-js_1 d} \rangle) \cdot (\frac{\varepsilon_1}{\varepsilon_2} k_\rho{}^2 - k_{1z}^i{}^2) \right\} e^{js_2 m} \end{aligned} \tag{2.12}$$

where $k_\rho{}^2 = k_x^i{}^2 + k_y^i{}^2$. Now it can easily be shown that at Brewster angle where $R_v = 0$, $R_{Born(v)}^{(1.5)}$ vanishes also.

Having found an approximate analytical solution for a plane wave excitation, the solution for an infinitesimal dipole embedded within the foliage can be obtained by expanding the field of the dipole in terms of a continuous angular spectrum of plane waves. Without loss of generality, consider a dipole, whose orientation is denoted by a unit vector $\hat{l}$, located at $\vec{r_0} = -(h+m)\hat{z}$. The field of this dipole within a uniform medium with permittivity ε_1 can be expressed by [30]

$$\vec{\mathbf{E}}_d(\vec{r}) = -\frac{Ik_0 Z_0}{8\pi^2} \int_{-\infty}^{\infty} \int_{-\infty}^{\infty} \left\{ \frac{1}{k_{1z}^i} [\bar{\bar{I}} - \frac{\vec{k}_1^i \vec{k}_1^i}{k_1^2}] \cdot \hat{l} e^{j(m+h)k_{1z}^i} \right\} e^{j\vec{k}_1^i \cdot \vec{r}} dk_x^i dk_y^i \tag{2.13}$$

where I is the amplitude of the sinusoidal current carried by the dipole. The integrand of (2.13) can be regarded as $\vec{\mathbf{E}}_0 e^{i\vec{k}_1^i \cdot \vec{r}}$ where

$$\vec{\mathbf{E}}_0 = -\frac{Ik_0 Z_0}{8\pi^2}\frac{1}{k_{1z}^i}\left[\hat{l} - \frac{(\vec{k}_1^i \cdot \hat{l})\vec{k}^i}{k_1^2}\right]$$

is the amplitude of each plane wave propagating along $\hat{k}_1^i = \vec{k}_1^i / k_1$. Using superposition, the mean scattered field in the presence of the upper free-space medium with rough interface, can be computed from the coherent sum of all reflected plane waves. That is

$$\langle \vec{\mathbf{E}}^t \rangle \approx \vec{\mathbf{E}}_{ref} - \frac{Ik_0 Z_0}{8\pi^2}\int_{-\infty}^{\infty}\int_{-\infty}^{\infty}\frac{1}{k_{1z}^i}\left[(\hat{l}\cdot\hat{v}_i(-k_{1z}^i))\hat{v}_i(k_{1z}^i)R_{Bv}^{(1.5)} + (\hat{l}\cdot\hat{h}_i(-k_{1z}^i))\hat{h}_i(k_{1z}^i)R_{Bh}^{(1)}\right] \cdot e^{-jk_{1z}^i(z-m-h)}e^{j(k_x^i x + k_y^i y)}dk_x^i dk_y^i \tag{2.14}$$

where $\vec{\mathbf{E}}_{ref}$ is the field of the dipole in the presence of the upper free-space medium with a planar interface at z = 0. The expression for $\vec{\mathbf{E}}_{ref}$ is similar to the integrand in (2.14) with the exception that R_B is replaced with R_{ref}. Using the change of variables

$$x = \rho\cos\varphi, \qquad y = \rho\sin\varphi$$
$$k_x = k_\rho\cos\gamma, \qquad k_y = k_\rho\sin\gamma$$

and making the use of the following identities

$$\int_0^{2\pi}\cos m\nu e^{jk_\rho\rho\cos(\varphi-\nu)}d\nu = 2\pi i^m\cos m\varphi J_m(k_\rho\rho)$$
$$\int_0^{2\pi}\sin m\nu e^{jk_\rho\rho\cos(\varphi-\nu)}d\nu = 2\pi i^m\sin m\varphi J_m(k_\rho\rho),$$

the integral in (14) can be simplified to

$$\langle \vec{\mathbf{E}}^s \rangle = \frac{Ik_0 Z_0}{4\pi} \int_0^\infty dk_\rho \frac{k_\rho e^{-jk_{1z}(z-m-h)}}{k_{1z}} \left\{ \left[\frac{R_{Bh}^{(1)}}{2} \{ (J_0(k_\rho\rho) + J_2(k_\rho\rho)\cos 2\varphi) l_x \right.\right.$$
$$+ J_2(k_\rho\rho)\sin 2\varphi l_y \} + \frac{R_{Bv}^{(1.5)}}{k_1^2} \{ -\frac{k_{1z}^2}{2}(J_0(k_\rho\rho) - J_2(k_\rho\rho)\cos 2\varphi) l_x$$
$$\left. + \frac{k_{1z}^2}{2} J_2(k_\rho\rho)\sin 2\varphi l_y - jk_\rho k_{1z}\cos\varphi J_1(k_\rho\rho) l_z \} \right] \hat{x} + \left[\frac{R_{Bh}^{(1)}}{2} \{ J_2(k_\rho\rho) \cdot \right.$$
$$\sin 2\varphi l_x + (J_0(k_\rho\rho) - J_2(k_\rho\rho)\cos 2\varphi) l_y \} + \frac{R_{Bv}^{(1.5)}}{k_1^2} \{ \frac{k_{1z}^2}{2} J_2(k_\rho\rho) \cdot$$
$$\left. \sin 2\varphi l_x - \frac{k_{1z}^2}{2}(J_0(k_\rho\rho) + J_2(k_\rho\rho)\cos 2\varphi) l_y - jk_\rho k_{1z}\sin\varphi J_1(k_\rho\rho) l_z \} \right] \hat{y}$$
$$\left. + \frac{R_{Bv}^{(1.5)}}{k_1^2} [jk_\rho k_{1z}(\cos\varphi l_x + \sin\varphi l_y) J_1(k_\rho\rho) + k_\rho^2 J_0(k_\rho\rho) l_z] \hat{z} \right\} \tag{2.15}$$

Obviously a similar expression can be obtained for $\vec{\mathbf{E}}_{ref}$. As will be shown later, the accuracy of the distorted Born approximation degrades as the mean height m and/or the normalized permittivity difference $\frac{\varepsilon_1 - \varepsilon_2}{\varepsilon_2}$ increase. To rectify this problem to some extent, we use the fact that an exact solution is available for a planar dielectric interface. In fact for a flat interface($\sigma = 0$) located at $z = -m$, the reflection coefficient can be computed from

$$R_{exact}(\sigma = 0) = R_{ref} e^{i2k_{1z}^i m} \approx R_{ref} + R_{Born}(\sigma = 0) \tag{2.16}$$

On the other hand the mean reflection coefficient at the interface with rms height σ is given by

$$R_{exact}(\sigma) \approx R_{ref} + R_{Born}(\sigma) \tag{2.17}$$

Now combining (2.16) and (2.17) it can easily be shown that

$$R_{exact}(\sigma) \approx R_{exact}(\sigma = 0) - R_{Born}(\sigma = 0) + R_{Born}(\sigma) \tag{2.18}$$

and substituting (2.18) into (2.15), the modified solution is given by

$$\langle \vec{\mathbf{E}}^t_{exact}(\sigma) \rangle \approx \vec{\mathbf{E}}_{exact}(\sigma = 0) - \vec{\mathbf{E}}^s_{Born}(\sigma = 0) + \langle \vec{\mathbf{E}}^s_{Born}(\sigma) \rangle \tag{2.19}$$

2.3 Asymptotic Evaluation

In the previous section, a closed form solution for the mean-field of a dipole inside a dielectric medium with rough interface was obtained. When the radial distance(ρ) between the observation point and the source point is large, the integrand becomes highly oscillatory and therefore accurate numerical evaluation of the integral becomes extremely inefficient. This is especially true when both points are near the interface. An approximate analytical expansion can be obtained by applying the standard technique of the steepest descent [24, 25]. The standard approach is to change the contour of integration by first extending the limit of the integral over the entire real axis($-\infty$,∞) and then using a change of variable $k_\rho = k_1 \sin w$. The expressions for the reflection coefficients, in the w-plane, take the following forms

$$R_h = \frac{\cos w - \sqrt{\kappa - \sin^2 w}}{\cos w + \sqrt{\kappa - \sin^2 w}}, \quad R_v = \frac{\kappa \cos w - \sqrt{\kappa - \sin^2 w}}{\kappa \cos w + \sqrt{\kappa - \sin^2 w}}$$

where $\kappa = \frac{\varepsilon_2}{\varepsilon_1} < 1$. These introduce a branch cut (with the branch point at $w_b = \sin^{-1}\sqrt{\kappa}$) in the w-plane which may be encountered by the steepest descent path. In this case, diffracted field is dominated by the saddle point and the branch cut contributions. Hence, in general,

each component of the diffracted field may be written as

$$\mathbf{E}_i \sim I_s + \mathrm{U}(\theta_s - \theta_c) I_{BC} \tag{2.20}$$

where I_s and I_{BC} represent the saddle point and the branch cut contribution respectively and U(·) is the Heaviside step function, θ_s is the saddle point, and θ_c is given by

$$\theta_c = \mathrm{Re}\{w_b\} - \cos^{-1}[\mathrm{sech}(\mathrm{Im}\{w_b\})]$$

The saddle point contribution can be obtained rather easily. The saddle points corresponding to the integrand of (2.15) are $w_s = \theta_{1,2}$ where $\sin\theta_{1,2} = \frac{\rho}{r_{1,2}}$, $\cos\theta_1 = \frac{h+h'}{r_1}$, $\cos\theta_2 = \frac{h+h'+2m}{r_2}$, $r_1 = \sqrt{\rho^2 + (h+h')^2}$, and $r_2 = \sqrt{\rho^2 + (h+h'+2m)^2}$. The saddle point(geometric optics) contribution is found to be

$$\begin{aligned} E_i^G \sim -j\frac{Ik_0Z_0}{8\pi}\Big[&\frac{e^{-jk_1r_1}}{r_1}\left\{R_h a_{ih} + R_v\cos^2\theta_1 a_{iv} + b_i \sin 2\theta_1 R_v l_z\right\} + \\ &\frac{e^{-jk_1r_2}}{r_2}\left\{R_{Bh} a_{ih} + R_{Bv}^{(1.5)}\cos^2\theta_2 a_{iv} + b_i \sin 2\theta_2 R_{Bv}^{(1.5)} l_z\right\}\Big] \end{aligned} \tag{2.21}$$

for subscript i = x or y, and

$$\begin{aligned} b_x &= \cos\varphi, \quad b_y = \sin\varphi, \\ a_{xh} &= (1-\cos 2\varphi)l_x - \sin 2\varphi l_y, \quad a_{xv} = -(1+\cos 2\varphi)l_x - \sin 2\varphi l_y, \\ a_{yh} &= -\sin 2\varphi l_x + (1+\cos 2\varphi)l_y, \quad a_{yv} = -\sin 2\varphi l_x - (1-\cos 2\varphi)l_y. \end{aligned}$$

The z component of the field is given by

$$\begin{aligned} E_z^G \sim \frac{Ik_0Z_0}{4\pi}\Big[&R_v \sin\theta_1 \frac{e^{-jk_1r_1}}{r_1}\left\{\cos\varphi l_x + \sin\varphi l_y + \sin\theta_1 l_z\right\} + \\ &R_{Bv}^{(1.5)} \sin\theta_2 \frac{e^{-jk_1r_2}}{r_2}\left\{\cos\varphi l_x + \sin\varphi l_y + \sin\theta_2 l_z\right\}\Big] \end{aligned} \tag{2.22}$$

In (2.21) and (2.22), the Fresnel (R_v,R_h) and Born (B_{Bh},$R_{Bv}^{(1.5)}$) reflection coefficients are evaluated at the saddle point. Evaluation of the branch cut is far more complex. In this case, the integral is expanded near the branch cut and the contour is deformed to the steepest descent at the branch cut using a change of variables [24]

$$\cos(w-\theta)=\cos(w_b-\theta)+js^2$$

After much algebra, the branch cut(lateral wave) contribution of (2.15) is given by

$$\vec{E}^L \sim \frac{jIlZ_1}{2\pi(1-\kappa)^{1/4}}\frac{e^{-jk_0\rho}}{\sqrt{\rho}}\left[\frac{u(\theta_1-\theta_c)e^{-jk_1\sqrt{1-\kappa}(h+h')}}{[(h+h')\sqrt{\kappa}-\rho\sqrt{1-\kappa}]^{3/2}}\bar{\bar{A}}_1+\right.$$
$$\left.\frac{1}{8k_1^2\sqrt{1-\kappa}}\frac{u(\theta_2-\theta_c)e^{-jk_1\sqrt{1-\kappa}(h+h'+2m)}}{[(h+h'+2m)\sqrt{\kappa}-\rho\sqrt{1-\kappa}]^{3/2}}\bar{\bar{A}}_2\right]\cdot\hat{l} \tag{2.23}$$

where $\bar{\bar{A}}_1$ and $\bar{\bar{A}}_2$ are symmetric dyads defined by

$$\bar{\bar{A}}_1=\begin{bmatrix} \frac{\cos^2\varphi-\kappa}{\kappa} & \frac{\cos\varphi\sin\varphi}{\kappa} & \sqrt{\frac{1-\kappa}{\kappa}}\cos\varphi \\ \frac{\cos\varphi\sin\varphi}{\kappa} & \frac{\sin^2\varphi-\kappa}{\kappa} & \sqrt{\frac{1-\kappa}{\kappa}}\sin\varphi \\ \sqrt{\frac{1-\kappa}{\kappa}}\cos\varphi & \sqrt{\frac{1-\kappa}{\kappa}}\sin\varphi & 1 \end{bmatrix}$$

and

$$\bar{\bar{A}}_2=\begin{bmatrix} 2(R'_{Bh}\sin^2\varphi-R_{Bv}^{(1.5)'}\cos^2\varphi\cos^2w_b) & -\sin2\varphi(R'_{Bh}+R_{Bv}^{(1.5)'}\cos^2w_b) & \cos\varphi\sin2w_bR_{Bv}^{(1.5)'} \\ -\sin2\varphi(R'_{Bh}+R_{Bv}^{(1.5)'}\cos^2w_b) & 2(R'_{Bh}\cos^2\varphi-R_{Bv}^{(1.5)'}\sin^2\varphi\cos^2w_b) & \sin\varphi\sin2w_bR_{Bv}^{(1.5)'} \\ \cos\varphi\sin2w_bR_{Bv}^{(1.5)'} & \sin\varphi\sin2w_bR_{Bv}^{(1.5)'} & 2\sin^2w_bR_{Bv}^{(1.5)'} \end{bmatrix}$$

In equation (2.23) $R_v', R_h', R_{Bv}^{(1.5)'}$, and R_{Bh}' are coefficients of the linear term in the Taylor expansion of the each reflection coefficient at the branch point given by

$$R_v' = -\frac{2\alpha}{k\cos w_b}, \quad R_h' = -\frac{2\alpha}{\cos w_b}$$
$$R_{Bv}^{(1.5)'} = A(\kappa-1)(g_{v1}+g_{v2}), \quad R_{Bh}' = Ak_1^2(\kappa-1)(g_{h1}+g_{h2})$$

where

$$\begin{aligned}
g_{v1} &= D\left[\frac{(\kappa-2)C}{\kappa\cos w_b} - j2k_1 m e^{-j2k_1 m\cos w_b} + \frac{CB}{A\alpha}\right], \\
g_{v2} &= E\left[j2k_1 m - \frac{4-\kappa C}{\kappa\cos w_b} - \frac{CB}{A\alpha}\right], \\
g_{h1} &= \frac{BC}{A\alpha} - j2k_1 m e^{-j2k_1 m\cos w_b} - \frac{C}{\cos w_b}, \\
g_{h2} &= j2k_1 m - \frac{4+C}{\cos w_b} - \frac{BC}{A\alpha}
\end{aligned}$$

and

$$\begin{aligned}
A &= \mathrm{Re}\{h(w_b)-1\}, \quad B = \mathrm{Re}\{h(w_b)\frac{\sigma^2\alpha}{2}k_1\cos w_b - j\frac{\sigma\alpha}{\sqrt{2\pi}}\}, \\
C &= 1-e^{-j2k_1 m\cos w_b}, \quad D = k_1^2\cos^2 w_b + \frac{k_1^2}{\kappa}\sin^2 w_b = k_0^2(2\varepsilon_1 - 1), \\
E &= -k_1^2\cos^2 w_b + \frac{k_1^2}{\kappa}\sin^2 w_b = k_0^2, \quad h(w_b) = e^{-\sigma^2 k_1^2\cos^2 w_b/2} erfc(-j\frac{\sigma k_1\cos w_b}{\sqrt{2}}), \\
\alpha &= \sqrt{\frac{j\sin 2w_b}{\sin(w_b-\theta)}}
\end{aligned}$$

Higher order lateral waves (interaction of the lateral wave with the underlying ground plane), $\vec{\mathbf{E}}_{gL}^{L}$ that is the lateral wave generated from the image of the source in the ground plane, and $\vec{\mathbf{E}}_{Lg}^{L}$ that is the reflected lateral wave from the ground plane can be computed

using (2.23) directly. Assuming the canopy height is H,

$$\vec{\mathbf{E}}_{gL}^{L} \sim \frac{jIlZ_1}{2\pi(1-\kappa)^{1/4}} \frac{e^{-jk_0\rho}}{\sqrt{\rho}} \left[\frac{u(\theta_1-\theta_c)e^{-jk_1\sqrt{1-\kappa}(2H-h+h')}}{[(2H-h+h')\sqrt{\kappa}-\rho\sqrt{1-\kappa}]^{3/2}} \bar{\bar{\mathbf{A}}}_1 + \frac{1}{8k_1^2\sqrt{1-\kappa}} \frac{u(\theta_2-\theta_c)e^{-jk_1\sqrt{1-\kappa}(2H-h+h'+2m)}}{[(2H-h+h'+2m)\sqrt{\kappa}-\rho\sqrt{1-\kappa}]^{3/2}} \bar{\bar{\mathbf{A}}}_2 \right] \cdot \bar{\bar{\mathbf{R}}} \cdot \hat{l} \tag{2.24}$$

and

$$\vec{\mathbf{E}}_{Lg}^{L} \sim \frac{jIlZ_1}{2\pi(1-\kappa)^{1/4}} \frac{e^{-jk_0\rho}}{\sqrt{\rho}} \left[\frac{u(\theta_1-\theta_c)e^{-jk_1\sqrt{1-\kappa}(2H+h-h')}}{[(2H+h-h')\sqrt{\kappa}-\rho\sqrt{1-\kappa}]^{3/2}} \bar{\bar{\mathbf{R}}} \cdot \bar{\bar{\mathbf{A}}}_1 + \frac{1}{8k_1^2\sqrt{1-\kappa}} \frac{u(\theta_2-\theta_c)e^{-jk_1\sqrt{1-\kappa}(2H+h-h'+2m)}}{[(2H+h-h'+2m)\sqrt{\kappa}-\rho\sqrt{1-\kappa}]^{3/2}} \bar{\bar{\mathbf{R}}} \cdot \bar{\bar{\mathbf{A}}}_2 \right] \cdot \hat{l} \tag{2.25}$$

where $\bar{\bar{\mathbf{R}}}$ is the ground reflectivity matrix given by

$$\bar{\bar{\mathbf{R}}} = \begin{bmatrix} \sin^2\varphi R_\perp - \cos^2\varphi R_{||} & -\sin\varphi\cos\varphi(R_\perp + R_{||}) & 0 \\ -\sin\varphi\cos\varphi(R_\perp + R_{||}) & \cos^2\varphi R_\perp - \sin^2\varphi R_{||} & 0 \\ 0 & 0 & R_{||} \end{bmatrix}$$

Generally the two higher order lateral waves, $\vec{\mathbf{E}}_{gL}^{L}$, and $\vec{\mathbf{E}}_{Lg}^{L}$, can be ignored except for the case where the receiver is near the ground plane. This is due to the additional exponential decay ($e^{-jk_1\sqrt{1-\kappa}\cdot 2H}$) in (2.24), and (2.25).

It can easily be shown that this formulation reduces to the flat boundary case by letting σ go to zero. In this case, $h(w_b) = 1$ which reduces A and consequently $R_{Bv}^{(1.5)'}$ and R'_{Bh} to zero. The remaining terms in (2.23), (2.24) and (2.25) would be the branch cut contribution from a flat boundary. The above formulation is valid when the observation point(θ) is away from the complex critical angle. To extend the valid region to observation point near the

critical point, (2.20) may be modified as

$$\mathbf{E}_i \sim I_s + u(\theta - \theta_c) I_{BC} \cdot F(\beta) \tag{2.26}$$

where $F(\beta)$ is a correction factor. This function can be obtained by retaining higher order terms of the Taylor series expansion of the integrand near the branch cut. For a dielectric with flat interface, $F(\beta)$ is represented by the Weber or parabolic cylinder function as [24, 25]

$$F(\beta) = e^{j(\beta^2/2+3\pi/8)}(2\beta^2)^{3/4} D_{-3/2}(\beta + j\beta)$$

where $\beta = 2\sqrt{k_1 r_1}\sin\frac{\theta_1-\theta_c}{2}$. Here $D_{-3/2}(\beta + j\beta)$ is Weber function of order -3/2 and is defined as [24, 25],

$$D_n(x) = \frac{2e^{x^2/4}}{\Gamma(-n)} \int_0^\infty t^{-2n-1} e^{-(x+t^2)^2/2} dt$$

As β increases, $F(\beta)$ approaches unity and (2.26) reduces to (2.20). It is, however, extremely difficult to modify the formulation for a rough boundary in such simple manner as the higher order derivatives of the special functions in the integrand are difficult to evaluate. The asymptotic expressions clearly indicate that the diffracted field due to the branch cut contribution (see(2.23), (2.24) and (2.25)) decays as $1/\rho^2$ whereas the saddle point contribution decays exponentially ($e^{jk_1 r}/r$). Hence for far observation points the lateral wave is the dominant source of the diffracted field. As will be shown later, the lateral wave for rough boundaries are weaker (depending on $k_0\sigma$) than the lateral wave for a flat boundary.

2.4 Numerical Simulation

In this section, numerical examples are considered to examine the validity of the solution based on distorted Born approximation and to demonstrate the sensitivity of the field intensity at the observation point to the canopy parameters such as effective dielectric constant, canopy-air interface roughness, and transmitter and receiver positions. In the following simulations, the transmitter dipole is assumed to be operating at f=30MHz having $Il = 1$. To examine the effect of transmitter polarization, a vertical dipole ($\hat{l} = \hat{z}$) and a horizontal dipole ($\hat{l} = \hat{y}$) are considered in a canopy with ε_l = 1.03+j0.006, and flat interface at h=3m (0.3λ). Figure 2.2(a) and 2.2(b) show the three components of the diffracted electric field (excluding the direct field contribution from the dipole) as a function of distance for a observation point 3m below the interface (h' = 3m) for the vertical and horizontal dipole respectively. Also shown in these figures are the results obtained from the asymptotic evaluation(see (2.21-2.25) for $k_0\sigma = 0$). From these figures, it is obvious that the field of a vertical dipole experiences less propagation loss than the field of a horizontal dipole.

Figure 2.3 shows the vertical component of the total field (diffracted plus the direct field) for a vertical dipole as a function of distance when h = 2m (0.2λ) and h' = 1m (0.1λ) for three different values of ε_l. In this simulation, the imaginary part of ε_l is kept constant and the real part is changed from 1.01 to 1.05. Figure 2.4 shows a simulation similar to that of Fig.2.3 with the exception that the real part of the effective permittivity is kept constant and the imaginary part is increased. For total field calculations shown in Figures. 2.3 and 2.4 a numerical integration is used for the observation points as far as 2km and for the points beyond 2km the asymptotic method is used. As expected, the propagation loss increases with increasing the imaginary part of ε_l. Next we examine the effect of the location of the transmitter and receiver in the canopy. It should be noted that the dependence of the field on h and h' is of the form, $h + h'$. Figure 2.5 shows the dependence of the field of a vertical dipole as a function of $k_0(h + h')$ for three different permittivity values at fixed lateral distance (ρ = 2.8km). Unless the observation and source points are very close to the

surface, the field decays exponentially as a function of $k_0(h+h')$ with an exponential factor proportional to $\mathrm{Im}[\sqrt{1-\kappa}]$.

To examine the accuracy of the distorted Born solution, a vegetation layer with smooth boundary is considered ($\sigma = 0$, and a non-zero m). For this case an exact solution exists. First the Fresnel reflection coefficients are considered. Figure 2.6(a) and 2.6(b) compare the magnitude and phase of the Fresnel reflection coefficient(R_h) of a dielectric interface with $\varepsilon_l = 1.03 + j0.005$ at $m = 0.6\lambda$ with those computed by the approximate distorted Born solution for perpendicular polarization. The computations are performed at 30MHz for two different values of ε_l and two different layer thickness values as a function of $\sin\theta_i = k_\rho/k_0$. Similar results for parallel polarization are shown in Fig. 2.7(a) and 2.7(b). Their errors in magnitude and phase do not exceed 5% and 10° respectively. The accuracy of the distorted Born approximation degrades as the dielectric constant and layer thickness(m) increases. To determine the region of validity of this solution, the exact solution was compared with the distorted Born approximate solution for a wide range of ε_l and m. It was found that the accuracy of the approximate solution improves as the imaginary part of the dielectric constant increases. To specify the region of validity to the problem at hand and lower the number of independent variables, we considered a canopy with vegetation particle permittivity, $\varepsilon_v = 50 + j25$, and used Polder Van Santen dielectric mixing formula [20] to compute the effective dielectric constant ε_l from

$$\frac{\varepsilon_v - 1}{\varepsilon_v + 2\varepsilon_l}\tilde{f} = \frac{\varepsilon_l - 1}{3\varepsilon_l}$$

where $\tilde{f}$ is the volume fraction. Tolerating 5% error in magnitude and 10° error in phase of the reflection coefficient, the region under curve shown in Fig.2.8 denotes values of m and ε_l where the distorted Born approximation produces valid results for the reflection coefficients. With a confidence in the formulation of the distorted Born approximation, the effect of surface roughness on the reflection coefficient is considered next. Figure

2.9(a)(perpendicular polarization) and 2.9(b)(parallel polarization) show the magnitude of reflection coefficients as a function of $k_\rho/k_0 = \sin\theta_i$ and two different values of surface rms height $\sigma = \pi/10$ and $\sigma = \pi/5$. In these simulations, $\varepsilon_l = 1.03 + j0.015$ and m was chosen to be 2σ. It is shown that the reflection coefficient is drastically reduced by the surface roughness for low incidence angle and for large value of k_ρ/k_0. The reduction in reflection coefficient is less prominent near the critical angle. This property is very important so far as the field of a dipole is concerned since a significant portion of the contribution of the integrand to the integral comes from this point. Figure 2.10 shows the magnitude of the reflection coefficient for both polarizations versus normalized surface rms height for a canopy with $\varepsilon_l = 1.03 + j0.015$ at 30MHz. Figure 2.11 compares the field of a vertical dipole ($h = 0.2\lambda$, $h' = 0.1\lambda$) obtained using exact solution and the approximate distorted Born solution in a canopy with $\varepsilon_l = 1.01 + j0.006$ and two different values, $m = \lambda/4$ and $m = \lambda/2$ at 30MHz where an excellent agreement is shown. A similar comparison is shown in Fig.2.12 where the effect of imaginary part of the dielectric constant is examined. The effect of surface roughness is shown in Figures 2.13 and 2.14. Vertical and horizontal($\hat{l} = \hat{y}$) dipole in a canopy with $\varepsilon_l = 1.01 + j0.006$ and $\varepsilon_l = 1.03 + j0.015$ and three different values of surface rms height, $\sigma = 0$, $\sigma = \lambda/2$, and $\sigma = \lambda$ are considered (observation point at $\phi = 45°$). It is shown that the surface roughness reduces the field intensity. It is very interesting to note that despite relatively significant surface rms height, lateral wave is still the dominant source of the field in a forested area. This can be attributed to the fact that most contribution of the mean field comes from the integrand of equation(2.15) for values of k_ρ/k_0 near the critical angle. As shown before the value of the reflection coefficient near the critical angle does not experience a significant reduction due to the surface rms height.

2.5 Conclusion

The effect of canopy-air interface roughness on the propagation of electomagnetic waves in forested environment was investigated in this chapter. An analytic formulations that take effect of the rough boundary into account, are obtained for both cases of plane wave and an arbitrary oriented dipole excitation. The solution is obtained using distorted Born approximation to a volumetric integral equation for the induced polarization current in a hypothetical layer above the canopy. This formulation was validated by comparing the approximate results with the exact results in the special case of smooth interface. It is shown that the canopy-air interface roughness reduces the mean field surface reflectivity drastically for plane wave illumination at incidence angles below the critical angle. A significant result of plane wave simulations was the discovery of the fact that the mean surface reflectivity near the critical angle is not drastically affected by the surface roughness, thereby allowing the propagation of the lateral wave despite significant interface roughness. Direct simulations of the field of an arbitrary dipole in a forest with different effective permittivity and surface roughness show that the field at the observation point may be anywhere between 0 to 10dB lower than that for a smooth air-canopy interface dependent on the value of the rms height surface roughness($k_0\sigma$).

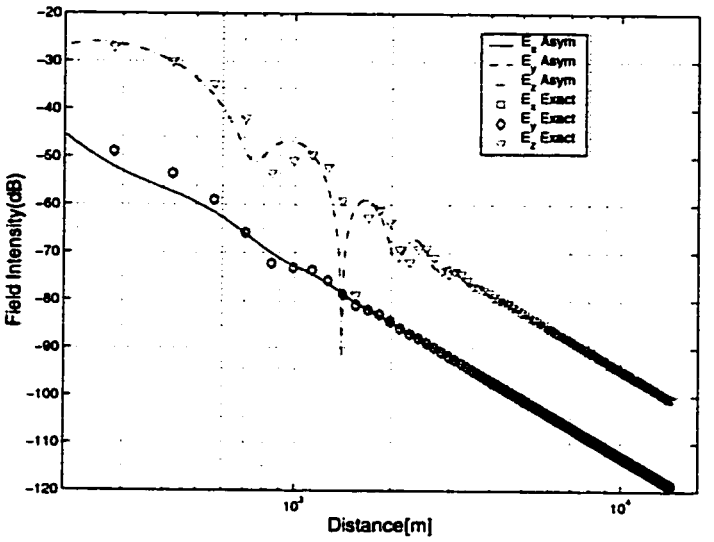

(a) $\hat{l} = \hat{z}$

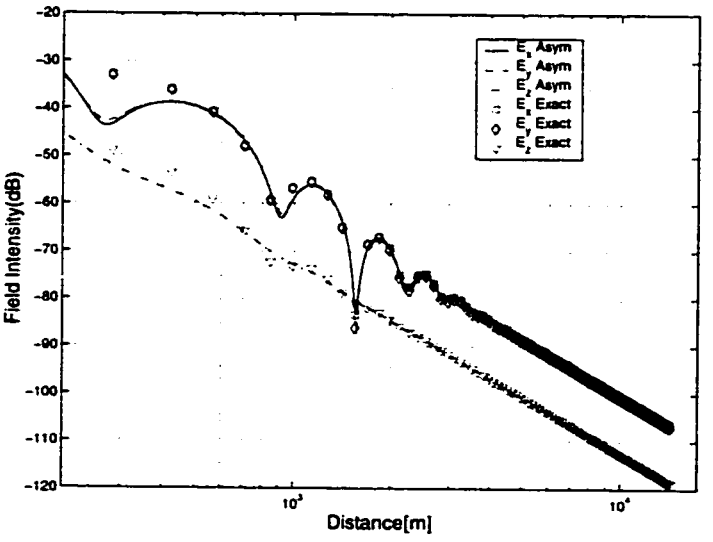

(b) $\hat{l} = \hat{y}$

Figure 2.2: The diffracted field intensity components (see (2.15))for a vertical(a) and horizontal(b) dipole in a canopy with ε_l = 1.03 + j0.006 with a smooth boundary ($\sigma = 0$) , h = 3m, h' = 3m at 30 MHz. The results are obtained with the approximation solution obtained from the asymptotic integral evaluation.

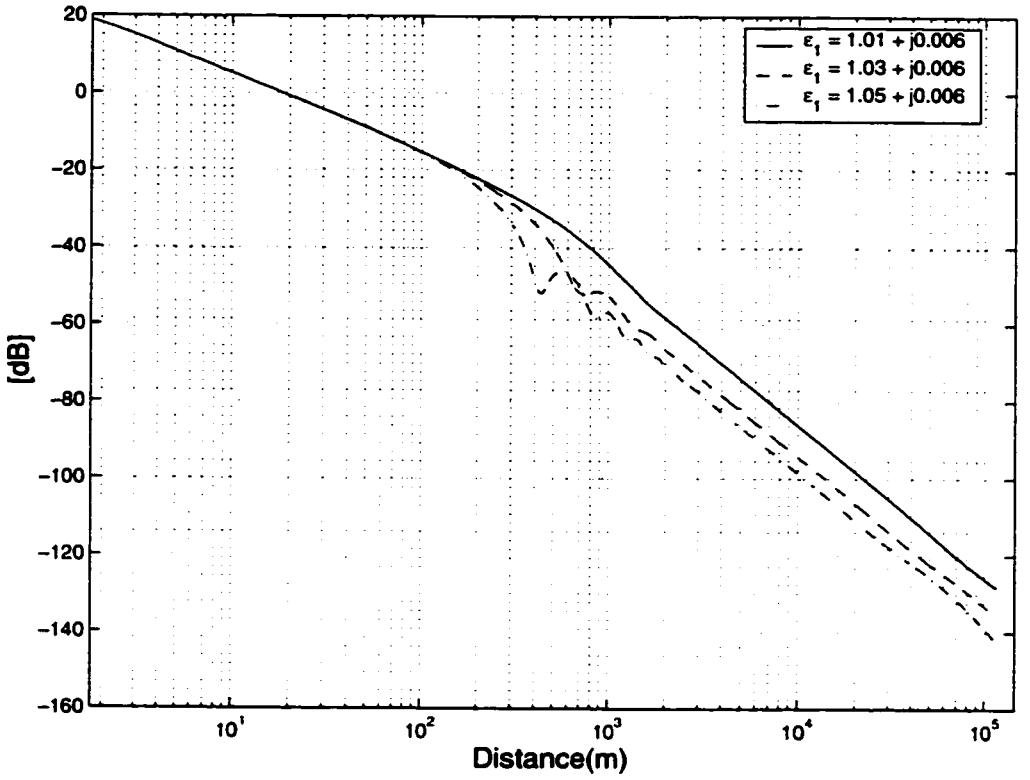

Figure 2.3: Electric field of a vertical dipole as a function of distance in a canopy with effective permittivity ε_1. Three different values for ε_1 are used, 1.01 + j0.006, 1.03 + j0.006, 1.05 + j0.006, and the location of the dipole and observation points are respectively, h = 2m (0.2λ), h' = 1m (0.1λ).

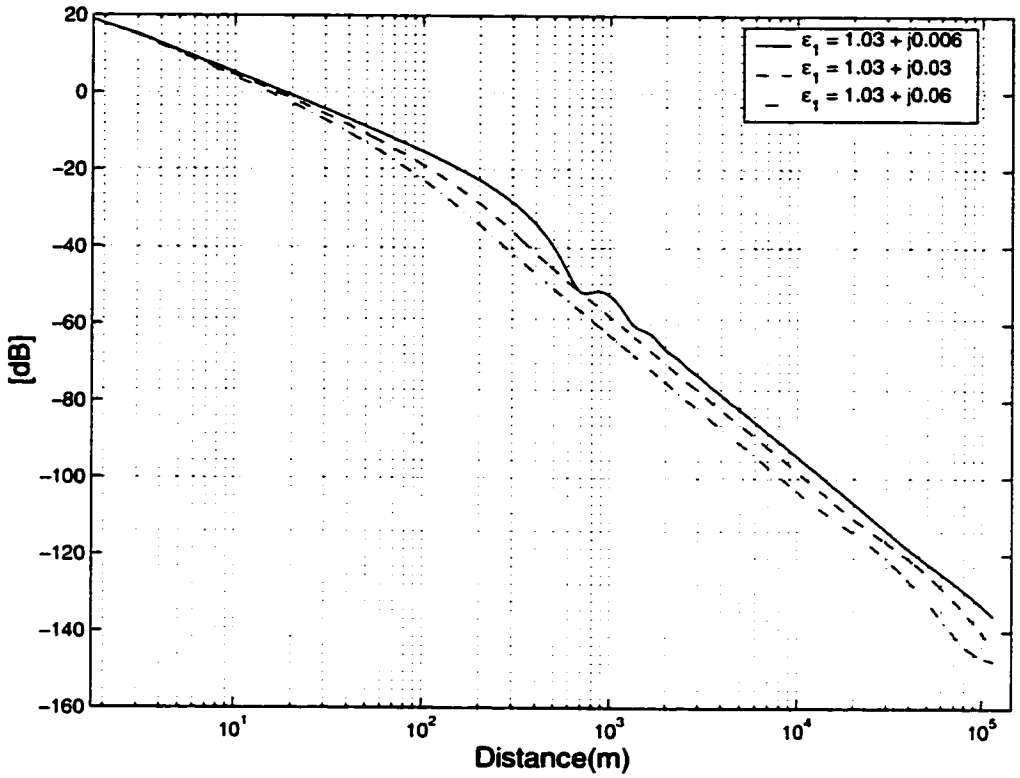

Figure 2.4: Electric field of a vertical dipole as a function of distance in a canopy with effective permittivity ε_1. Three different values for ε_1 are used, 1.03 + j0.006, 1.03 + j0.03, 1.03 + j0.06, and the location of the dipole and observation points are respectively, $h = 2\text{m}$ (0.2λ), $h' = 1\text{m}$ (0.1λ).

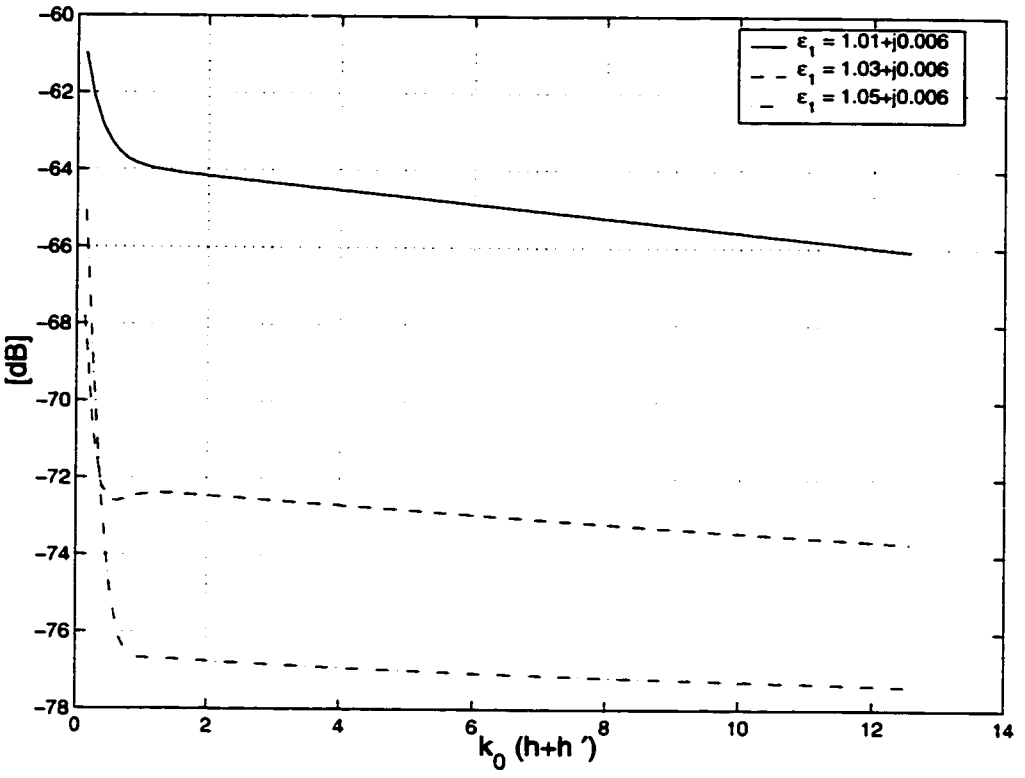

Figure 2.5: Electric field of a vertical dipole(f=30MHz) in a canopy with effective dielectric constant ε_1 as function of $k_0(h+h')$ at a fixed observation point($\rho = 2.8$km).

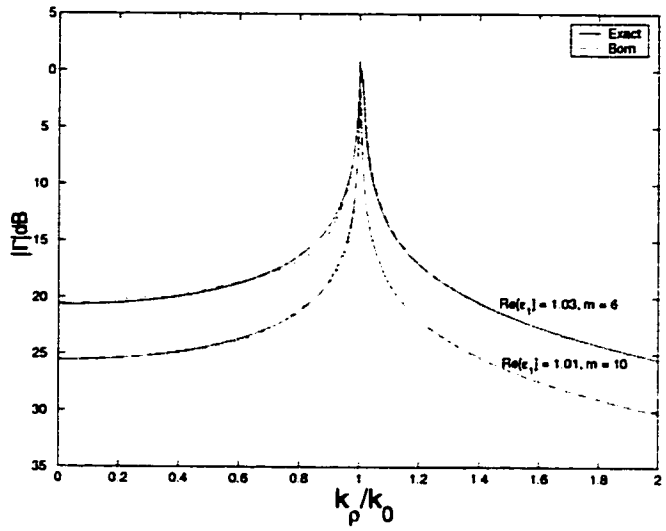

(a)

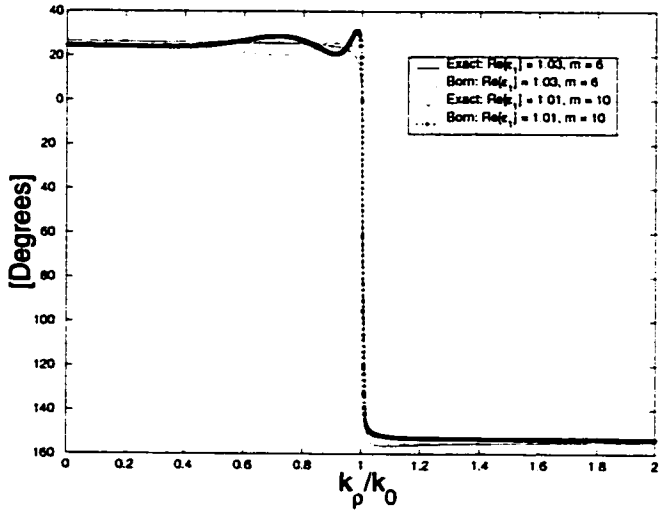

(b)

Figure 2.6: Comparison of the magnitude(a) and phase(b) of reflection coefficient(R_h) with the approximate distorted Born solution(see (9)) for perpendicular polarization. Two permittivity values and two mean layer thickness values are shown as a function of $\sin\theta_i = k_\rho / k_0$, ε_1 = 1.03+j0.005, and m = 6m (0.6λ) and the other is for ε_1 = 1.01+j0.005, and m = 10m (λ). Frequency is 30MHz.

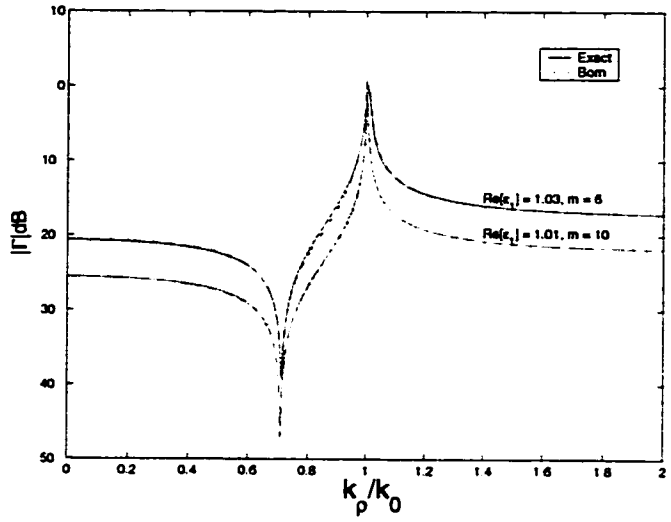

(a)

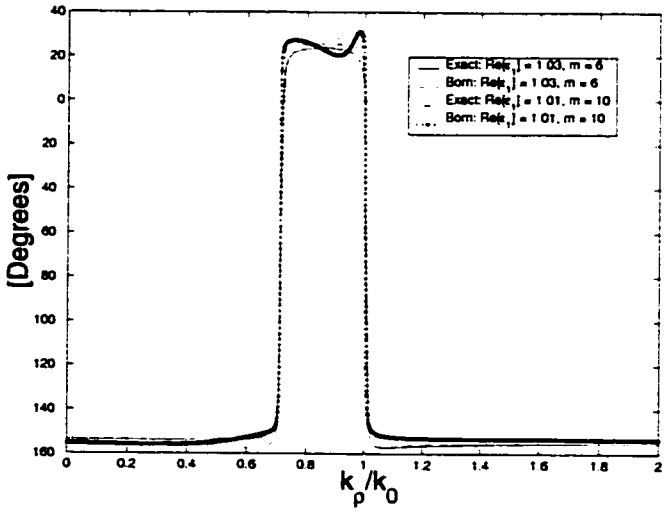

(b)

Figure 2.7: Comparison of the magnitude(a) and phase(b) of reflection coefficient(R_v) with the approximate distorted Born solution(see (12)) for parallel polarization. Two permittivity values and two mean layer thickness values are shown as a function of $\sin\theta_i = k_\rho / k_0$, ε_1 = 1.03+j0.005, and m = 6m (0.6λ) and the other is for ε_1 = 1.01+j0.005, and m = 10m (λ). Frequency is 30MHz.

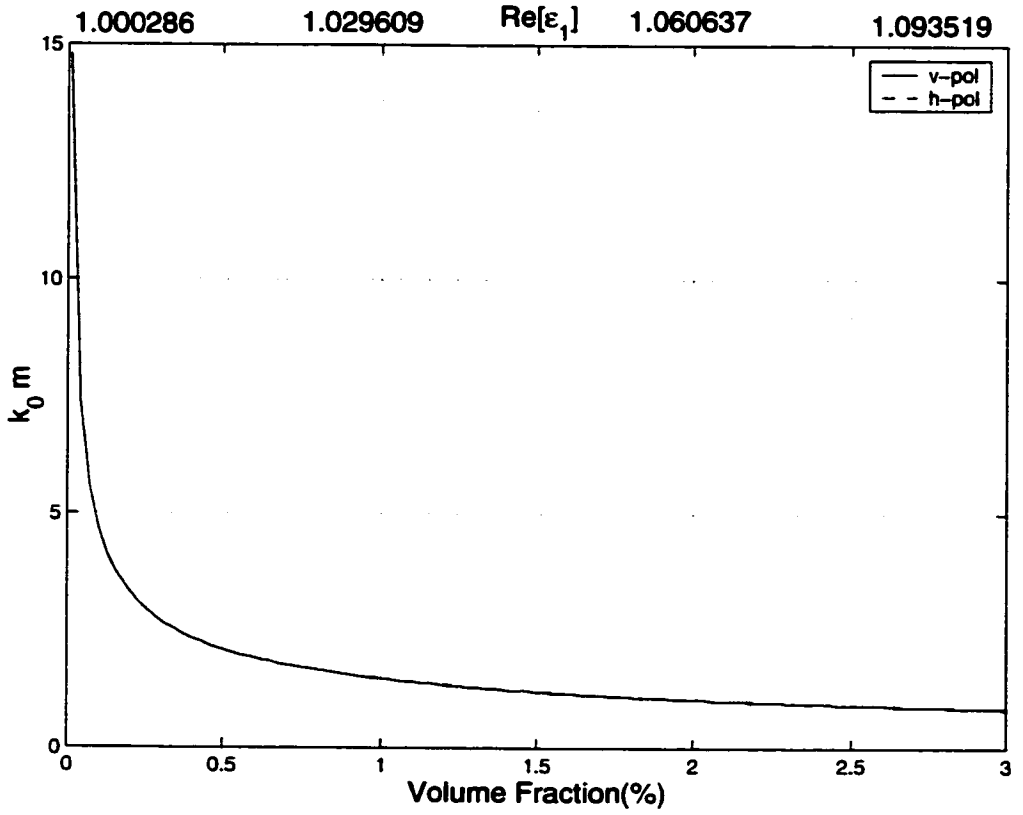

Figure 2.8: The region of validity of the distorted Born approximation (points under the curve) is shown with regard to the reflection coefficient for 5% error criterion.

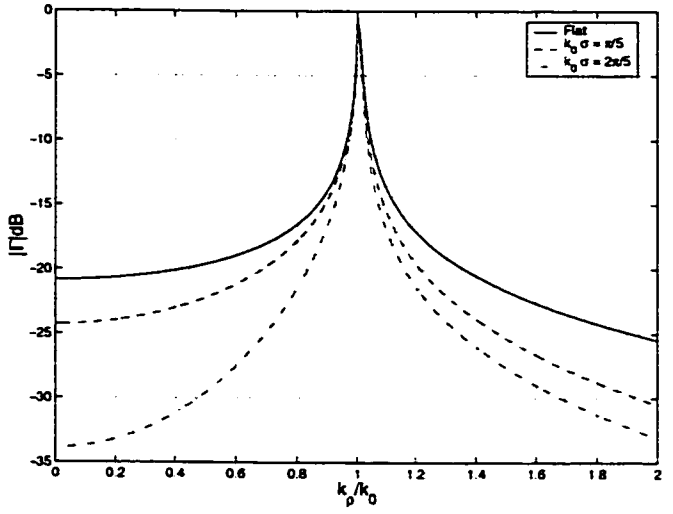

(a)

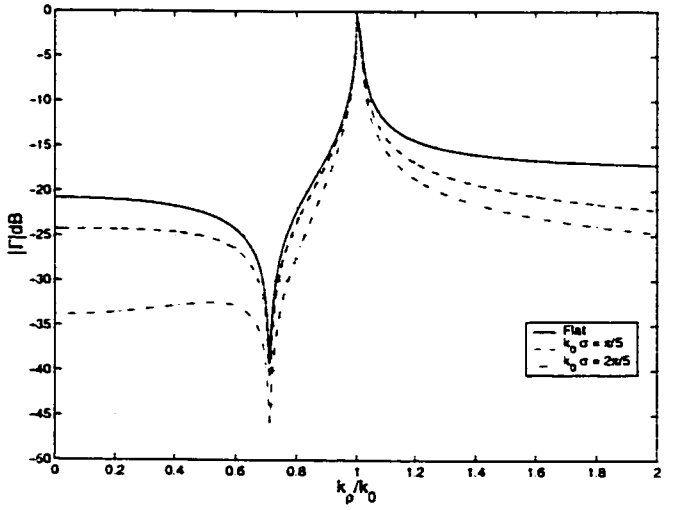

(b)

Figure 2.9: The magnitude of reflection coefficient for perpendicular(a) and parallel(b) polarizations as a function of $k_\rho/k_0 = \sin\theta_i$ for a canopy with ε_1 = 1.03+j0.015 assuming flat surface ($\sigma = 0$), $\sigma = \lambda/10$ ($m = \lambda/5$), and $\sigma = \lambda/5$ ($m = 2\lambda/5$). It is shown that surface roughness significantly decrease the magnitude of the reflection coefficient everywhere except for incidence angles near the critical angle.

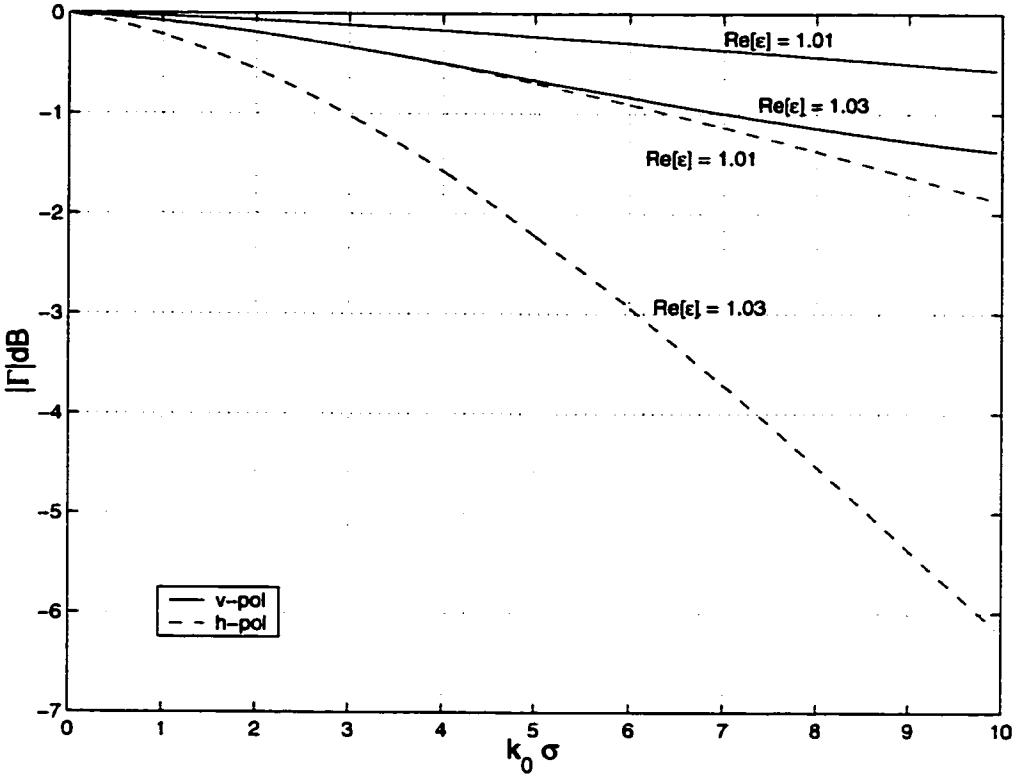

Figure 2.10: Magnitude of reflection coefficient versus normalized rms height($k_0\sigma$) at the critical angle for a canopy with $\varepsilon_1 = 1.03 + j0.015$, and $\varepsilon_1 = 1.01 + j0.005$ for perpendicular and parallel polarization.

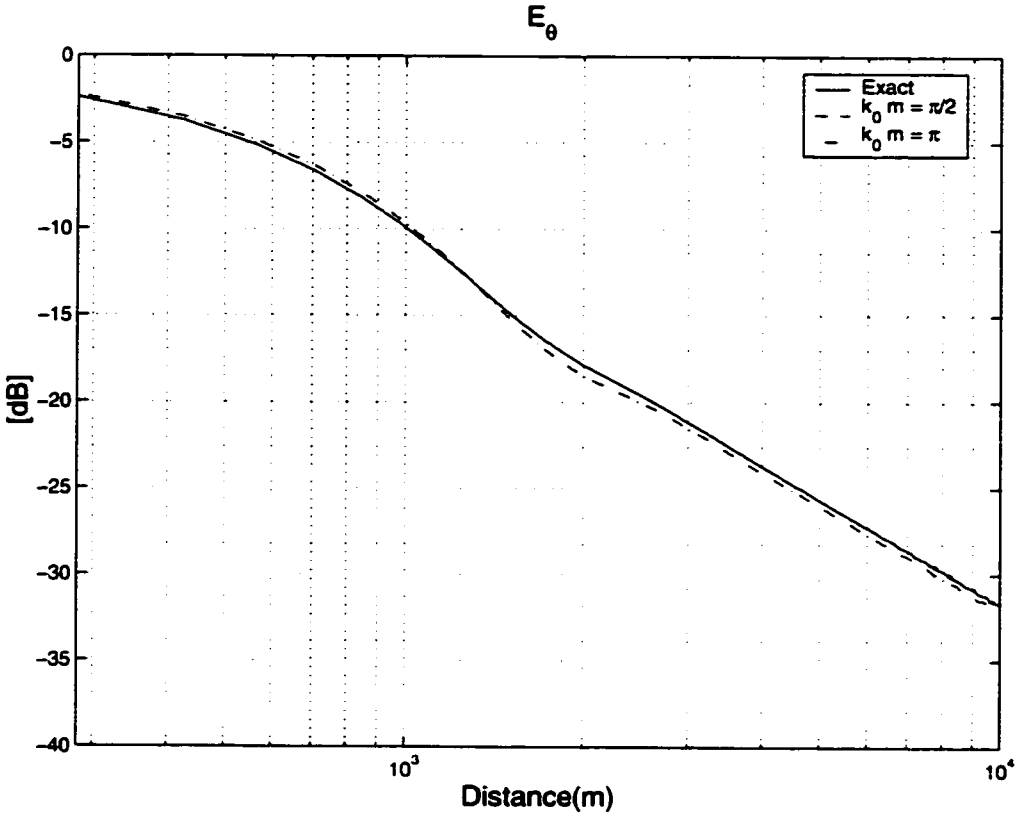

Figure 2.11: Path-loss of a vertical dipole in a canopy with ε_1 = 1.01+j0.006 and smooth interface obtained from the exact solution is compared with distorted Born approximation for two values of m. An operation frequency 30MHz, $h = 0.2\lambda$, and $h' = 0.1\lambda$ are assumed.

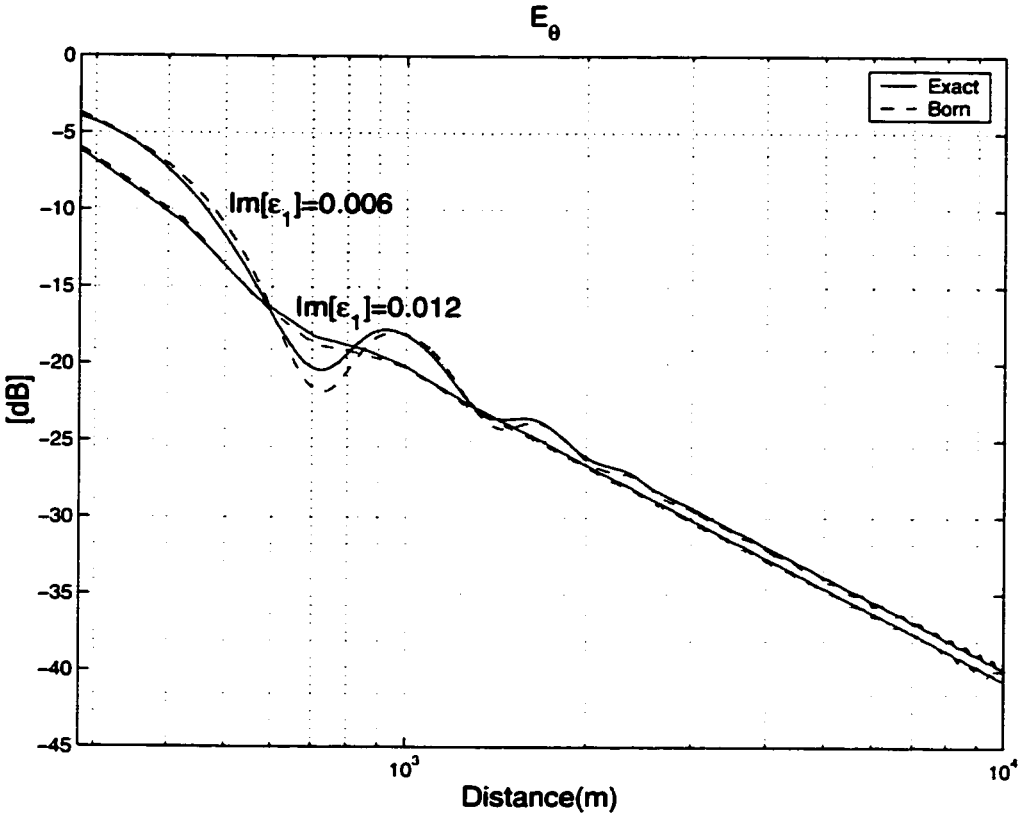

Figure 2.12: Path-loss of a vertical dipole in a canopy with ε_1 = 1.03+j0.006 or 1.03+j0.012 and smooth interface obtained from the exact solution is compared with distorted Born approximation for fixed value of $k_0 m = \pi/5$. An operation frequency 30MHz, $h = 0.2\lambda$, and $h' = 0.1\lambda$ are assumed.

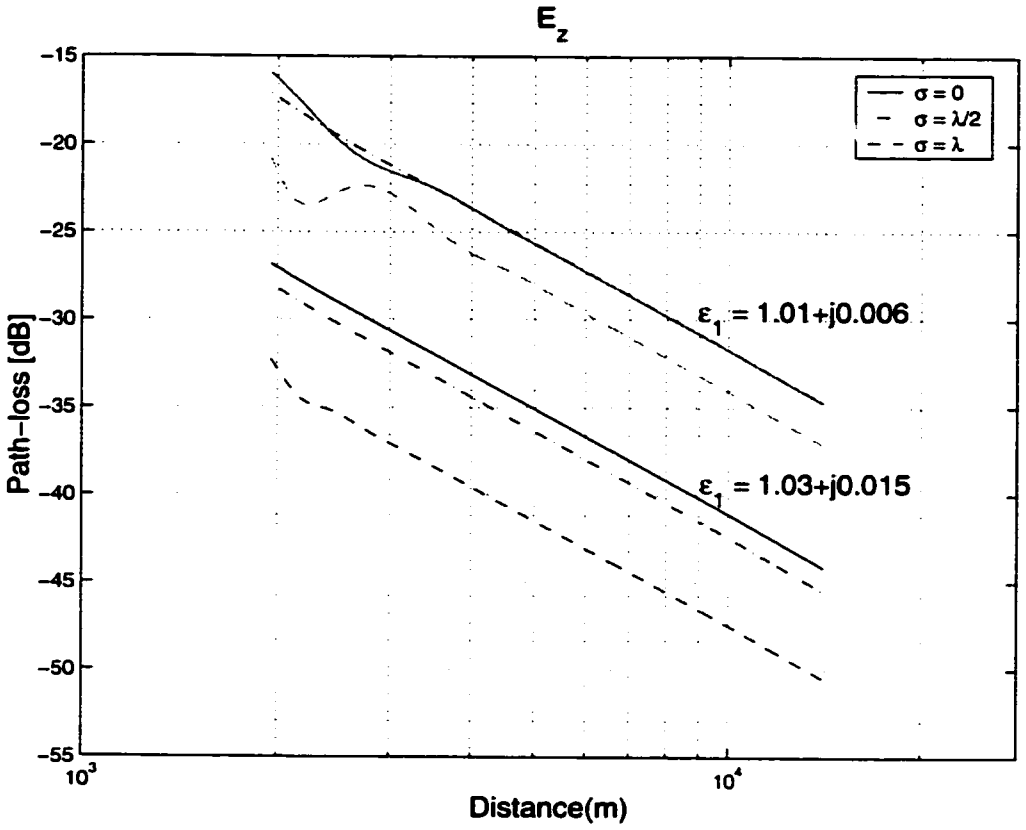

Figure 2.13: Path-loss of a vertical dipole in a forest canopy ($h = 0.2\lambda$, $h' = 0.1\lambda$) for two different values of ε_1 = 1.01 + j0.006 and ε_1 = 1.03 + j0.015 and for three different values of surface rms height, $\sigma = 0$, $\sigma = \lambda/2$, and $\sigma = \lambda$.

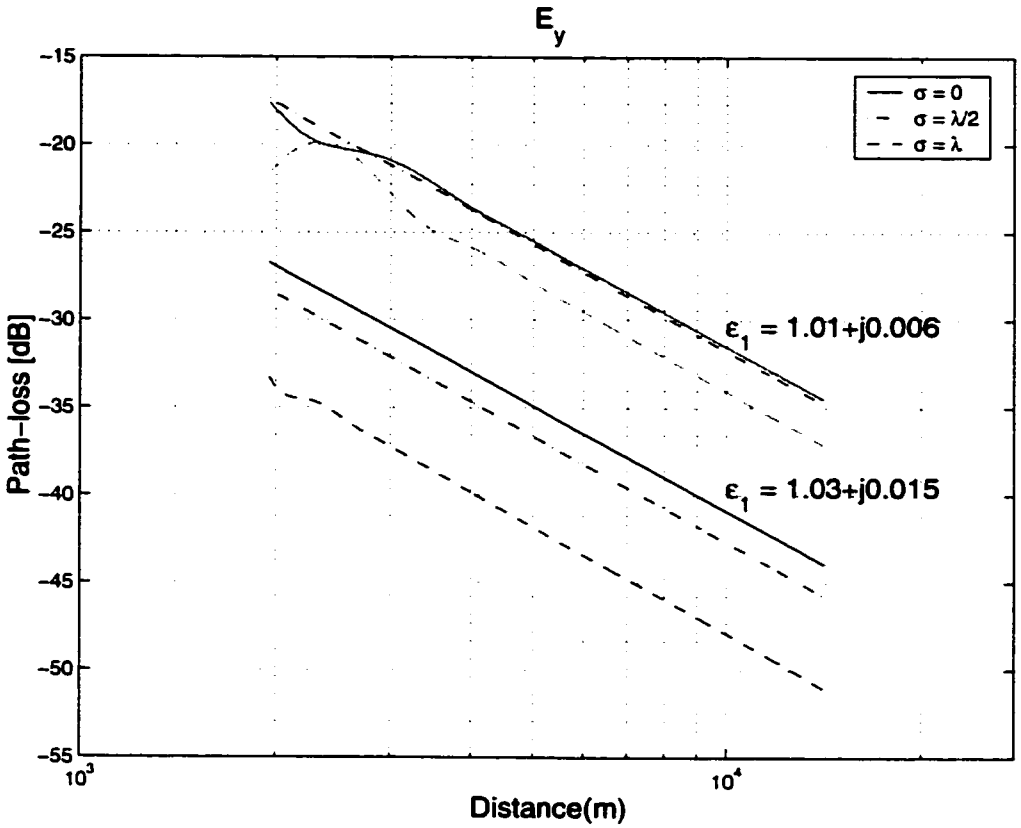

Figure 2.14: Path-loss of a horizontal dipole($\hat{l} = \hat{y}$) in a forest canopy ($h = 0.2\lambda$, $h' = 0.1\lambda$) for two different values of ε_1 = 1.01 + j0.006 and ε_1 = 1.03 + j0.015 and for three different values of surface rms height, $\sigma = 0$, $\sigma = \lambda/2$, and $\sigma = \lambda$.

CHAPTER 3

A Novel Physics-Based Channel Model for Ground-to-Ground communication in a Rural Environment

3.1 Introduction

Due to relatively high attenuation rates, direct wave propagation in a forest environment is not possible over large distances at high frequencies. In the HF-UHF range where both the transmitter and receiver are embedded in the foliage, radio signals can propagate over relatively large distances. This peculiar behavior is explained by certain type of surface waves known as the lateral wave [9]. Mathematically speaking, the lateral wave is the contribution of the branch cut from the integral of the spectral representation of a dipole field inside a half-space dielectric as explained in chapter 2. As mentioned earlier path-loss only partially characterizes the channel and other scattering mechanisms must be accounted for to complete the model. At UHF and lower frequencies, the dimensions of leaves and branches are small compared to wavelength and do not cause significant scattering which is the source of signal fluctuations, multi-path, and dispersion. The effect of tree trunks which are electrically large create a highly scattering environment.

In this chapter the effect of tree trunks is accounted for by computing their interac-

tion with the source and the lateral waves. A numerical solution based on the method of moments (MoM) in conjunction with Monte-Carlo simulation is proposed to evaluate the scattering effects of tree trunks. However, considering the number of tree trunks between the transmitter and receiver, it is quite obvious that a brute-force application of MoM is not possible due to the exorbitant memory and computation time requirements. To make the solution tractable while maintaining the model fidelity, three techniques are proposed: 1) simplification of the MoM formulation noting that tree trunks are sparsely distributed, 2) simplification base on physical insight by noting that the scattered fields from tree trunks between the transmitter and receiver, but distant from them, are almost in-phase, and 3) simplification of field computation using the reciprocity theorem. In what follows, the forest model is described first and then the simplified MoM formulation is presented. This model is used to demonstrate that only scatterers near the source and observation points significantly contribute to the field fluctuations. Next the near-field interaction of tree trunks with the source field and lateral waves are computed by application of reciprocity and using the MoM formulation. Finally, numerical simulations are presented, where the spatial decorrelations in a forest environment are examined and the performance of the antenna arrays and spatial diversity schemes evaluated.

3.2 Forest Model

The model presented in this section is suitable for predicting the statistics of the field radiated by an elementary antenna embedded in a forest environment and is valid for frequencies up to UHF. As mentioned earlier, since the dimensions of leaves and branches are small compared to the wavelength, the forest canopy can be modeled by a homogeneous dielectric . However, the trunks whose dimensions are comparable to or larger than a wavelength must be treated separately. Figure 3.1 shows the geometry of the wave propagation problem where both the source and observation points are within a dielectric slab with ef-

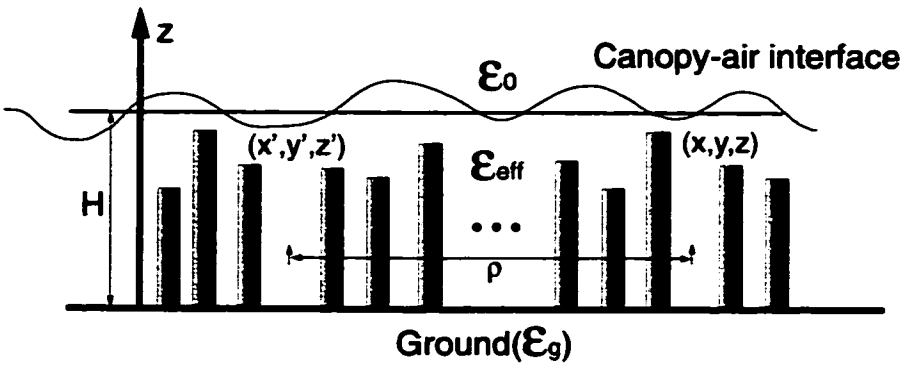

Figure 3.1: Geometry of a forest model for characterization of wave propagation in a forest environment.

fective permittivity ε_{eff}. This dielectric slab is assumed to have a smooth lower interface with a dielectric half-space (representing the ground) and a rough upper interface with air. Tree trunks are modeled by dielectric cylinders perpendicular to the ground plane having a relatively large height-to-diameter ratio. Ignoring the scattering from tree trunks, the mean field at the receiver is composed of the following components as depicted, in Fig. 3.2 :

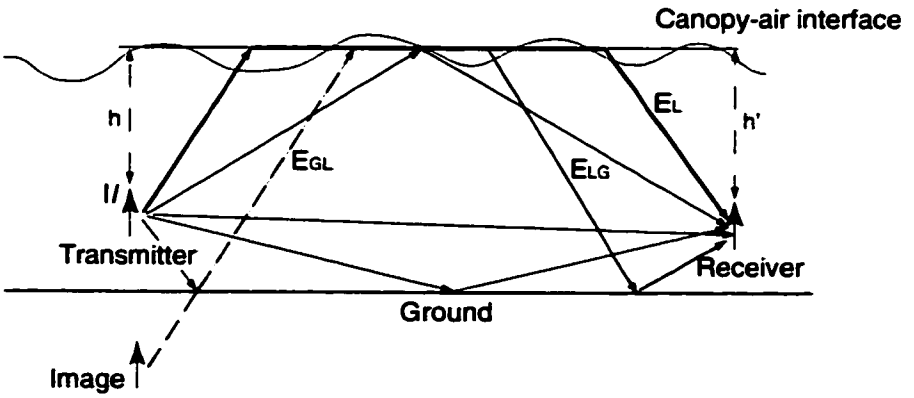

Figure 3.2: Wave propagation mechanisms contributing to the mean field without tree trunks in a forest environment.

1. geometric optics terms which include the direct propagation between the transmitter and receiver and reflected fields from the upper and lower interfaces. The mean reflected field from the upper interface is reduced exponentially where the exponent is proportional to the rms height of the canopy-air interface roughness [19]. These

terms are only important when the receiver is relatively close to the transmitter, otherwise due to the lossy nature of the effective dielectric constant of the foliage these components do not contribute much. Basically the geometric optics terms exponentially decay with distance between the transmitter and the receiver.

2. Lateral wave (a diffraction term) which propagates along the canopy-air interface and decays proportionally to the reciprocal of the radial distance squared($\sim 1/\rho^2$). The path loss associated with the lateral wave propagation increases with increasing foliage density (effective dielectric constant) and decreases by bringing the source or observation points closer to the canopy-air interface. The path loss increases as the canopy-air interface roughness (rms height) relative to wavelength increases. Close examination of the expression representing the lateral wave contribution reveals that the contribution can be attributed to a ray that emanates from the source along the critical angle, propagates along the canopy-air interface, and arrives at the receiver along the critical angle as shown in Fig. 3.2. Other higher order lateral wave contributions also exist, of which two are significant. One corresponds to the ray emitted from the source which reflects from the ground boundary, propagates along the critical angle and then travels along the interface (E_{GL}). The other one is the reflected lateral wave from the ground which arrives at the receiver (E_{LG}). These two contributions are also shown in Fig. 3.2

The expression for the electric field resulted from the asymptotic expansion of the spectral integral around the branch cut (Lateral wave) for a half-space dielectric with a smooth boundary is given by (2.23), and rewritten:

$$\vec{\mathbf{E}}^L \sim \frac{jIlZ_0}{2\pi(1-\kappa)^{1/4}} \frac{e^{-jk_0\rho}e^{-jk_1\sqrt{1-\kappa}(h+h')}}{\left[(h+h')\sqrt{\kappa}-\rho\sqrt{1-\kappa}\right]^{3/2}\rho^{1/2}}\bar{\bar{\mathbf{A}}}_1\cdot\hat{l} \tag{3.1}$$

where $k_1 = k_0\sqrt{\varepsilon_{eff}}$, ρ is the radial distance between the transmitter and receiver, h and h' are the depth of transmitter and receiver below the canopy-air interface, Il is the cur-

rent moment of the dipole, and k_0 and Z_0 are, respectively, the propagation constant and the characteristic impedance of free-space. In (3.1) the unit vector, $\hat{l}$, denotes the dipole orientation $\kappa = 1/\varepsilon_{eff}$ where ε_{eff} is the effective dielectric constant of foliage, and $\bar{\bar{A}}_1$ is a symmetric dyad given by equation (2.3). Here ϕ is a cylindrical coordinate angle representing the location of observation point with respect to the transmitter. The phase term of equation (3.1) indicates that the lateral wave is locally a plane wave propagating along the direction $\vec{k}_1 = k_0 \left[\cos\phi\hat{x} + \sin\phi\hat{y} - \sqrt{\frac{1-\kappa}{\kappa}}\hat{z}\right]$ and also noting $\vec{E}_L \cdot \vec{k}_1 = 0$. The expression for the lateral wave contribution for rough canopy-air interface (2.23) is more complicated than (3.1), but the mean-field still represents a plane wave locally. To include the effects of scattering from tree trunks consider the geometry of the problem as shown in Fig. 3.3. The

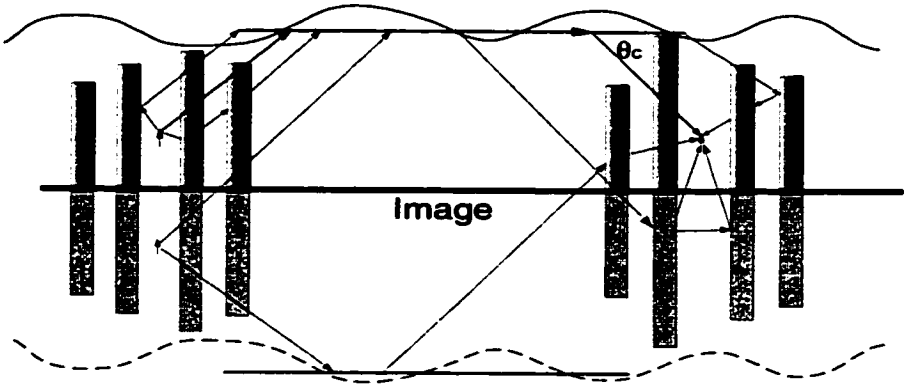

Figure 3.3: Scattering mechanisms resulted from wave interaction with tree trunks in a forest environment.

source and its image excite polarization currents in the dielectric cylinders which in turn re-radiate and produce multiple scattering among the tree trunks and secondary lateral waves (lateral waves generated by scattering from the tree trunks) that arrive at the receiver. The sum of all lateral and the secondary lateral waves will be referred to as the total incident wave in the vicinity of all receiver. The total incident wave excites polarization currents within the dielectric cylinders (tree trunks) near the receiver, which re-radiate and together with the total incident fields constitute the total field at the receiver. A formal solution to the problem can be obtained rather easily by casting the formulation in terms of an integral

equation for the polarization currents induced inside the dielectric cylinders. However, the brute-force solution of the integral equation using the method of moments is not tractable because of the large number of unknowns and the complex nature of the dyadic Green's function of the problem. To make the problem tractable an accurate approximate solution is sought. An accurate approximate solution, considering the physics of the problem, can be obtained as will be shown in the following section.

3.3 Reduced Problem

As mentioned before, estimation of field fluctuations in a forest environment requires the computation of multiple scattering effects, as well as the interaction of lateral waves with large number of dielectric cylinders. It is expected that the induced polarization currents in cylinders near the source be much stronger than those in cylinders distant from the source. Also the contribution to the received fields from cylinders in the vicinity of the receiver is expected to be high. Although the contribution to the scattered fields from individual cylinders between the transmitter and receiver which are not in the close proximity of the either is relatively small, one may argue that there are many such cylinders and the overall contribution may be significant. Considering the path-length between the transmitter to a cylinder and from the cylinder to the receiver, and noting that the scattering is strongest in near forward direction, the scattered fields from these cylinders arrive almost in-phase. Therefore the scattered field from cylinders that are not close to the receiver and transmitter are not expected to contribute to the field fluctuations significantly. The effect of these scatterers may be accounted for by replacing them with an effective dielectric constant. To examine the validity of these postulations, a 2-D medium consisting of infinite cylinders, excited by line source, is considered. Figure 3.4(a) shows the geometry of the problem where a line source capable of supporting z-directed current (TM case) or ρ-directed current (TE case) is used as the transmitter. Figure 3.4(b) shows the geometry

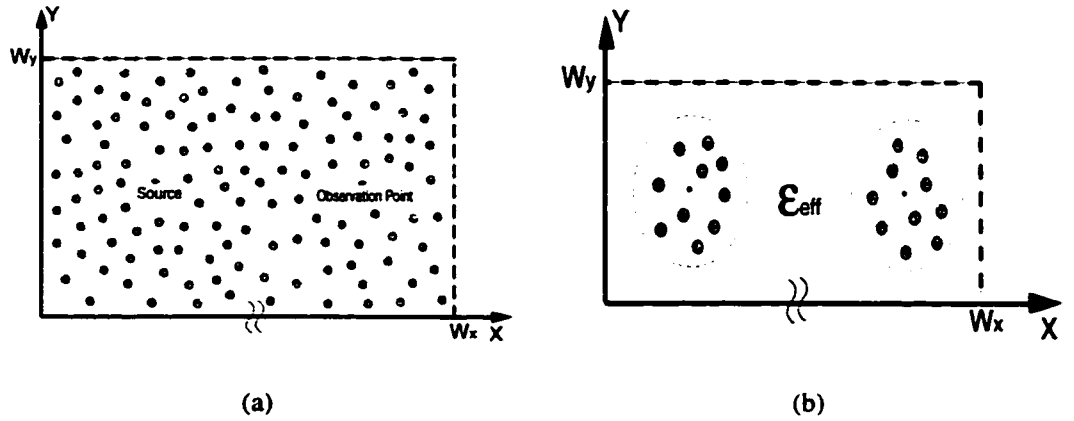

Figure 3.4: A 2-D random medium consisting of cylinders (a) and its statistically equivalent model (b). Also shown is a fictitious boundary used for the Monte Carlo simulation. (a) Complete Problem (b) Reduced Problem.

of the reduced problem where the scatterers that are not close to the receiver and transmitter are replaced with a effective dielectric constant. Our objective here is to show that the mean and variance of the field in the original problem and the reduced problem are the same. The method of moments is used to solve these problems for a given arrangement of cylinders. Then using Monte-Carlo simulation, the desired field statistics are computed. In the implementation of the Monte-Carlo simulation, the boundaries of the medium must be varied randomly by a few wavelengths to avoid coherence effects [32]. Position of cylinders are determined by a random number generator. In this filling process the distance of a new cylinder is measured from the previous ones to ensure a minimum distance between the tree trunks. The filling process for each medium realization is continued until a desired number density is reached.

3.3.1 The Method of Moments for M-body Sparse Scatterers

In this section a numerical technique based on the method of moments appropriate for a relatively large number of sparsely distributed dielectric cylinders, illuminated at oblique incidence is described. The integral equation formulation for the induced polarization cur-

rent for infinite cylinders whose axes are parallel to the z-axis is given by

$$\frac{1}{\varepsilon_r - 1}\vec{\mathbf{J}}(\vec{\rho}) = -jk_0 Y_0 \vec{\mathbf{E}}^i + \sum_{n=1}^{N} \int_{s_n'} \bar{\bar{G}}(|\vec{\rho} - \vec{\rho}'|) \cdot \vec{\mathbf{J}}(\vec{\rho}')ds' \tag{3.2}$$

where $\vec{\mathbf{E}}^i$ represents the incident field having a propagation constant k_0, ε_r is the relative dielectric constant of the cylinders and s_n' is the cross section of the nth cylinder. The explicit expression for the dyadic Green's function is given by

$$\bar{\bar{G}}(|\vec{\rho} - \vec{\rho}'|) = \frac{j}{4}\begin{bmatrix} k_0^2 + \frac{\partial^2}{\partial x^2} & \frac{\partial^2}{\partial x \partial y} & -jk_z\frac{\partial}{\partial x} \\ \frac{\partial^2}{\partial x \partial y} & k_0^2 + \frac{\partial^2}{\partial y^2} & -jk_z\frac{\partial}{\partial y} \\ -jk_z\frac{\partial}{\partial x} & -jk_z\frac{\partial}{\partial y} & k_\rho^2 \end{bmatrix} H_0^{(1)}(k_\rho|\vec{\rho} - \vec{\rho}'|) \tag{3.3}$$

where k_z is the propagation constant of the incident wave along the z-axis, and $k_\rho = \sqrt{k_0^2 - k_z^2}$. Following the standard procedure of the MoM, the cross section of the cylinders are discretized into small cells over which the current distribution may be considered a constant vector. Using point matching, the integral equation (3.2) can be cast in terms of a matrix equation of the form

$$\bar{\bar{\mathbf{Z}}} \cdot \vec{\mathbf{J}} = \vec{\mathbf{V}} \tag{3.4}$$

where $\bar{\bar{\mathbf{Z}}}$ is known as the impedance matrix. The size of the impedance matrix is proportional to the total number of cells for all N cylinders and is a limiting factor with regard to computer memory. Noting that in a fully-grown forest, the tree trunks are sparsely distributed, storage of all elements of $\bar{\bar{\mathbf{Z}}}$ can be avoided. In this case, the impedance matrix of the individual cylinders (block diagonal elements) are computed and stored. This can be limited to a few matrices corresponding a small number of cylinder, with different radii that represents the variability in tree trunk diameters. Next the impedance matrix elements or the pairwise interaction between the cells at the center of the cylinders are computed and stored. The interaction between other elements are computed in an approximate manner

as needed in the program and are not stored. For further clarification, consider the ith and

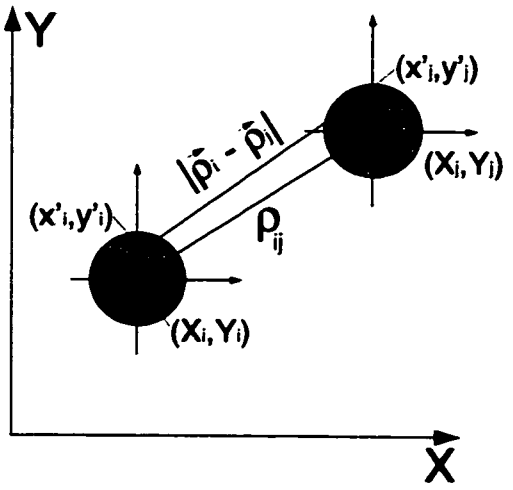

Figure 3.5: Global and local coordinate systems used in the MoM formulation of sparse scatterers.

the jth cylinders in the global coordinate system whose centers are respectively located at (X_i,Y_i) and (X_j,Y_j) as shown in Fig. 3.5. Suppose the interaction between two cells, whose local coordinate in the ith and jth system are respectively given by (x_i',y_i') and (x_j',y_j'), are needed. In this case, using the Taylor series expansion,

$$|\vec{\rho}_i - \vec{\rho}_j| \approx \rho_{ij} + \frac{(X_i - X_j)(x_i' - x_j')}{\rho_{ij}} + \frac{(Y_i - Y_j)(y_i' - y_j')}{\rho_{ij}} \tag{3.5}$$

where $\rho_{ij} = \sqrt{(X_i - X_j)^2 + (Y_i - Y_j)^2}$ is the distance between the centers of the cylinders. The approximation in (3.5) can be used in the evaluation of integrals needed for the computation of matrix elements. For example,

$$\begin{aligned} I_{i'j'} &= \int_{x_j'-\Delta/2}^{x_j'+\Delta/2} \int_{y_j'-\Delta/2}^{y_j'+\Delta/2} H_0^{(1)}(k_\rho |\vec{\rho}_i - \vec{\rho}_j|) dx' dy' \\ &\approx \alpha_n H_0^{(1)}(k_\rho \rho_{ij}) \cdot e^{i\Phi_{i'j'}} = I_{ij} \cdot e^{i\Phi_{i'j'}} \end{aligned}$$

where $\Phi_{i'j'} = k_\rho \left[(X_i - X_j)(x_i' - x_j') + (Y_i - Y_j)(y_i' - y_j') \right] / \rho_{ij}$, and $\alpha_n = \Delta^2 \left[1 - \frac{(k_\rho \Delta)^2}{24} \right]$. As mentioned earlier I_{ij} is stored and $I_{i'j'}$ is computed as needed . Using a sparse matrix

Stored Components	Size
Imp. Matrix of individual cylinder	$M \times M$: TM, $2M \times 2M$: TE
$k_\rho(X_i - X_j)/\rho_{ij}, k_\rho(Y_i - Y_j)/\rho_{ij}$	M(M - 1) array
$\Phi_{i'j'}$	M(M - 1) array
$\cos^2\theta_{ij} - \sin^2\theta_{ij}$	M(M - 1)/2 array

Table 3.1: Stored matrices and arrays for the implementation of M-body sparse scatterers.

storage scheme [33] and storing a small number of terms like, $(X_i - X_j)/\rho_{ij}$, $(Y_i - Y_j)/\rho_{ij}$, $(x'_i - x'_j)$ and $(y'_i - y'_j)$, the needed memory size is reduced. Similarly for other terms of the dyadic Green's function that require spatial derivatives, we can use the following approximations:

$$\left(\frac{\partial^2}{\partial u^2} + k_\rho^2\right) I_{i'j'} \approx \frac{\alpha_n k_\rho^2}{2}\left\{H_0^{(1)}(k_\rho\rho_{ij}) \pm H_2^{(1)}(k_\rho\rho_{ij})[\cos^2\theta_{i'j'} - \sin^2\theta_{i'j'}]\right\} \cdot e^{\Phi_{i'j'}} \quad (3.6)$$

where the positive and negative signs are used for $u = x$ for $u = y$, respectively. Also in (3.6)

$$\cos^2\theta_{i'j'} - \sin^2\theta_{i'j'} \approx \frac{\cos^2\theta_{ij} - \sin^2\theta_{ij} + (a_1 - a_2)/\rho_{ij}}{1 + (a_1 + a_2)/\rho_{ij}^2},$$
$$a_1 = 2(X_i - X_j)(x'_i - x'_j), \quad a_2 = 2(Y_i - Y_j)(y'_i - y'_j) \quad \theta_{ij} = \tan^{-1}\left[(Y_i - Y_j)/(X_i - X_i)\right]$$

Moreover

$$\frac{\partial I_{i'j'}}{\partial u} \approx \frac{\alpha_n k_\rho^2}{2}\left[H_0^{(1)}(k_\rho\rho_{ij}) + H_2^{(1)}(k_\rho\rho_{ij})\right](u_{i'} - u_{j'}) \cdot e^{\Phi_{i'j'}}$$

for $u = x$ or y. Finally for the $\frac{\partial^2 I_n}{\partial x \partial y}$ term, we can use

$$\frac{\partial^2 I_{i'j'}}{\partial x \partial y} \approx \frac{(X_i - X_j)(Y_i - Y_j) + (X_i - X_j)(y'_i - y'_i) + (Y_i - Y_j)(x'_i - x'_j)}{\rho_{ij}^2 + (a_1 + a_2)} k_\rho^2 H_2^{(1)}(k_\rho\rho_{ij}) \cdot e^{\Phi_{i'j'}}$$

Table 3.1 shows the sub-matrices and arrays that are stored in this scheme for M identical cylinder, each discretized into N pixels.

3.3.2 Statistically Equivalent 2-D Medium

In this section, a complete MoM solution for a large number of cylinders is used to verify the conjectures mentioned for the reduced problem. However before presenting these results, the accuracy of the approximate MoM solution for the M-body, sparse scatterers problem is evaluated. An array of 50 equally spaced dielectric cylinders with $\varepsilon_r = 5 + j$ and radius 0.3m are arranged along y-axis with a spacing of 2m. This array is illuminated by a 50MHz plane wave at an oblique incident angle $\theta = 60^o$ and TE polarization. The scattered field computed by the exact MoM and the approximate MoM are compared along the curve, $y = x\ln x$. Small discrepancies are observed between the two solutions which are plotted in Fig. 3.7 as relative percentage error. Many other cases were also examined and it was found that when the average ratio of cylinder spacing to cylinder radius is larger than 5, the approximate MoM is capable of producing very accurate results. Having confidence in the approximate MoM algorithm, simulation of wave propagation in a sparse random medium is carried out. A large number of dielectric cylinders (2000) confined in a rectangular box as shown in Fig. 3.4, are considered. The box is chosen to have average dimensions of 50m $\times$ 800m. As mentioned earlier, to eliminate the coherence effect of finite box size (see [32]) the dimension of the box is varied by at least one wavelength in the Monte Carlo simulation. A line source is used as the transmitter, at location (x = 20, y = 25) and the field is calculated at a point located at (x = 780, y = 25). Many sample media are generated and the MoM solution for each sample is used to construct approximate statistics of the field at the receiving point. In specifics, the mean and standard deviation (SDV) of the field is monitored and the simulation is continued up until a convergence is reached. The contribution to the total mean-field and standard deviation from scatterers in range bins of 20m wide are stored separately and are plotted in Fig. 3.8, for three frequencies of 10, 30, and 50MHz. It is interesting to note that the contribution to the total standard deviation (field fluctuations) are mainly dominated by the scatterers near the source and observation points. This indicates that scatterers between, but not close to, the

transmitter and receiver are not significant sources of field fluctuations and can be replaced with an effective dielectric constant. The geometry of the reduced problem is shown in Fig. 3.4(b) where 600 cylinders near the source and 250 cylinders near the observation point are kept and the rest are replaced with an effect dielectric medium. In this simulation a cylinder density $0.05/m^2$ is used and the comparison of standard deviation for the complete and reduced problems for the TM case is shown in Fig. 3.9. As can be seen in Fig. 3.9 the reduced and complete problems produce effectively the same field variations. To examine the field variance only, far less scatterers produce the same result. Figures 3.10(a), 3.10(b),and 3.10(c) show respectively the field variance for TE (3.10(a), and 3.10(b)) and TM (3.10(c)) excitation using 200 cylinders near the source and 150 cylinders near the receiver. For these simulations cylinder density $0.01/m^2$ is used. For the reduced problem, the effective medium is anisotropic and its dielectric constant is a tensor given by [32],

$$\begin{aligned} \varepsilon_{eff} &= \varepsilon_h + (\varepsilon_i - \varepsilon_h) f \qquad \text{for TM} \\ \varepsilon_{eff} &= \varepsilon_h + \frac{2f(\varepsilon_i - \varepsilon_h)}{\varepsilon_i + \varepsilon_h} \qquad \text{for TE} \end{aligned}$$

3.4 Fast Field Calculation Based on Reciprocity

As our goal in this investigation is the computation of the fields of a dipole in a forest environment, computation of polarization currents in tree trunks when illuminated by the dipole is needed. Even with the simplification mentioned in the previous section, a 3-D scattering problem which includes more than 200 cylinders is not tractable numerically. In this section, we demonstrate a procedure where, with the help of reciprocity theorem, the 3-D scattering problem is first reduced to an equivalent 2-D problem, which is then solved by the method of moments. To demonstrate this procedure, let us first consider a short dipole near a single cylinder as shown in Fig. 3.6. The field at the receiver is the

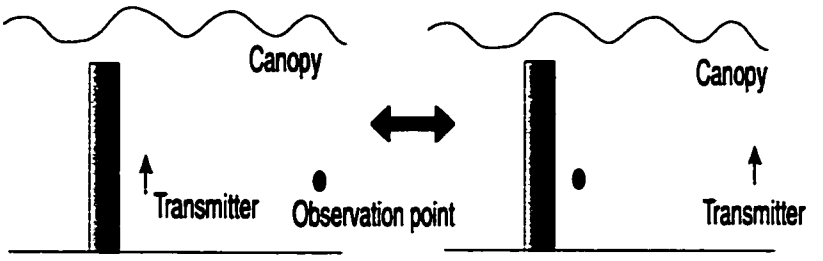

Figure 3.6: Application of reciprocity theorem for the computation of scattered field of cylinder from a nearby dipole embedded in a dielectric slab above ground plane.

sum of the field of the dipole and the radiated field from the polarization current induced in the dielectric cylinder embedded in the canopy above the ground. Since the observation point is in the far-field of the cylinder and the dipole, reciprocity can be applied to simplify the problem. According to the reciprocity theorem [34], the vertical component of the received field for a dipole excitation with orientation $\hat{l}$ is equal to the $\hat{l}$ component of the field near the cylinder of the same dipole oriented vertically and located at the observation point. According to (3.1), the field of the dipole (in the modified problem) illuminating the dielectric cylinder is locally plane wave. Also noting that the induced polarization currents in a finite, long dielectric cylinder is approximately the same as those of an infinite cylinder having the same radius and dielectric constant [18, 35], the MoM solution for 2-D problems can be used to find the induced polarization currents. Once this polarization current is obtained, the near field can easily be computed and the expression for it given in the Appendix A. The same procedure is applied to find the contribution of all cylinders in the vicinity of the transmitter, at the receiver. To compute the effect of the scattered field of cylinders near the receiver, the fields of the dipole and all cylinders in its vicinity are computed at each cylinder location near the receiver. Again these fields are locally plane waves illuminating tree trunks near the receiver at an oblique incidence equal to the critical angle. MoM is used to find the induced polarization current in cylinders near the receiver from which the scattered field is computed. Hence the contribution from all cylinders near the transmitter and receiver are included. To account for the effect of the forest floor, the

geometric optics images of the dipole and lateral waves on the ground plane are considered and their contributions are evaluated using a similar procedure. It is worth mentioning that in this case, the number of cylinders which need to be kept in the vicinity of the transmitter and receiver for the reduced problem is expected to be smaller than what was obtained for the 2-D problem. Basically for the dipole excitation where the finite tree trunks are illuminated by the resulting plane waves at oblique incidence, fewer number of cylinders can interact with each other.

3.5 Numerical Simulation

Based on the rigorous electromagnetic model described in the previous section, a very accurate propagation model which provides a complete channel characterization of forest media is possible through Monte Carlo simulations. To examine the effect of tree trunks on the field of a transmitter in a forest, we first consider a single tree trunk in the near-field of a short dipole. For this example a dielectric cylinder with permittivity $\varepsilon = 5 + j$, radius a = 35cm , and height h_c = 15m is considered in a forest with a canopy having $\varepsilon_{eff} = 1.03 + j0.036$ and height H = 20m. A vertical dipole transmitting at 90MHz is placed at a distance of 10cm from the surface of the cylinder and is moved up and down, and around the cylinder and its field is computed at an observation point 1km away from the cylinder and 5m above the ground plane. Figure 3.11 shows the normalized z-component of the field at the receiver as a function of dipole height above the ground and for three azimuthal angles around the cylinder. The normalization here is with respect to the field of the dipole in the absence of the cylinder. It is shown that the field at the receiving point fluctuate as the dipole is moved along the cylinder axis. This fluctuation is a result of constructive and destructive interference of the direct field, scattered field from the cylinder, and their images on the ground plane. Since the cylinder radius is small compared to the wavelength a gentle variation is observed as the dipole is moved around the cylinder. It is

interesting to note that for most dipole locations, existence of the cylinder in the near-field region of the dipole enhances the field at the receiver since the tree trunk acts as a passive radiator. Next, computation of path-loss and field standard deviation is considered for the forest of the previous example. In this case tree trunks having an average height 15m and height standard deviation of 1m with number density $0.05/m^2$ and dielectric constant of $\varepsilon = 5 + j$ are also included. As mentioned before, the number of cylinders we need to keep for the reduced problem is expected be smaller than those for the 2-D problem. Here we kept 200 cylinders near the transmitter located at the origin 3m above the ground and 50 cylinders near the receiver located 1km away from the transmitter and 5m above the ground. Table 3.2 shows the path-loss (with respect to the free-space) of the normal component

	Path-loss(dB)		**SDV/Mean(dB)**	
Antenna Configuration	200 cyl.	390cyl.	200 cyl.	390 cyl.
single dipole	47.5	48.16	1.42	1.16
4-element Broadside	48		3	
4-element End-fire	59		2.45	

Table 3.2: Path-loss and standard deviation-to-mean ratio of the field of a vertical dipole and 4-element dipole arrays in the forest with $\varepsilon_{eff} = 1.03 + j0.036$, canopy height H = 20m, tree density $0.05/m^2$, and tree trunk height of h = 15m.

of the wave and its standard deviation at 50MHz for a vertical dipole. Also shown in Table 3.2 are the path-loss and standard deviation if 390 cylinders (250 near the source and 140 near the receiver) are kept. The Monte-Carlo simulation converges after about 30 realizations and is shown that the results based on 200 cylinders is very close to those based on 390 cylinders. This convergence test indicates that a moderate number of scatterers (about 200) is sufficient for accurate characterization of field variance. The results also indicate a standard-to-mean ratio deviation of almost unity for the random variable E_z. Using different forest parameters and frequencies (at HF band) random variable E_z showed a similar behavior. That is the statistics of the channel follows Ricean statistics with a standard deviation-to-mean ratio ranging from 0.5 - 2. This is different than Rayleigh statistics which is commonly assumed for communication channels when there is no line-

of-sight propagation path. Significant non-zero mean-field in this case is a direct result of contributions from the lateral wave.

For communication channels with significant multi-path, antenna arrays are usually used to mitigate fading. In this case, because of the existence of a considerable coherent mean-field, antenna arrays may provide coherent gain. To investigate the performance of antenna arrays in a forest environment two basic configurations, namely, broadside and end-fire are considered. For the broadside configuration four vertical dipoles are arranged along a line perpendicular to the line between the transmitter and receiver points with a spacing of $\lambda/2$. The four elements of the end-fire array are placed along the line between the transmitter and receiver separated by $7\lambda/16$ and having a progressive phase factor of $-7\pi/8$ [36]. The field of these two arrays are evaluated and the path-loss and SDV-to-mean ratio is reported in Table 3.2. It is found that the broadside array has about 11dB less path-loss than the end-fire array. This is very close to the 12-dB gain of a 4-element array and indicates that the field of all four elements of the broadside array arrive at the receivers almost coherently whereas those of the end-fire array are incoherent. This behavior can be understood by considering the spatial correlation function in the forest environment. The spatial correlation coefficient between two points $\vec{r}_1$ and $\vec{r}_2$ is defined as [37]

$$C_s(\vec{r}_1,\vec{r}_2) = \frac{\mathrm{Cov}\left[\vec{E}(\vec{r}_1),\vec{E}(\vec{r}_2)\right]}{\sigma_{E_1}\sigma_{E_2}}$$

where σ_{E_1} and σ_{E_2} are the variance of the field at $\vec{r}_1$ and $\vec{r}_2$ respectively. A grid of nine points along x-axis (direction between the transmitter and receiver) and nine points along y-axis separated by $\lambda/2$ that is 1km from the transmitter is generated and components of the electric field are calculated many times for different cylinder arrangements in order to compute the correlation coefficient. Figures 3.12(a) and 3.12(b) show the magnitude and phase of $C_s(\vec{r}_1,\vec{r}_2)$ along the x- and y-axis respectively. It is shown that the signal along y-axis remains coherent over much larger distance than along x-axis. This result is in agreement

with the observed behavior of broadside and end-fire antenna arrays. Sampling theorem [38, 37, 39] is used to generate the smooth curves that goes in between the discrete points in Figures 3.12.

To study the path-delay effects, the impulse response of the channel must be characterized. The impulse response cannot be directly determined. However, by characterizing frequency response over a wide bandwidth the impulse response can be determined by applying the Fourier transformation to generate time domain (range) information. Direct application of FFT is not computationally efficient considering the number of frequency points which are needed in order to avoid aliasing. For example, with a receiver at a distance of 1.5km from the transmitter a maximum frequency spacing of 200 KHz is required. A pulse width of 12.5 nsec corresponds to 80MHz bandwidth which can be used to resolve path delays 3.75m apart. In this case for each forest realization 400 frequency points must be simulated. To circumvent this difficulty we used a non-uniform frequency sampling scheme. Gauss quadrature integration [39] is used to evaluate the Fourier transform. The order of Legendre polynomial should be chosen so that the minimum distance between the zeros of the Legendre polynomial is smaller than the minimum frequency spacing required to avoid aliasing (200 KHz for the above example). Impulse response of the forest considered in the previous example is simulated at HF using a bandwidth of 10 - 90MHz. A receiver at a distance of 1km from the transmitter is considered. It is expected that the dispersion (pulse spreading) will be observed due to multiple scattering among tree trunks and the frequency dependent path-loss of lateral waves. Figure 3.13 shows the frequency response of the received field in the absence of the tree trunks and the ground plane for two cases: 1) smooth canopy-air interface and 2) rough canopy-air interface with a rms height 2m. The transmitter and receiver are 17m and 15 m below the interface and the effective dielectric constant of the canopy is $\varepsilon_{eff} = 1.03 + j0.036$, as before. It is shown that the canopy-air interface roughness increase the dispersion. Figure 3.14 shows the impulse response of the forest channel including tree trunks and the underlying ground plane. For the calculation of

the impulse response, Gauss quadrature method with 40 points is used over the frequency range of 10 - 90MHz. A Gaussian pulse is assumed to be transmitted which is also plotted in Fig. 3.14 for comparison. The amplitude of the transmitted pulse is multiplied by the path-loss and delayed by the free-space distance between the transmitter and receiver. As can be seen in Figure 3.14, pulse spreading and ringing are observed which are the result of dispersion and multipath. The last simulation demonstrates performance of different spatial diversity schemes. Three antennae 1.5λ apart are aligned x-axis placed 1km away from a transmitter operating at 50MHz in the forest. Three diversity schemes are examined: 1) selective diversity (SD), 2) equal gain combining (EG), and 3) maximal ratio (MR) combining [40]. In SD scheme the detector simply chooses the output of the receiver with the highest receiver power. In EG combining method the detector is provided with the averaged detected signal from each receiver (a weighting factor of $w_i = 1/3$ is used in the combining). In the diversity scheme based on maximal ratio combining a weighting factor proportional to the signal power is used to combine the signals from the receiver ($w_i = \frac{P_i}{\sum_{j=1}^{3} P_j}$). To assess the performance of the above-mentioned diversity combining methods, cumulative distribution function (CDF) of fading depth for each diversity scheme is calculated using a Monte-Carlo simulations. The fading depth is defined as power level at the output of each combiner (SD, EG, or MR) above the average power in dB ($10\log(|\vec{E}|^2/\langle|\vec{E}|^2\rangle)$). Figure 3.15 shows the CDF of fading depth for SD, EG, and MR combining methods. Also shown is the CDF of one of the channels. It is shown that the performance of all three diversity scheme is approximately the same for this problem.

3.6 Conclusion

A complete wave propagation model capable of predicting path-loss, time delay response, and coherent frequency response in a forest environment is developed. The model is based on a hybrid analytical and numerical approach which allows for efficient computa-

tion of important channel properties without compromising accuracy. The model accounts for multiple scattering among tree trunks and includes the effects of the forest ground plane. Branches and leaves are represented by an effective dielectric constant which limits the range of validity of the model up to UHF. Except for the path-loss calculation other statistical channel characteristics are determined using a Monte-Carlo simulation. In general, propagation simulations are slower at higher frequencies which depending on the computer platform also constitutes a limit for the highest frequency. The model is used to simulate performance of antenna arrays and different diversity schemes. It is shown that because of a significant non-zero mean-field, spatial diversity only improves the channel fading moderately and there is not a significant difference between different diversity combining schemes. The model presented in this chapter shows the possibility of constructing a very accurate physics-based propagation model capable of end-to-end channel simulations.

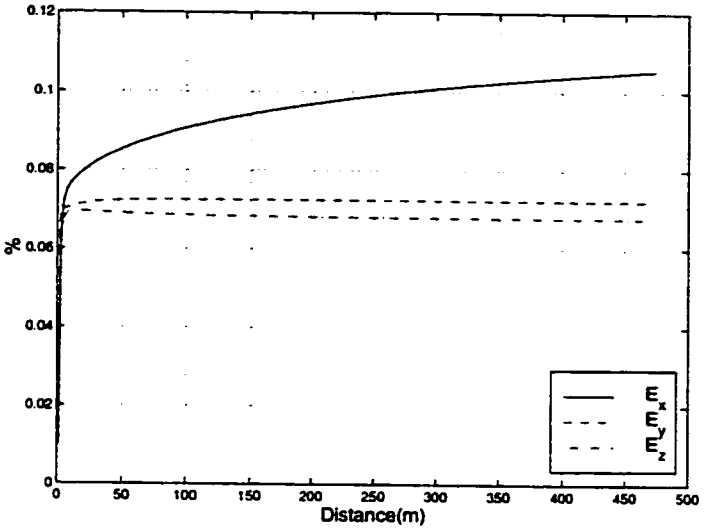

(a)

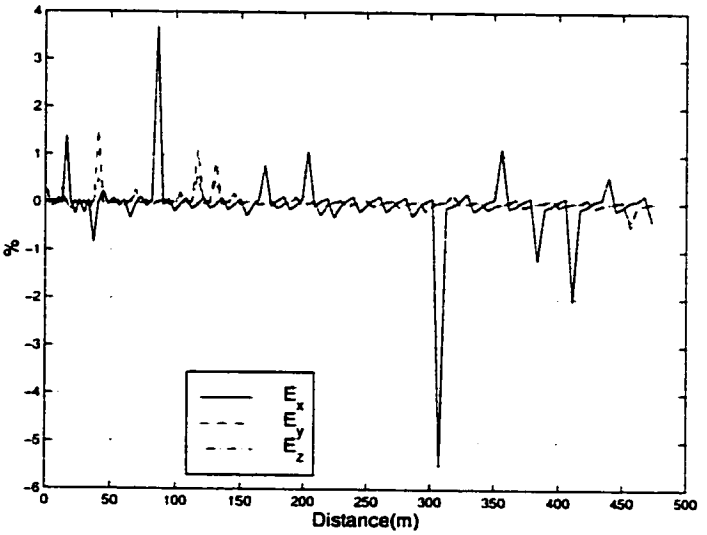

(b)

Figure 3.7: Relative percentage error in magnitude (a) and phase (b) of scattered electric field from 50 infinite dielectric cylinders that are located along y-axis with 2m separation when a TE plane wave is obliquely incident with $\theta = 60^o$ at 50 MHz.

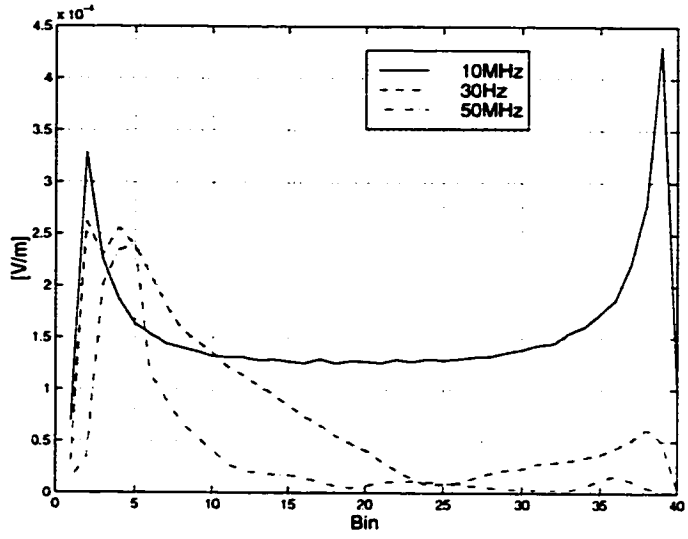

(a)

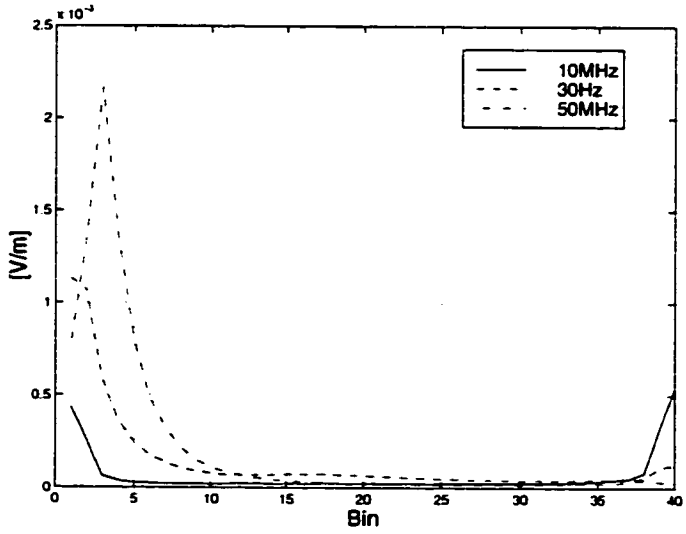

(b)

Figure 3.8: Mean and standard deviation of scattered electric field generated by scatterers in each 20m bin with TM source(x = 20, y = 25) and an observation point(x = 780, y = 25). Three different frequencies are used, 10, 30, and 50MHz and total number of scatterers is 2000. (a) Magnitude of mean (b) Magnitude of standard deviation.

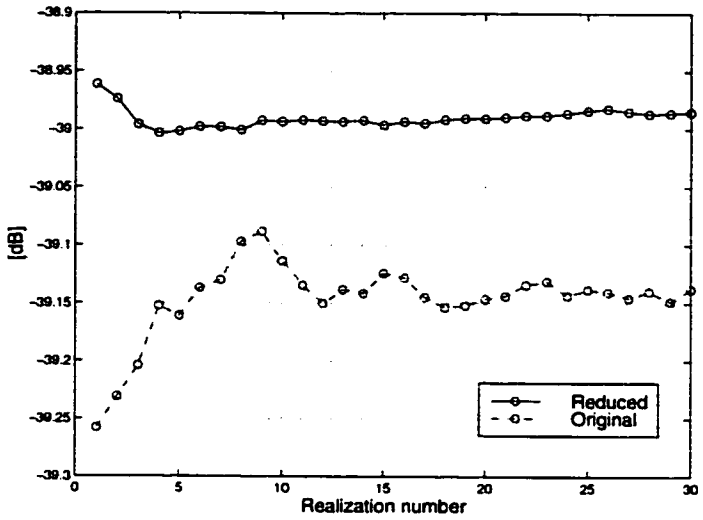

(a)

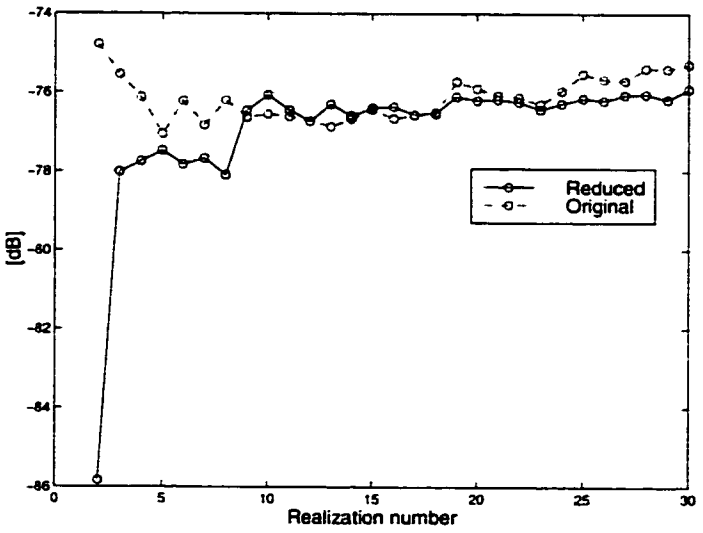

(b)

Figure 3.9: Comparison of the mean field (a) and standard deviation (b) of E_z of the reduced problem that keeps 600 scatterers near the source and 250 scatterers near the observation point with those of the complete problem that contains 2000 scatterers, with TM line source excitation.

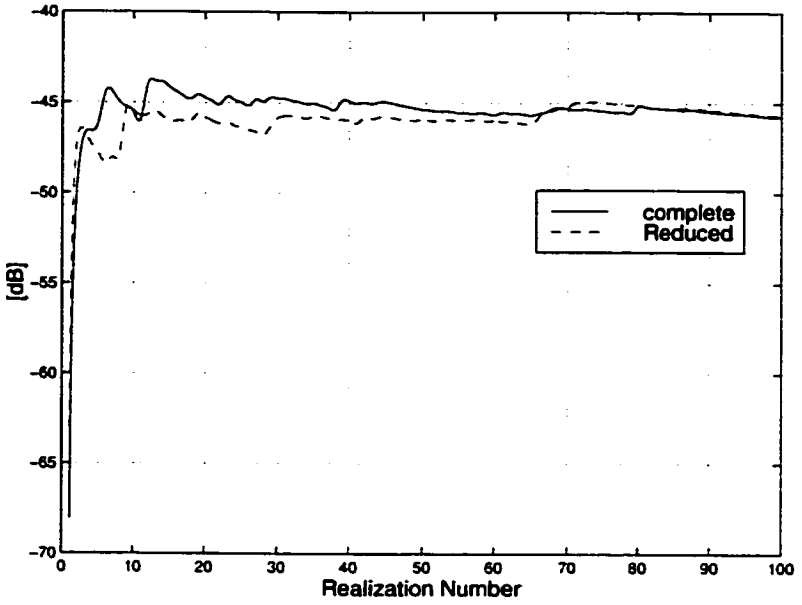
-40
-45
-50
-55
-60
-65
-70
[dB]
0
10
20
30
40
50
60
70
80
90
100
Realization Number
complete
Reduced

(a)

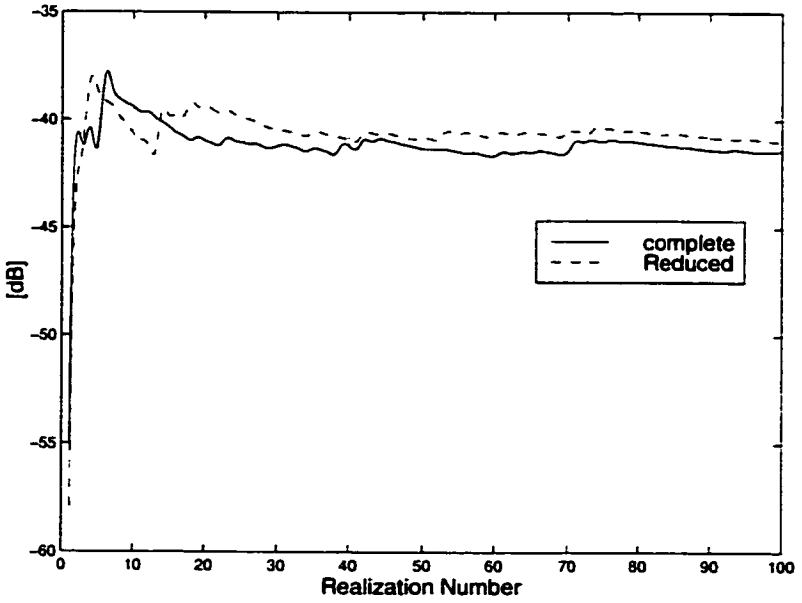
-35
-40
-45
-50
-55
-60
[dB]
0
10
20
30
40
50
60
70
80
90
100
Realization Number
complete
Reduced

(b)

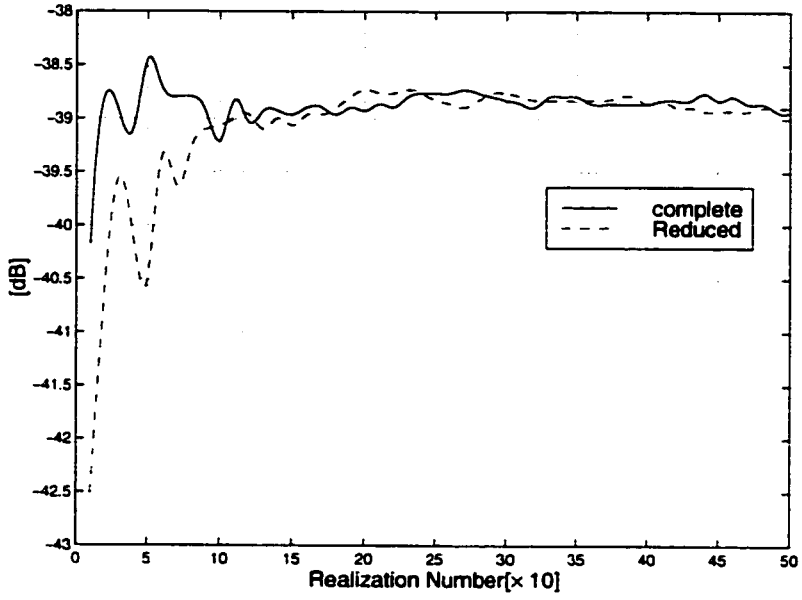

(c)

Figure 3.10: Comparison of the standard deviation for TE ((a) and (b)) and TM ((c)) excitations of the complete and reduced problems that keeps 200 (TE) or 150 (TM) scatterers near the source and 150 scatterers near the observation point with those of the complete problem that contains 500 scatterers, with TE line source excitation.

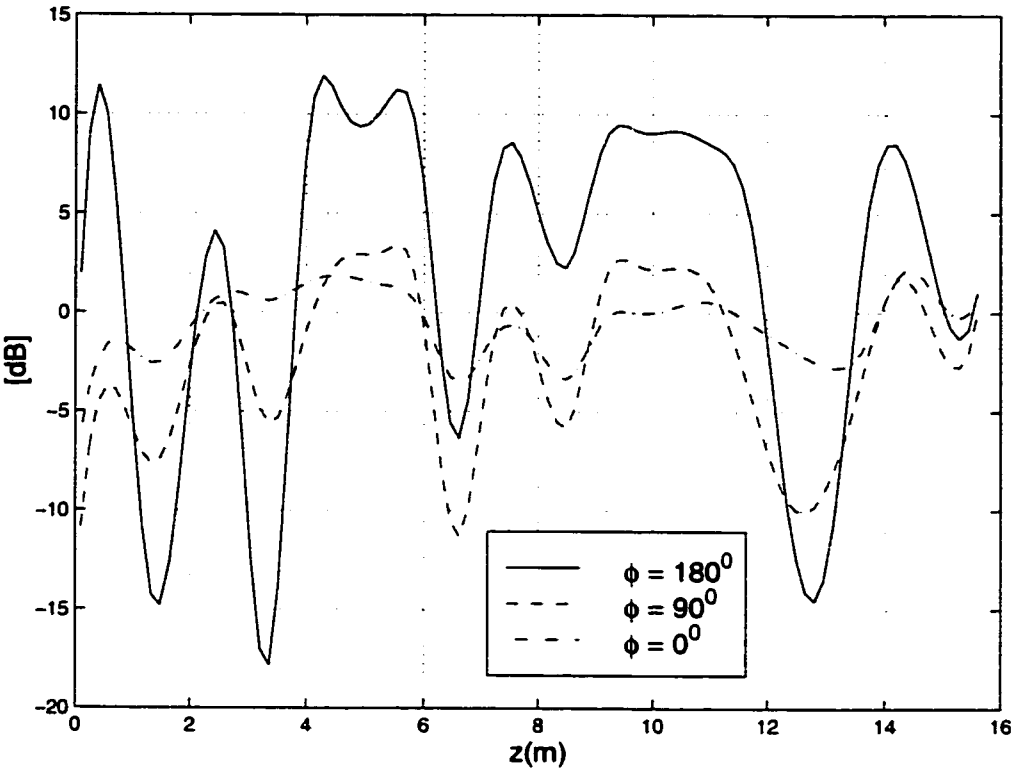

Figure 3.11: The ratio of the fields of a dipole with and without a tree trunk as a function of dipole height (z) and azimuthal angle around the cylinder. The dipole is vertical and 10cm away from the cylinder surface and observation point is 1km away.

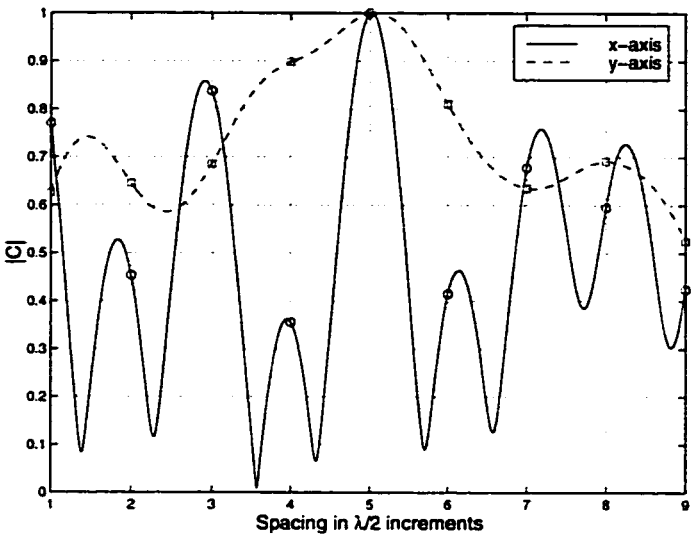

(a)

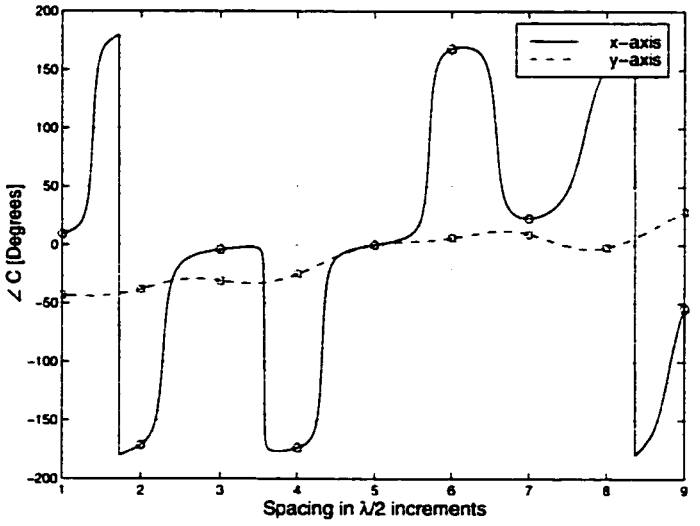

(b)

Figure 3.12: Spatial correlation of magnitude (a) and phase (b) of field of a vertical dipole (E_z) along x-axis and y-axis.

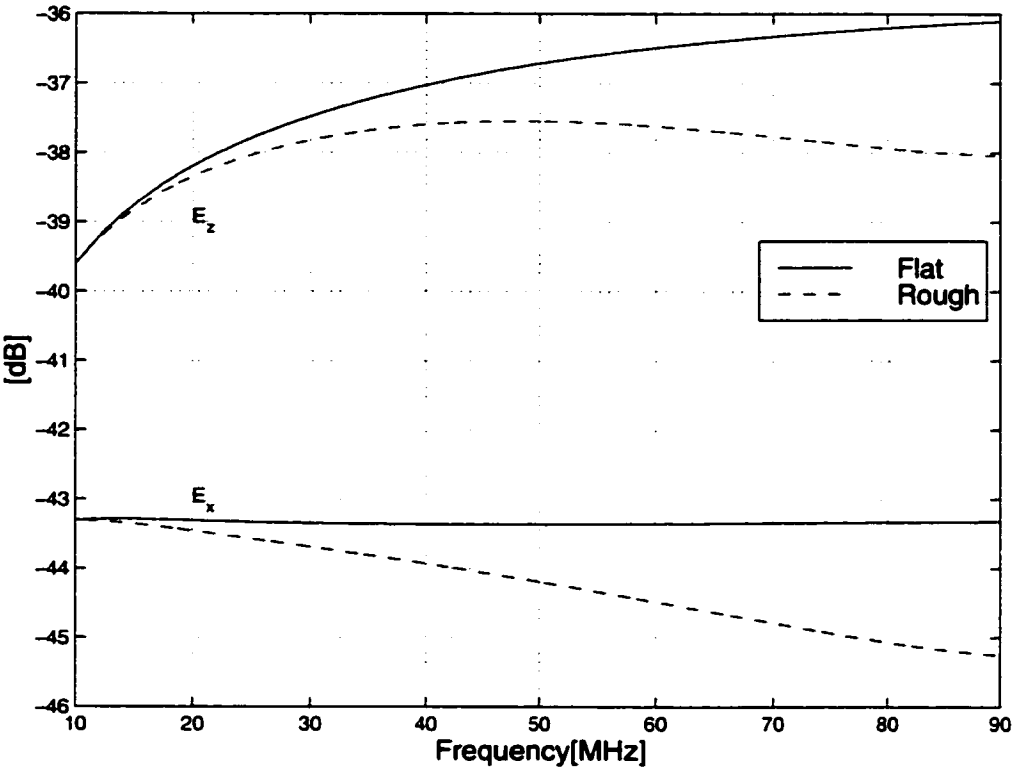

Figure 3.13: Magnitude of mean field as function of frequency in the absence of tree trunks and the ground plane. RMS height is 2m and $\varepsilon_{eff} = 1.03 + j0.0036$ and the transmitter and receiver are 17m and 15m below the canopy-air interface, respectively.

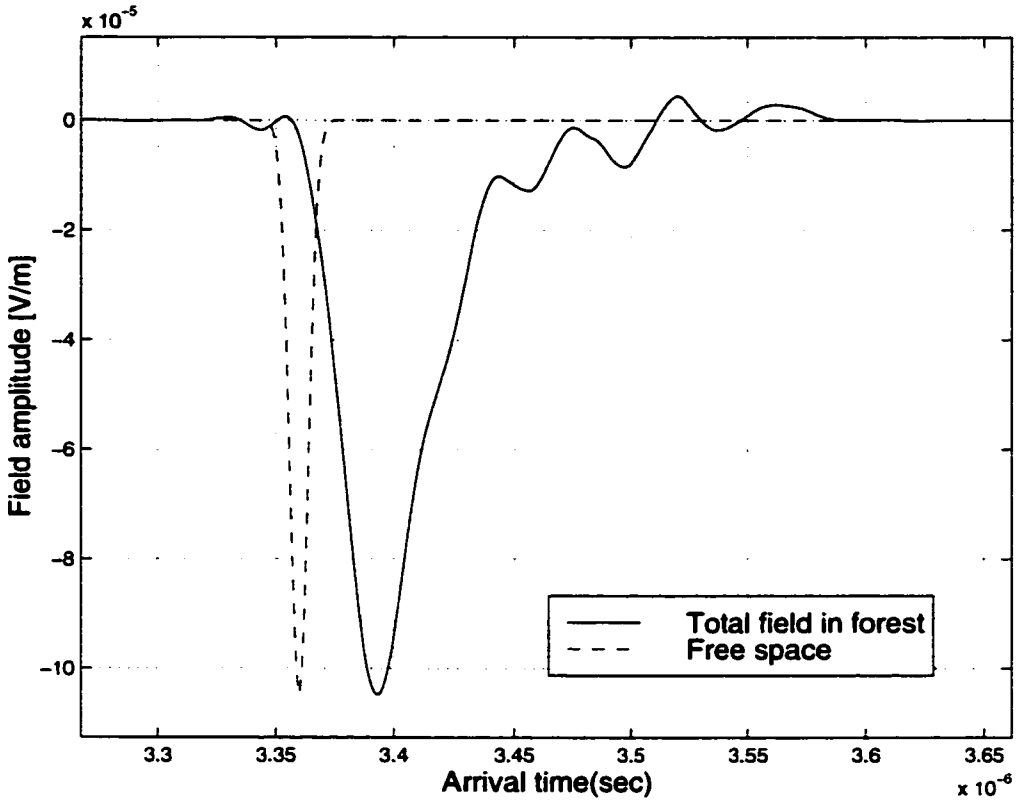

Figure 3.14: Impulse response with Gaussian pulse excitation on the $\hat{z}$ directed dipole. 40 non-uniformly spaced sampling points are used. Dot line is free-space response multiplied by the path-loss evaluated at 50MHz (see Table 2).

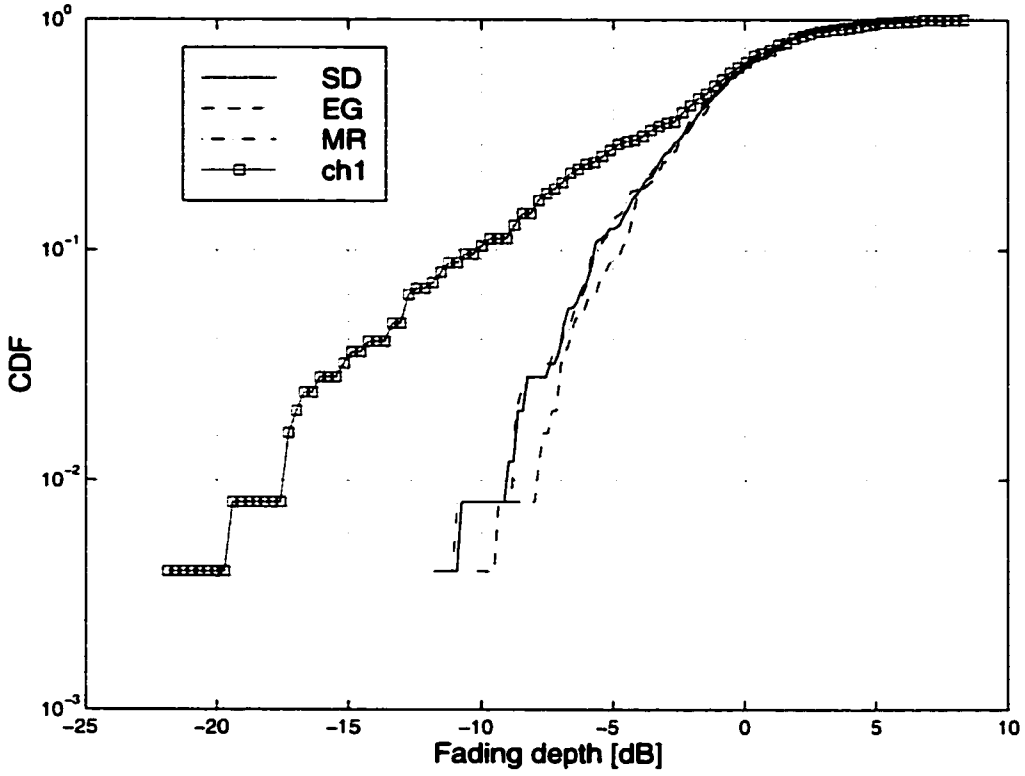

Figure 3.15: Cumulative distribution function(CDF) of fading depth for each diversity scheme when antenna arrays are long x-axis.

CHAPTER 4

A Novel Physics-Based Channel Model for Air-to-Ground communication in a Rural Environment

4.1 Introduction

Ground-to-air/satellite communication is a scenario with numerous civilian and military applications ranging from simple voice and data communications to navigation. In this scenario characterization of the channel is rather straightforward except for the urban environment or forested areas where significant scattering and shadowing may take place. In this chapter, the problem of channel characterization for a forested environment is considered. Using this model, performance of GPS receivers under tree canopies, and a narrow pulse transmission through a tree canopy are investigated as examples.

The Global Positioning System (GPS) was introduced by the Department of Defense (DoD) primarily for the U.S. military to provide precise estimation of position, velocity, and time. Since the early 1980's, the DoD has allowed GPS to be used for civilian applications. Because of the high price of GPS receivers in early years, the application of GPS for commercial purposes was limited mainly to civil aviation. In recent years however, mainly with the rapid development of the integrated circuit, the availability of low-cost receivers has significantly broadened the application domain of the GPS, such as land transportation,

surveying and mapping, agriculture, earth sciences, etc [41]. Each GPS satellite transmits a right hand circularly polarized L-band signal at two frequency bands known as L1 (1.57542GHz) and L2 (1.2276GHz). For a commercial use, the L1 signal is modulated by a pseudo-random noise (PRN) code called the Coarse/Acquisition (C/P) code which is a 1023 Gold code with a chip rate of 1023 Mchips/s (Mcps) and its null-to-null bandwidth is 2.046MHz [42]. When this signal reaches the earth's surface, the level is very weak and therefore the receiver performance may be severely degraded if a line-of-sight (LOS) transmission is not established.

The literature concerning interaction of electromagnetic waves and vegetation can be categorized into two groups, namely, papers related to radar remote sensing of vegetation [18, 35, 43, 44, 45] and papers related to communications [9, 46, 47]. The thrust of remote sensing articles is on the modeling of vegetation scattering when both the transmitter and receiver are in the far field region of the illuminated canopy and the interest is usually in the calculation of the mean backscatter power. In the communication problem where the transmitter or receiver, or both are within the canopy, the field calculations and the mechanisms responsible for the dominant field at the receiver are very different. For example when both the transmitter and receiver are embedded in the canopy, there is a non-vanishing dominant mean-field at frequencies below UHF as explained in the previous two chapters. Wave propagation over relatively long distances at UHF and higher where both the transmitter and receiver are embedded in a forest canopy is not possible due to exorbitant propagation path-loss. At these frequencies either the transmitter or the receiver must be outside the canopy. Field calculations for this scenario are complicated because of the close proximity of the receiver (transmitter) to relatively large scatterers, which can cause significant field attenuation and fluctuation.

In what follows development of an accurate model that describes the propagation of electromagnetic waves through foliage is considered. In Section 4.2 the overall structure of the coherent channel model based on a single scattering theory and Monte-Carlo simu-

lation is presented. Also an analytical approximate scattering formulation for an arbitrarily oriented finite dielectric cylinder above a ground plane, which can represent tree trunks and branches, is provided. This new formulation is a building block for the channel model and provides a uniform expression for the scattered field which is valid for observation points near and far from the cylinder. Finally in Section 4.3, numerical simulations are presented showing the effects of foliage on the GPS signal. Quantities such as the signal path-loss, statistics of the received polarization, and the first-order statistics of the electric field for both horizontally and vertically polarized incident waves are calculated. In addition, the effect of the tree canopy on an ultra-wideband signal is investigated.

4.2 Forest Model

From electromagnetic scattering point of view, a tree can be considered as a complex structure composed of a group of randomly oriented scatterers structured in a semi-deterministic fashion with electrical characteristics very much dependent on their moisture content. At UHF frequencies and higher, dimensions of tree trunk, the primary and secondary branches, or even leaves and twigs can be much larger than or comparable to the wavelength. Noting that a relatively large cluster of trees around an observation point significantly contribute to the total field at the receiver, field calculations based on brute force numerical techniques are not possible at microwave frequencies or higher. However, if the multiple scattering among branches and leaves is ignored, a single scattering model can be constructed. To a high degree of accuracy this model can predict the first order statistics of the total field within a forest. This is because through the averaging process the dominant portion of the total field (coherent effect) can survive, and the multiple interaction is minimized. In modeling the forest, one approach is to distribute the vegetation particles (leaves and branches) uniformly, however, it is found that for frequencies up to about 3 GHz it is important to preserve the structural information of tree canopies for accurate prediction of

radar backscatter [43]. This effect is expected to be even more important when the observation point is within the forest. Basically, not only the coherence of the scattered fields from the vegetation structure must be preserved, but also the near-field effects of lower branches and tree trunks near the observation point must be accounted for very accurately.

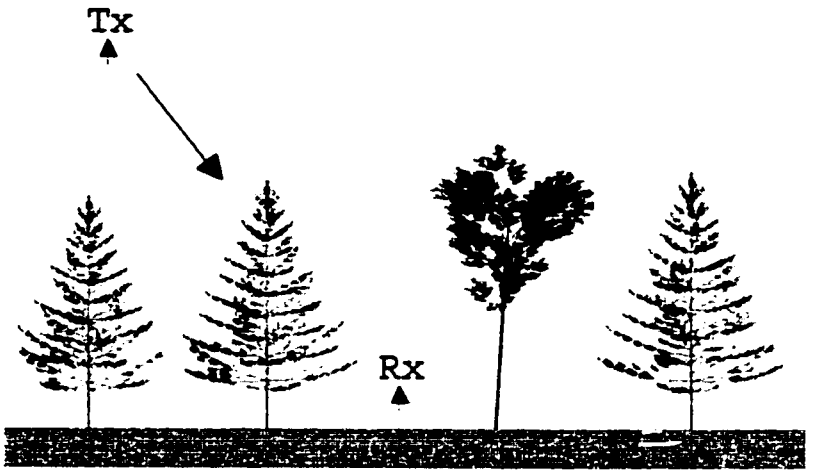

Figure 4.1: The problem geometry where a receiver inside a forest is communicating with a transmitter above.

Figure 4.1 shows the geometry of the communication problem where a receiver (or a transmitter) embedded in a foliage is communicating with a transmitter (or a receiver) above the foliage layer. As the signal passes through the foliage, it experiences attenuation and scattering which depend on signal parameters such as frequency, polarization, and incidence angle as well as vegetation attributes such as tree type, density, and height. As mentioned earlier, to model the interaction of electromagnetic waves with vegetation accurately, tree structures must be modeled rather accurately. Considering the number of branches and leaves on a tree and the variability in their sizes and orientations, generating a tree structure can be a very difficult task. This can be done efficiently by approximating tree structures by fractal geometries. Here we use a statistical Lindenmayer system [43] in conjunction with botanical properties pertinent to a specified tree specie. In this model, the geometry of vegetation particles are also approximated by canonical geometries such as dielectric disks, needles, and layered dielectric cylinders. Each particle in the medium

is assumed to be illuminated by the incident wave, attenuated by the foliage along the ray between the particle and the canopy top. The attenuation through the foliage is calculated using Foldy's approximation [21] and single scattering theory is invoked to compute the field scattered from all vegetation particles and their images in the ground plane in the vicinity of the observation point. The total field is then obtained by adding all scattered field components coherently.

4.2.1 A Uniform Near-Field to Far-Field Expression For Scattering from Finite Dielectric Cylinders

A building block for simulated fractal trees are finite dielectric cylinders which can be used to represent tree trunks, branches, and twigs. To compute the scattered field from a fractal tree, an analytic or numeric scattering solution is needed. Unfortunately exact analytical solutions for finite dielectric cylinders do not exist. Numerical methods of course, can provide very accurate and general solutions for finite dielectric cylinders. However, considering the number of dielectric cylinders in a given tree and the fact that the length or the diameter of these cylinders may be comparable to or much larger than a wavelength, the computation time for the scattering solution becomes exorbitant. To circumvent this difficulty, an approximate analytical solution for the scattered field from a finite dielectric cylinder is formulated. For long cylinders (cylinders with large aspect ratio), significant scattered field exists only in a forward scattering cone (see Fig. 4.2(b)) [35]. Hence an accurate formulation for the scattered field in this region is of great interest. The formulation presented in this section provides very accurate results anywhere (from near-field to far-field) within and in the vicinity of the forward scattering region. This approximate solution is obtained by assuming that the equivalent surface electric ($\vec{\mathbf{J}}_e$) and magnetic ($\vec{\mathbf{J}}_m$) currents are the same as those of an infinite cylinder whose radius and dielectric constant are equal to those of the finite cylinder. It has been shown that approximate currents can provide accurate results in the far-field if the length of the cylinder is large compared to

both wavelength and cylinder radius ($L \gg \lambda$ and a), and the angle of incidence with respect to the cylinder axis is relatively large ($\beta \geq 10°$) [18, 35]. Analytic expressions for these currents are given by [18, 35]:

$$\begin{aligned}
\vec{\mathbf{J}}_e(\phi,z) &= \vec{\mathbf{J}}_e(\phi)e^{-jk_0z\cos\beta} \\
&= \sum_{m=-\infty}^{\infty}(-j)^m e^{jm\phi}\left[Q_{1m}Y_0(\sin\phi\hat{x}-\cos\phi\hat{y})+Q_{2m}\hat{z}\right]e^{-jk_0z\cos\beta} \qquad (4.1)\\
\vec{\mathbf{J}}_m(\phi,z) &= \vec{\mathbf{J}}_m(\phi)e^{-jk_0z\cos\beta} \\
&= \sum_{m=-\infty}^{\infty}(-j)^m e^{jm\phi}\left[-\bar{Q}_{1m}(\sin\phi\hat{x}-\cos\phi\hat{y})+\bar{Q}_{2m}\hat{z}\right]e^{-jk_0z\cos\beta} \qquad (4.2)
\end{aligned}$$

where k_0 is the free-space propagation constant, and $Y_0 = 1/Z_0$ is the free-space admittance. The terms, Q_{1m}, Q_{2m}, $\bar{Q}_{1m}$, and $\bar{Q}_{2m}$ are given by

$$\begin{aligned}
Q_{1m} &= h_zJ_m(x_0)+B_mH_m(x_0) \\
Q_{2m} &= -\frac{Y_0}{jk_0\sin^2\beta}\left\{k_0\sin\beta[e_zJ'_m(x_0)+A_mH'_m(x_0)]+\frac{jm\cos\beta}{a}[h_zJ_m(x_0)+B_mH_m(x_0)]\right\} \\
\bar{Q}_{1m} &= e_zJ_m(x_0)+A_mH_m(x_0) \\
\bar{Q}_{2m} &= -\frac{1}{jk_0\sin^2\beta}\left\{k_0\sin\beta[h_zJ'_m(x_0)+B_mH'_m(x_0)]-\frac{jm\cos\beta}{a}[e_zJ_m(x_0)+A_mH_m(x_0)]\right\}
\end{aligned}$$

where $x_0 = k_0a\sin\beta$, $e_z = \vec{\mathbf{E}}^i\cdot\hat{z}$, $h_z = Z_0\vec{\mathbf{H}}^i\cdot\hat{z}$, J_m, and H_m are the m-th order Bessel and Hankel function of the first kind, respectively, and the $'$ indicates the derivative with respect to the entire argument. Other terms, such as A_m, and B_m are given in [18, 35]. Using these currents, the electric field can be written in terms of electric ($\vec{\Pi}_e$), and magnetic ($\vec{\Pi}_m$) Hertz potentials using

$$\vec{\mathbf{E}}(\vec{r}) = \nabla\times\nabla\times\vec{\Pi}_e(\vec{r})+jk_0Z_0\nabla\times\vec{\Pi}_m(\vec{r}) \qquad (4.3)$$

where

$$\vec{\Pi}_e = \frac{jZ_0}{4\pi k_0}\int_0^{2\pi}\vec{J}_e(\phi')\int_0^L \frac{e^{jk_0(|\vec{r}-\vec{r'}|-\cos\beta z')}}{|\vec{r}-\vec{r'}|}a dz' d\phi' \tag{4.4}$$

$$\vec{\Pi}_m = \frac{jY_0}{4\pi k_0}\int_0^{2\pi}\vec{J}_m(\phi')\int_0^L \frac{e^{jk_0(|\vec{r}-\vec{r'}|-\cos\beta z')}}{|\vec{r}-\vec{r'}|}a dz' d\phi' \tag{4.5}$$

In situations where the observation point is not in the far-field region of the cylinder, a difficulty arises from the evaluation of $\int_0^L \frac{e^{jk_0(|\vec{r}-\vec{r'}|-\cos\beta z')}}{|\vec{r}-\vec{r'}|}dz'$. As will be shown, using an integral transformation, this integral can be represented by an approximate closed-form formula which retains a high degree of accuracy. Using the identity, $\frac{e^{jk_0|\vec{r}-\vec{r'}|}}{|\vec{r}-\vec{r'}|} = \frac{j}{2}\int_{-\infty}^{\infty} H_0^{(1)}(k_1\zeta)e^{j\alpha_1(z-z')}d\alpha_1$ [24], the integral is transformed to a more appropriate form:

$$\begin{aligned} I &= \int_0^L \frac{e^{jk_0(|\vec{r}-\vec{r'}|-\cos\beta z')}}{|\vec{r}-\vec{r'}|}dz' \\ &= \frac{j}{2}\int_0^L\int_{-\infty}^{\infty} H_0(k_1\zeta)e^{j\alpha_1(z-z')}d\alpha_1\cdot e^{-j\alpha z'}dz' \\ &= \frac{1}{2}\int_{-\infty}^{\infty}\frac{H_0(k_1\zeta)}{\alpha_1+\alpha}e^{j\alpha_1 z}d\alpha_1 - e^{-j\alpha L}\frac{1}{2}\int_{-\infty}^{\infty}\frac{H_0(k_1\zeta)}{\alpha_1+\alpha}e^{j\alpha_1(z-L)}d\alpha_1 \end{aligned}$$

where $\zeta = \sqrt{(x-x')^2+(y-y')^2}$, and $\alpha = k_0\cos\beta$, and $k_1^2 = k_0^2 - \alpha_1^2$. Each integral in the above equation can be transformed by following the standard steepest decent method procedure [24, 48] into

$$\begin{aligned} I_i &= \int_{-\infty}^{\infty}\frac{H_0(k_1\zeta)}{\alpha_1+\alpha}e^{j\alpha_1 z_i}d\alpha_1 \\ &\sim \sqrt{\frac{2}{\pi k_0\zeta}}e^{-j\pi/4}\cdot e^{jk_0 r_i}\int_{-\infty}^{\infty}\frac{\sqrt{\cos w}}{\sin w+\cos\beta}e^{-k_0 r_i s^2}\frac{dw}{ds}ds \end{aligned}$$

where i can be 1 or 2, $z_1 = z$, and $z_2 = z-L$. Also $\frac{dw}{ds} = \frac{2\sqrt{-j}}{\sqrt{1+\cos(w-\theta_s)}}$, $\cos\theta_s = \frac{\zeta}{r_i}$, $r_i = \sqrt{\zeta^2+z_i^2}$, and $\cos(w-\theta_s) = 1+js^2$. Since the resulting integrand has a singularity at $w = \beta-\pi/2$, the integrand must be decomposed into two parts: one that contains the

singularity and the other one which is regular, that is

$$G(s) = \frac{\sqrt{\cos w}}{\sin w + \cos\beta} \cdot \frac{2\sqrt{-j}}{\sqrt{1+\cos(w-\theta_s)}} = \frac{b}{s-s_1} + T(s)$$

where $s_1 = \pm\sqrt{j[1-\sin(\beta-\theta_s)]}$, and b is the residue of $G(s)$ at the singularity which is given by

$$\begin{aligned} b &= \lim_{s\to s_1}(s-s_1)G(s) = \frac{1}{\sqrt{\sin\beta}} \\ T(0) &= G(0) + \frac{b}{s_1} = e^{-j\pi/4}\left[\frac{\sqrt{2\cos\theta_s}}{\sqrt{\sin\theta_s+\cos\beta}} \pm \frac{1}{\sqrt{\sin\beta}\sqrt{1-\sin(\beta-\theta_s)}}\right] \end{aligned}$$

Here the + sign is used for $\theta_s < \beta - \pi/2$, the - sign is used for $\theta_s > \beta - \pi/2$, and $T(0) = \frac{e^{-j\pi/4}}{\sqrt{\sin\beta}}\left[\frac{\cos\beta}{2\sin\beta} - \sqrt{2\sin\beta}\right]$ for $\theta_s = \beta - \pi/2$. Noting that

$$\int_{-\infty}^{\infty} \frac{b}{s-s_1} e^{-k_0 r s^2} ds + \int_{-\infty}^{\infty} T(s) e^{-k_0 r s^2} ds = j\pi b e^{-k_0 r s_1^2}\left[erf(j\sqrt{k_0 r}s_1) + \Lambda\right] + T(0)\sqrt{\frac{\pi}{k_0 r}}$$

where

$$\Lambda = \begin{cases} 1 & \mathrm{Im}[s_1] > 0 \\ 0 & \mathrm{Im}[s_1] = 0 \\ -1 & \mathrm{Im}[s_1] < 0 \end{cases}$$

the final expressions for I_1 and I_2 can be written as

$$I_i \sim e^{-j\pi/4}\left[\frac{e^{jk_0 r_i}}{k_0}\sqrt{\frac{2}{\zeta r_i}}T(0) + j\sqrt{\frac{2\pi}{k_0\sin\beta\zeta}}e^{jk_0 r_i \sin(\beta-\theta_s)} \cdot [erf(j\sqrt{k_0 r_i}s_1) + \Lambda]\right]$$

where $erf(\cdot)$ is the error function [24, 48, 31]. Noting that for large $k_0\sin\beta\zeta$ the quantity $\sqrt{\frac{2\pi}{k_0\sin\beta\zeta}}e^{jk_0 r_i\sin(\beta-\theta_s)} \sim \pi H_0(k_0\sin\beta\zeta)e^{-jk_0\cos\beta z_i}$, a better approximation for I_i may be

written as

$$I_i \sim \frac{e^{jk_0 r_i}}{k_0}\sqrt{\frac{2}{\zeta r_i}}T(0)e^{-j\pi/4} + j\pi H_0(k_0 \sin\beta\zeta)[erf(j\sqrt{k_0 r}s_1) + \Lambda]e^{-jk_0\cos\beta z_i} \qquad (4.6)$$

Hence the expression for the electric Hertz potential in (4.4), can be written as,

$$\begin{aligned}\vec{\Pi}_e \;\sim\; & \frac{jZ_0 a}{8\pi k_0}\sum_{m=-\infty}^{\infty}(-j)^m \int_0^{2\pi} e^{jm\phi'}\left[Q_{1m}Y_0(\sin\phi'\hat{x} - \cos\phi'\hat{y}) + Q_{2m}\hat{z}\right] \qquad (4.7)\\ & \cdot\; [I_1 - I_2 e^{-jk_0\cos\beta L}]d\phi'\end{aligned}$$

It is not obvious how to carry out the above integral with the respect to ϕ' analytically, however if $r^2 + a^2 >> a\rho$ is assumed, an analytical expression can be obtained using the following approximations,

$$\begin{aligned} r_1 &= \sqrt{(x-x')^2 + (y-y')^2 + z^2} \approx \sqrt{r^2 + a^2} - \frac{\rho a\cos(\phi - \phi')}{\sqrt{r^2 + a^2}},\\ \sqrt{r_1}s_1 &\approx \sqrt{r_{a1}}s_1 \end{aligned}$$

where $r = \sqrt{x^2 + y^2 + z^2}$, and $\rho = \sqrt{x^2 + y^2}$. Similarly,

$$\begin{aligned} r_2 &= \sqrt{(x-x')^2 + (y-y')^2 + (z-L)^2} \approx \sqrt{r_L^2 + a^2} - \frac{\rho a\cos(\phi - \phi')}{\sqrt{r_L^2 + a^2}},\\ \sqrt{r_2}s_1 &\approx \sqrt{r_{a2}}s_1 \end{aligned}$$

where $r_L = \sqrt{x^2+y^2+(z-L)^2}$. Therefore, with the aid of the integral relations given in [18, 35], the two integrals in (4.7) can be evaluated analytically as

$$\begin{aligned}
\vec{\pi}_e^i &= \frac{jZ_0 a}{4\pi k_0}\sum_{m=-\infty}^{\infty}(-j)^m\int_0^{2\pi}e^{jm\phi'}\left[Q_{1m}Y_0(\sin\phi'\hat{x}-\cos\phi'\hat{y})+Q_{2m}\hat{z}\right]I_i d\phi' \qquad (4.8)\\
&\sim \frac{jZ_0 a}{2k_0}\left[e^{-j\pi/4}\frac{e^{jk_0 r_{ai}}}{k_0}\sqrt{\frac{2}{\rho r_{ai}}}T(0)\sum_{m=-\infty}^{\infty}(-1)^m\vec{C}_m(\frac{\rho a}{r_{ai}})e^{jm\phi}\right.\\
&+ \left. j\pi H_0(k_0\sin\beta\rho_a)[erf(j\sqrt{k_0 r_{ai}}s_1)+\Lambda]e^{-jk_0\cos\beta z}\cdot\sum_{m=-\infty}^{\infty}(-1)^m\vec{C}_m(\frac{\rho a}{r_{ai}}\sin\beta)e^{jm\phi}\right]
\end{aligned}$$

where

$$\begin{aligned}
r_{a1} &= \sqrt{r^2+a^2}, \qquad r_{a2}=\sqrt{r_L^2+a^2}\\
\vec{C}_m(y_0) &= Y_0 Q_{1m}P_{1m}(y_0)\hat{x}-Y_0Q_{1m}P_{2m}(y_0)\hat{y}+Q_{2m}J_m(y_0)\hat{z}\\
P_{1m}(y_0) &= j\sin\phi J_m'(y_0)-\cos\phi\frac{m}{y_0}J_m(y_0)\\
P_{2m}(y_0) &= -j\cos\phi J_m'(y_0)+\sin\phi\frac{m}{y_0}J_m(y_0)
\end{aligned}$$

Similarly,

$$\begin{aligned}
\vec{\pi}_m^i &\sim \frac{jY_0 a}{2k_0}\left[e^{-j\pi/4}\frac{e^{jk_0 r_{ai}}}{k_0}\sqrt{\frac{2}{\rho r_{ai}}}T(0)\sum_{m=-\infty}^{\infty}(-1)^m\vec{D}_m(\frac{\rho a}{r_{ai}})e^{jm\phi}\right. \qquad (4.9)\\
&+ \left. j\pi H_0(k_0\sin\beta\rho_a)[erf(j\sqrt{k_0 r_{ai}}s_1)+\Lambda]e^{-jk_0\cos\beta z}\cdot\sum_{m=-\infty}^{\infty}(-1)^m\vec{D}_m(\frac{\rho a}{r_{ai}}\sin\beta)e^{jm\phi}\right]
\end{aligned}$$

where $\vec{D}_m(y_0) = -\bar{Q}_{1m}P_{1m}(y_0)\hat{x}+\bar{Q}_{1m}P_{2m}(y_0)\hat{y}+\bar{Q}_{2m}J_m(y_0)\hat{z}$. Finally the two Hertz vectors can be expressed by

$$\begin{aligned}
\vec{\Pi}_e &\sim \frac{1}{2}\left(\vec{\pi}_e^1-\vec{\pi}_e^2 e^{-jk_0\cos\beta L}\right),\\
\vec{\Pi}_m &\sim \frac{1}{2}\left(\vec{\pi}_m^1-\vec{\pi}_m^2 e^{-jk_0\cos\beta L}\right)
\end{aligned}$$

According to (4.3), the scattered electric field can be evaluated by taking the curl of the approximate closed form expressions of the Hertz potentials. Noting that the observation point is in the far-field with regard to cylinder diameter ($\rho > \frac{8a^2}{\lambda}$), the far-field approximation for the ∇ operator is expressed as

$$\begin{aligned} \nabla e^{jk_0 r_{a1}} &= jk_0 \frac{\vec{r}_{a1}}{r_{a1}} e^{jk_0 r_{a1}}, \quad \nabla e^{jk_0 r_{a2}} = jk_0 \frac{\vec{r}_{a2}}{r_{a2}} e^{jk_0 r_{a2}} \\ \nabla e^{jk_0(\sin\beta\rho_a - \cos\beta z)} &= jk_0 \hat{k}_s e^{jk_0(\sin\beta\rho_a - \cos\beta z)} \end{aligned}$$

where $\hat{k}_s = \sin\beta\cos\phi\hat{x} + \sin\beta\sin\phi\hat{y} - \cos\beta\hat{z}$. After some algebraic manipulation, the complete expression of the electric field for a finite cylinder may be written as

$$\begin{aligned} \vec{E} \sim -j\frac{k_0 a}{4} \Bigg[& e^{-j\pi/4} \frac{e^{jk_0 r_{a1}}}{k_0} \sqrt{\frac{2}{\rho r_{a1}}} T(0) \sum_{m=-\infty}^{\infty} (-1)^m e^{jm\phi} [Z_0 \hat{r}_{a1} \times \hat{r}_{a1} \times \vec{C}_m(\frac{\rho a}{r_{a1}}) + \\ & \hat{r}_{a1} \times \vec{D}_m(\frac{\rho a}{r_{a1}})] - e^{-jk_0 \cos\beta L} e^{-j\pi/4} \frac{e^{jk_0 r_{a2}}}{k_0} \sqrt{\frac{2}{\rho r_{a2}}} T(0) \cdot \\ & \sum_{m=-\infty}^{\infty} (-1)^m e^{jm\phi} [Z_0 \hat{r}_{a2} \times \hat{r}_{a2} \times \vec{C}_m(\frac{\rho a}{r_{a2}}) + \hat{r}_{a2} \times \vec{D}_m(\frac{\rho a}{r_{a2}})] + \\ & j\pi H_0(k_0 \sin\beta\rho_a) e^{-jk_0 \cos\beta z} \sum_{m=-\infty}^{\infty} (-1)^m e^{jm\phi} [Z_0 \hat{k}_s \times \hat{k}_s \times \vec{C}_m(\frac{\rho a}{\rho_a} \sin\beta) + \\ & \hat{k}_s \times \vec{D}_m(\frac{\rho a}{\rho_a} \sin\beta)] \left[erf(j\sqrt{k_0 r_{a1}} s_1) + \Lambda_1 - erf(j\sqrt{k_0 r_{a2}} s_1) - \Lambda_2 \right] \Bigg] \end{aligned} \tag{4.10}$$

Equation (4.10) is valid for observation points on or near the forward scattering cone. If the observation point is outside the cone (the effect of the pole can be neglected), another equation for the scattered field can be formulated. Using the asymptotic behavior of the error function, $erf(z) \sim 1 - \frac{e^{-z^2}}{\sqrt{\pi}z}$ [31], (4.6) can be reduced to

$$I_i \sim -j\frac{e^{jk_0 r_i}}{r_i} \frac{2}{k_0(\sin\theta_s + \cos\beta)}$$

Through the same procedure and approximations, a formulation for the scattered field that

is valid outside the forward scattering cone can be written as

$$\vec{\mathbf{E}} \sim -\frac{a}{2}\left[\frac{e^{jk_0 r_{a1}}}{r_{a1}}\frac{1}{\sin\theta_s+\cos\beta}\sum_{m=-\infty}^{\infty}(-1)^m e^{jm\phi}[Z_0\hat{r}_{a1}\times\hat{r}_{a1}\times\vec{C}_m(\frac{\rho a}{r_{a1}})+\right.$$
$$\hat{r}_{a1}\times\vec{D}_m(\frac{\rho a}{r_{a1}})]-\frac{e^{jk_0 r_{a2}}}{r_{a2}}\frac{e^{-jk_0\cos\beta L}}{\sin\theta_s+\cos\beta}\cdot \tag{4.11}$$
$$\left.\sum_{m=-\infty}^{\infty}(-1)^m e^{jm\phi}[Z_0\hat{r}_{a2}\times\hat{r}_{a2}\times\vec{C}_m(\frac{\rho a}{r_{a2}})+\hat{r}_{a2}\times\vec{D}_m(\frac{\rho a}{r_{a2}})\right]$$

It is worth mentioning that (4.10), and (4.11) can be reduced to the formula derived in [35] for observation points in the near-field region and a formula given in [18] for observation points in the far-field region. To apply this formulation to a cylinder with arbitrary orientation, it is needed to transform the components of the incident wave in the global coordinate system (X,Y,Z), to the local cylinder coordinate system (x',y',z') where z'-axis is parallel to the cylinder axis. After calculating the scattered field components in the local coordinates, they are transformed back to the global coordinate system. This procedure is mathematically expressed by

$$\vec{\mathbf{E}}_L^i = U^{-1}\vec{\mathbf{E}}_G^i$$
$$\vec{\mathbf{E}}_G^s = U\vec{\mathbf{E}}_L^s$$

where U is the transformation matrix and is given by

$$U=\begin{pmatrix}\cos\theta_c\cos\phi_c & -\sin\phi_c & \sin\theta_c\cos\phi_c\\ \cos\theta_c\sin\phi_c & \cos\phi_c & \sin\theta_c\sin\phi_c\\ -\sin\theta_c & 0 & \cos\theta_c\end{pmatrix}$$

for a cylinder with orientation angles (θ_c,ϕ_c), as is seen in Fig. 4.2.

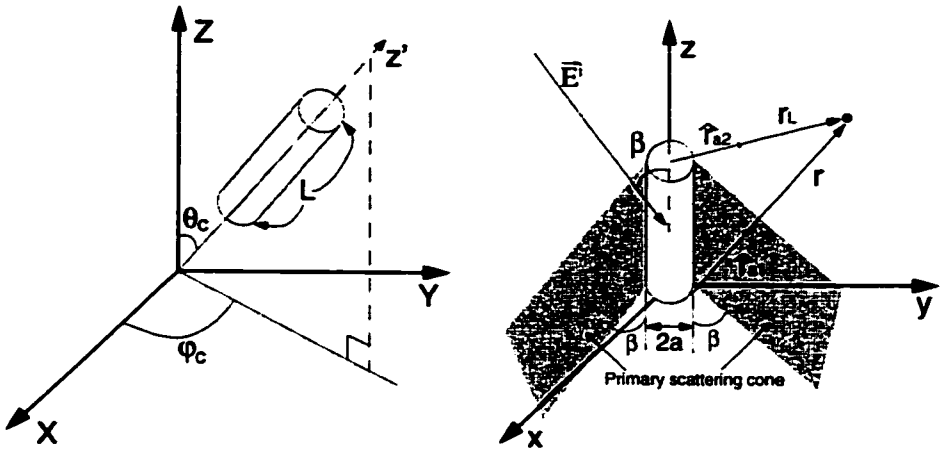

Figure 4.2: Global and local coordinate systems for an arbitrarily oriented cylinder (a) before the coordinate transformation (b) after the coordinate transformation.

4.2.2 Scattering from Leaves and Needles

The thickness of most broad leaf vegetation ($\tau \sim 0.1 - 0.5mm$) is very small compared to the wavelength at frequencies up to X-band. For these leaves the Rayleigh-Gans approximation [49] is used. This expression is supposed to be valid independent of the leaf surface dimensions relative to the wavelength. That is so long as the electric thickness of the leaf is very small, the Rayleigh-Gans approximation is expected to provide accurate results. However, we found that the accuracy of Rayleigh-Gans degrades for physical large leaves (see Appendix C). For leaves where surface dimensions are large compared to the wavelength and their electric thickness becomes compared to the wavelength, a physical optic approximation [18] is used. This solution is valid for frequencies at where $a > 0.5\lambda$. A formulation for thin cylinders of arbitrary cross section [18] is used to model the scattering from vegetation needles (see Appendix B).

Polarization currents in a thin dielectric disk, model for a leaf, and a thin dielectric

cylinder, model for a needle, can be expressed in terms of polarizability tensor ($\bar{\bar{\mathbf{P}}}$) like

$$\vec{\mathbf{J}} = -jk_0 Y_0(\varepsilon_r - 1)\bar{\bar{\mathbf{P}}} \cdot \vec{\mathbf{E}}^i$$

The tensor can be obtained analytically using Rayleigh-Gans approximation, and reduced to diagonal matrix which is written: For a leaf

$$P_{xx} = P_{yy} = 1, \quad P_{zz} = 1/\varepsilon_r$$

for a needle

$$P_{xx} = P_{yy} = \frac{2}{\varepsilon_r + 1}, \quad P_{zz} = 1$$

Using these currents, scattered field from a leaf or needle can be easily calculated (see Appendix B and C).

4.2.3 Effect of Ground Plane

To calculate the scattered field accurately, the effect of the ground plane should be included into the final solution. The underlying soil surface is modeled by a half-space dielectric medium. However, to account for the exact effect of the half-space dielectric using the Sommerfeld integral is very complicated and not necessary for the required degree of accuracy. Thus in this work, only the three dominant G.O. components are incorporated into the final solution. The first component is the scattered field generated by the reflected incident field from the ground plane, denoted by $\vec{\mathbf{E}}^{gr}$, the second term is the scattered field reflected from the ground plane ($\vec{\mathbf{E}}^{rg}$), and the third component is the scattered field generated by reflected incident field which is again reflected from the ground ($\vec{\mathbf{E}}^{grg}$) (see Fig. 4.3). These terms should be added coherently to the direct scattered field. The direction of the reflected incident wave is $\hat{k}_r = \hat{k}_i - 2(\hat{k}_i \cdot \hat{z})\hat{z}$ which makes an angle $\beta_r = \cos^{-1}(\hat{k}_r \cdot \hat{z}')$

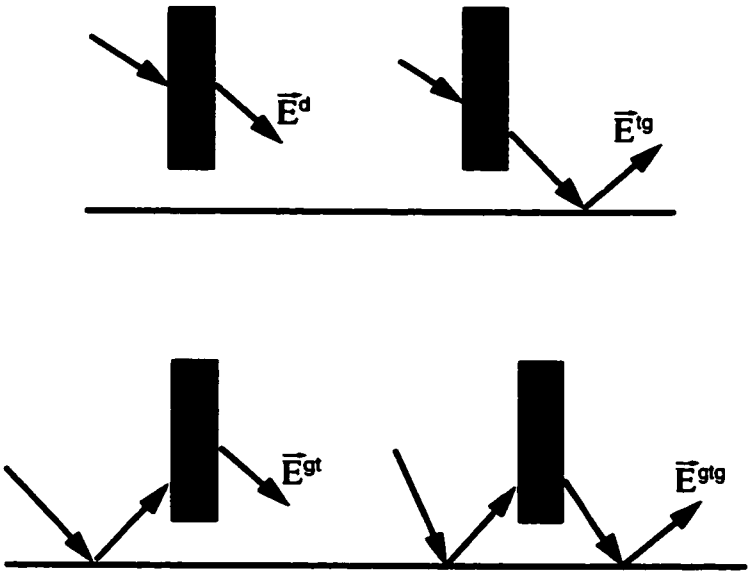

Figure 4.3: Three G.O. components of the scattered field from a cylinder above the ground plane, along with forward scattered component.

with the cylinder axis. The reflected field ($\vec{\mathbf{E}}^r$) consists of the parallel and perpendicular components of the incident wave, and are modified by the Fresnel reflection coefficients ($R_{||}$ and $R_\perp$), respectively, i.e., $\vec{\mathbf{E}}^r = E_v^i R_{||} \hat{v}_r + E_h^i R_\perp \hat{h}_r$ where $\hat{v}_r$ is a unit vector in the plane of incidence, and perpendicular to $\hat{k}_r$ and $\hat{h}_r$ is perpendicular to the plane of incidence. The expansion shown in (4.10), and (4.11) can be used to find $\vec{\mathbf{E}}^{gt}$ using $\vec{\mathbf{E}}^r$ as the incident wave on the cylinder. To include other components, approximate image currents in the ground are used. From an asymptotic formulation of the electric, and magnetic Hertz potentials of an infinitesimal dipole above the ground [50], approximate image currents can be inferred as

$$\begin{aligned}
\vec{\mathbf{J}}_e^i &= R_\perp a_x^e \hat{X} + R_\perp a_y^e \hat{Y} + (R_{||} a_z^e + \cos\phi R_1 a_x^e + \sin\phi R_1 a_y^e)\hat{Z} \\
\vec{\mathbf{J}}_m^i &= R_{||} a_x^m \hat{X} + R_{||} a_y^m \hat{Y} + (R_\perp a_z^m + \cos\phi R_1 a_x^m + \sin\phi R_1 a_y^m)\hat{Z}
\end{aligned}$$

where the currents above the ground plane are given as $\vec{\mathbf{J}}_e = a_x^e \hat{X} + a_y^e \hat{Y} + a_z^e \hat{Z}$, and $\vec{\mathbf{J}}_m = a_x^m \hat{X} + a_y^m \hat{Y} + a_z^m \hat{Z}$. Here $R_1 = 2\sin\theta\cos\theta \frac{\cos\theta - \sqrt{\varepsilon_d - \sin^2\theta}}{\varepsilon_d \cos\theta + \sqrt{\varepsilon_d - \sin^2\theta}}$, and ε_d is the dielectric constant

of the ground. The reflection coefficients, $R_\perp$, $R_\parallel$, and R_1 and other quantities such as $\sin\phi$, and $\cos\phi$ can be assumed constant because in the far-field region, the variation of these quantities is very small. The angle at which these Fresnel reflection coefficients are calculated is obtained by using the line connecting the image point to the observation point, that is, if $\vec{r}_0$ denotes the observation point and $\vec{r}_s^{\,i}$ represents the image of the source point this angle is defined as $\theta = \cos^{-1}\left(\hat{z}\cdot\frac{\vec{r}_0-\vec{r}_s^{\,i}}{|\vec{r}_0-\vec{r}_s^{\,i}|}\right)$. To compute $\vec{\mathbf{E}}^{tg}$, and $\vec{\mathbf{E}}^{gtg}$, equations (4.10), and (4.11) can now be used but the terms, $\vec{C}_m$, and $\vec{D}_m$ must be modified as

$$\begin{aligned}
\vec{C}_m &= Y_0 Q_{1m} R_\perp (P_{1m}\hat{x} - P_{2m}\hat{y}) + [Q_{1m} J_m R_\parallel + (\cos\phi P_{1m} - \sin\phi P_{2m}) Y_0 Q_{1m} R_1]\hat{z} \\
\vec{D}_m &= \bar{Q}_{1m} R_\parallel (P_{2m}\hat{y} - P_{1m}\hat{x}) + [\bar{Q}_{2m} J_m R_\perp + (\sin\phi P_{2m} - \cos\phi P_{1m}) \bar{Q}_{1m} R_1]\hat{z}
\end{aligned}$$

where $J_m = J_m(y_0)$.

4.3 Numerical Simulation

In this section the validity of the approximate formulations for the scattered field of a finite cylinder are being examined. A number of approximations were used to derive the integral expression given by (4.6). Figure 4.4 shows the comparison between the two results from an exact numerical integration and the analytic formulation, (4.6). In this comparison, L is 4λ and the observation point is at z = L/3 and $0.1 < \rho < 100$. As can be seen the two results are in excellent agreement over the entire region of comparison. The next three figures, 4.5, 4.6, and 4.7 show the accuracy of equation (4.10) when a TM, and TE waves are incident on a 4λ long cylinder with dielectric constant, $5 + j$, and a radius, $a = 5$cm, at $\beta = 60°$, and $\phi_i = 180°$. A MoM solution in Appendix A is used for exact calculation of the scattered field. It is shown that the two results are in good agreement. The accuracy of the approximate formulation (4.10) degrades as the ratio (radius/length) is increased.

The developed forest channel model is used to demonstrate performance assessment

of GPS receivers placed under coniferous and deciduous canopies. For these simulations the frequency is set at 1.57542GHz and the polarization is chosen to be right hand circular (RHCP). For the following simulations a receiver is placed 1m above a ground plane having a soil moisture content $m_v = 0.18$ which consists of 50% sand and 10% clay. At this GPS frequency the soil dielectric constant is calculated to be $\varepsilon_s = 9.75 + j1.62$ [43]. To derive the field statistics and forest channel properties, a Monte Carlo simulation is carried out using 400 realizations. To account for near-field effects 10 trees randomly located around the receiver are included in the simulations. First a relatively young red pine stand with average tree height of 9.5m and the density of 0.1 trees/m^2 is considered. The mean and standard deviation of the total field (incident + reflected + scattered) are shown in Figs. 4.8, and 4.9, respectively for both h- and v-polarized incident waves as function of incidence angle. As the incidence angle increases, the field is more attenuated as expected, and small cross-polarized components are observed. In Fig. 4.8(a), the mean-field jumps approximately 10dB at incidence angle 50° due to the interference between the direct incident wave and the reflected wave from the ground. Note that E_z has more fluctuation than E_x, and E_y. This is due to the fact that most scattering fluctuations are caused by the tree trunks which are big and vertically alinged. Figures 4.10 shows the path-loss as a function of incidence angle. The path-loss is defined as the ratio of the total power received to that in the free-space. In this example a short dipole aligned to receive the incident wave is used as the receiver antenna. Next we examine the statistics of the polarization of the received signal. Polarization of a wave is characterized by two parameters, the ellipticity angle, χ, and the tilt angle, ξ [19]. At the receiver both the vertical and horizontal components of the electric field in a plane perpendicular to the direction of incidence are calculated, and for which χ and ξ are evaluated. In this simulation the polarization of incidence wave is assumed be right hand circular polarization. A Monte Carlo simulation is used to estimate the probability density function (pdf) of χ and ξ for the red pine stand. It is shown that as the incidence angle is increased the polarization of the received signal is modified, how-

ever, it remains always righthanded. A similar Monte Carlo simulation is carried out for deciduous forest stand that consist of red maples. A tree density of $0.1/m^2$ and average height of 17m and trunk diameter of 20cm is chosen. This stand has a dry biomass of 107 Kg/tree. Simulations for both foliated and defoliated trees are performed. Figures 4.12, and 4.13 show the mean-field and standard deviation for a receiver 1m above the ground for a foliated stand as a function of incidence angle. The same jump phenomenon is observed in the mean-field due to the same interference as the pine tree case. Similar to the pine forest simulation the standard deviation is comparable to or larger than the mean field, and the level of the cross polarized field is relatively low. The path loss is also calculated and shown in Fig. 4.14. As the incidence angle increases, the v-polarized wave is more attenuated because the path length increases in the trunk layer where scatterers are aligned mostly along $\hat{z}-$ axis. Whereas the number of leaves (of the order of 12000 per a typical tree) is higher than the number of branches and twigs ($\sim$ 7000), scattering from leaves can be ignored as their typical dimension (7cm) is small compared to the wavelength. However leaves can cause considerable attenuation. Figure 4.15 shows the pdf of ellipticity angle and tilt angle for a receiver 1m above ground under the red maple stand. It is shown that the incident wave approached a linear wave (h-polarized).

Next we examine the effect of receiver height on the field attenuation, fluctuation, and depolarization for the red pine stand at 40° incidence. Tables 4.1, and 4.2 show the three components of mean-field and its standard deviation for the two principal polarizations. It is shown that the ratio of standard deviation to mean-field decreases as the receiver height is increased. Table 4.3 shows the co-polarized path-loss as a function of receiver height. The pdfs of polarization state as a function of receiver height for incidence angle 40° are shown in Fig. 4.16. The polarization at z = 10m is almost the same as that of the incident wave (RHCP).

Now let's consider a GPS receiver at a height of 1m above ground embedded in the red pine . It is assumed that polarization of the antenna is RHCP and has a free space gain of

0dBi. The power received by such receiver in free space is -160dBW on the earth surface [42]. This signal level is below the thermal noise power at the receiver if it were not for the processing gain of about 30dB for the 1023 chip code length of the GPS receiver [38]. Considering the receiver bandwidth is B = 2.046MHz, the noise power is calculated from

$$N = KTB = KT_0(NF - 1)B \approx -134dBW$$

This calculation assumes a receiver noise figure of 1.5dB and the noise power associate with the antenna temperature is ignored. However, it should be pointed out that the antenna temperature operating under foliage can be significantly different (higher) than that without foliage. Figure 4.17(a) shows the mean power received by the GPS receiver under red pine forest. Also shown in this figure (the vertical bar) is a power range of the simulation and the received power in the absence of foliage, and the thermal noise power plus 10dB (threshold S/N). It is shown that the mean signal power is above the threshold for incidence angles below 70°, however, strong power fluctuations may hamper receiver signal lock on a given satellite. Figure 4.17(b) shows the performance of the same receiver below the red maple stand. Here receiver power fluctuation is less since the lower branches are farther from the receivers. In both cases reliable operation cannot be guaranteed. To remedy this problem more transmitter power (by a factor of 15dB) is needed.

Last we examine the performance of a wideband time domain communication system. Time-domain modulation using very narrow pulses is being considered for military applications, since it minimizes evesdropping and provides anti-jamming capability. A signal occupying a bandwidth 1 to 2GHz is considered. Again a receiver is considered to be 1m above the ground plane in the red pine stand. An incidence angle of 40° is assumed. Figure 4.18 shows the frequency response of three components (for a given realization of tree) for both vertical and horizontal incident wave. Strong spectral field fluctuations are a result of multipath caused by strong scatterers in the channel. The Fourier transform of these

responses provides the time domain response of the channel. Figure 4.19 shows the time domain response for the three received field components assuming the incident field has a Gaussian envelope for both the vertical and horizontal incident waves.

4.4 Conclusion

A physics-based channel estimation model for a forested environment is developed. This model is appropriate when either the transmitter or receiver is within the canopy and the other is outside. Realistic tree structures are constructed using a fractal algorithm and scattering from individual tree components are calculated and added coherently. An accurate approximate uniform near-field to far-field scattering solution for dielectric cylinders representing branches, and tree trunks is also developed, and incorporated into the tree model. Monte Carlo simulations are carried out in order to estimate the statistics of the channel behavior, such as path-loss, coherence bandwidth, field fluctuation, etc.. In specifics, performance of GPS receivers under foliage is evaluated and it is shown that the signal attenuation, depolarization, and field fluctuation hamper proper operation of a receiver under both coniferous, and deciduous stands with heights as low as 10m. The same model is used to assess the performance of wideband communications.

	h-pol. incident			v-pol. incident		
Height	E_x[dB]	E_y[dB]	E_z[dB]	E_x[dB]	E_y[dB]	E_z[dB]
10cm	-41.2	-9.0	-41.8	-12.4	-47.9	-13.3
1m	-46.9	-21.3	-48.4	-15.7	-40.8	-11.2
10m	-63.2	0.8	-49.7	-1.9	-46.0	-4.1

Table 4.1: Mean of total field under pine trees at three different heights, 0.1m, 1m, and 10m when a plane wave is incident at 40°.

	h-pol. incident			v-pol. incident		
Height	E_x[dB]	E_y[dB]	E_z[dB]	E_x[dB]	E_y[dB]	E_z[dB]
10cm	-14.1	-7.7	-17.6	-8.8	-13.1	-9.2
1m	-13.8	-7.3	-15.3	-9.2	-11.8	-8.8
10m	-22.7	-17.1	-22.6	-16.7	-20.6	-21.5

Table 4.2: Standard deviation of total field under pine trees at three different heights, 0.1m, 1m, and 10m when a plane wave is incident at 40°.

	Total power		Received power	
Height	h-pol.[dB]	v-pol.[dB]	h-pol.[dB]	v-pol.[dB]
10cm	-4.6	-3.9	-5.3	-5.2
1m	-5.8	-3.8	-7.1	-5.5
10m	0.9	0.3	0.9	0.1

Table 4.3: Total and received power under pine trees at three different heights, 0.1m, 1m, and 10m when a plane wave is incident at 40°.

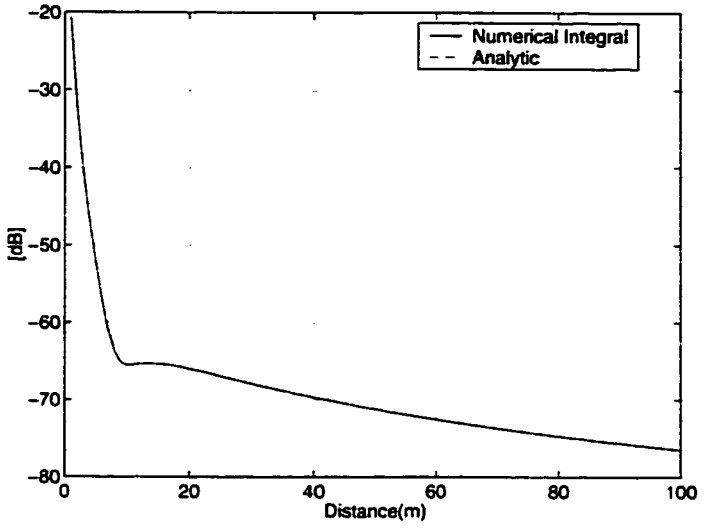

(a)

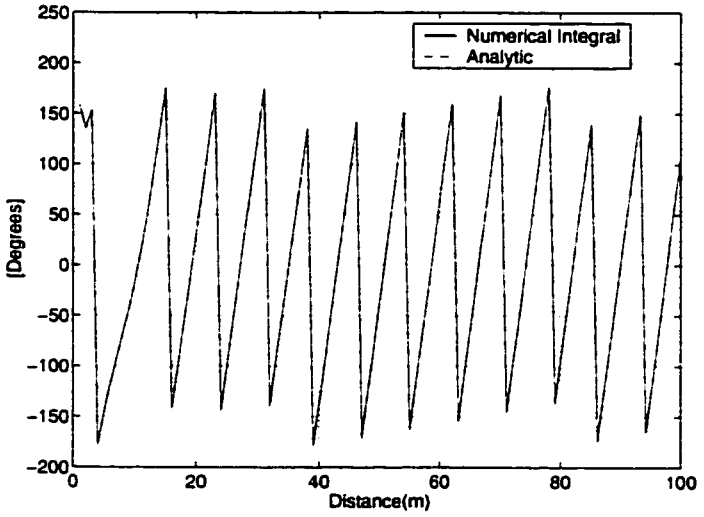

(b)

Figure 4.4: Numerical and analytic evaluation of $\int_0^L \frac{e^{jk_0(|\vec{r}-\vec{r'}|-\cos\beta z')}}{|\vec{r}-\vec{r'}|}dz'$ (a) Magnitude (b) Phase.

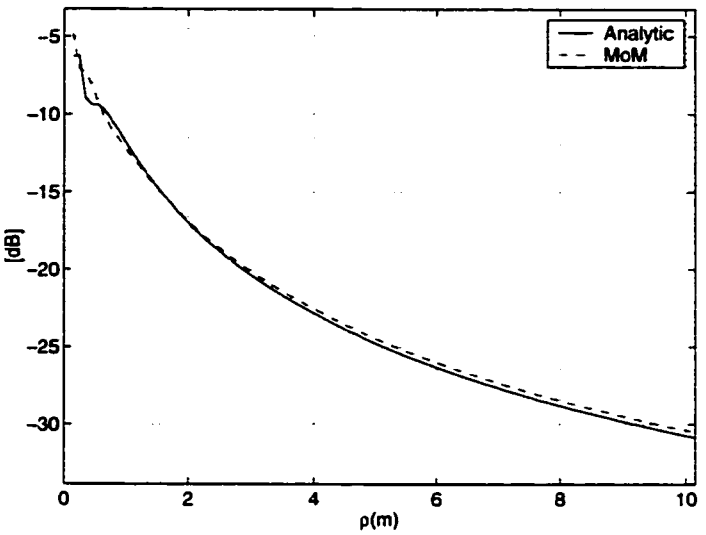

(a)

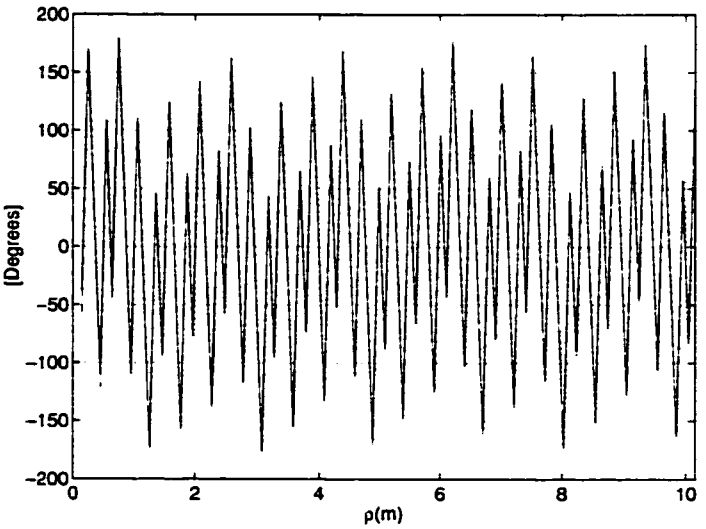

(b)

Figure 4.5: Comparison of analytic and MoM results of scattered field (E_x) from a finite cylinder whose radius is 5cm and dielectric constant is $5+j$. The length of the finite cylinder is 4λ, and the observation line is $z = L/2 - \rho/\tan\beta$. TM wave is incident at $\beta = 60^o$, and $\phi_i = 180^o$. (a) Magnitude (b) Phase.

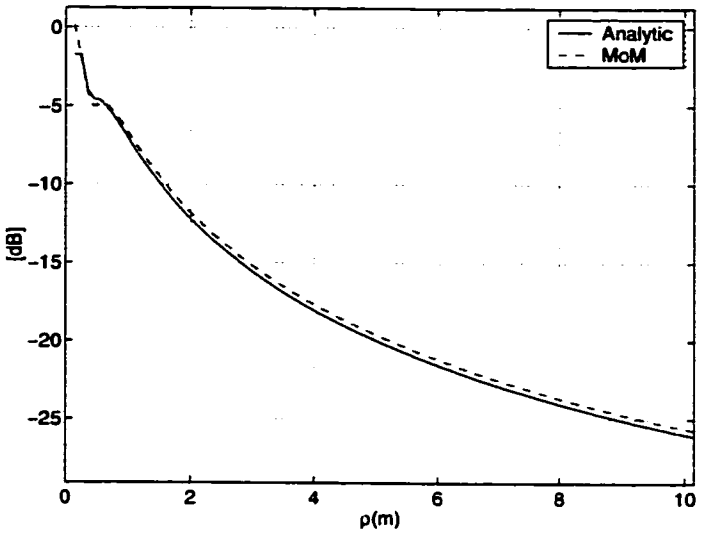

(a)

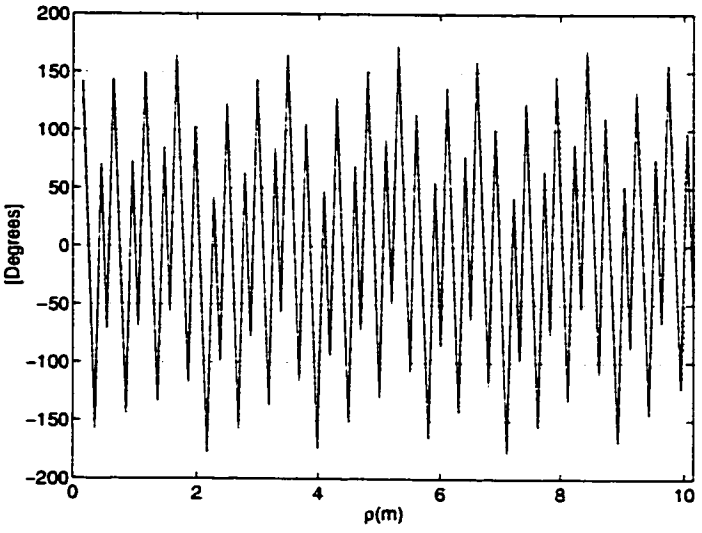

(b)

Figure 4.6: Comparison of analytic and MoM results of scattered field (E_z) from a finite cylinder whose radius is 5cm and dielectric constant is $5+j$. The length of the finite cylinder is 4λ, and the observation line is $z = L/2 - \rho/\tan\beta$. TM wave is incident at $\beta = 60^o$, and $\phi_i = 180^o$. (a) Magnitude (b) Phase.

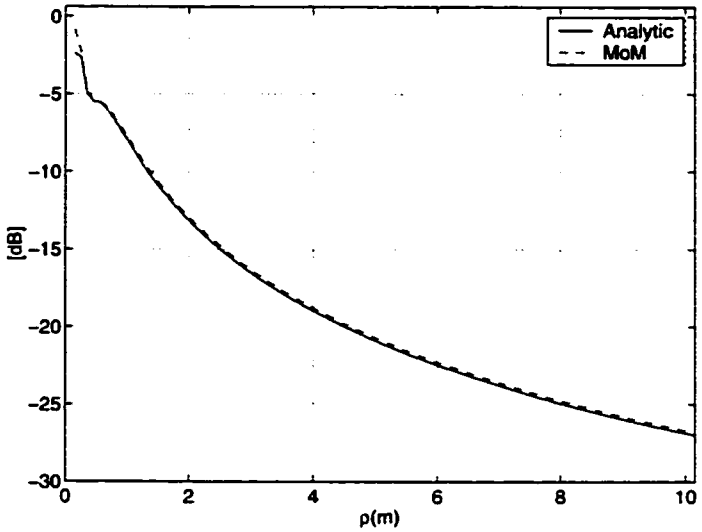

(a)

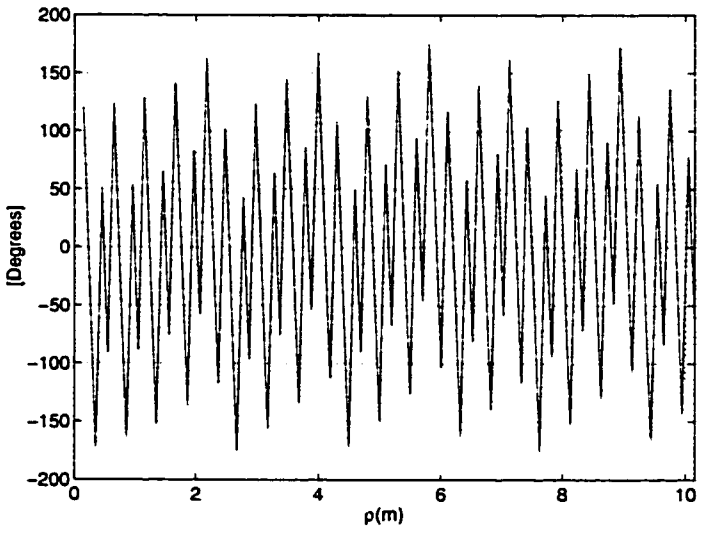

(b)

Figure 4.7: Comparison of analytic and MoM results of scattered field (E_y) from a finite cylinder whose radius is 5cm and dielectric constant is $5+j$. The length of the finite cylinder is 4λ, and the observation line is $z = L/2 - \rho/\tan\beta$. TE wave is incident at $\beta = 60^o$, and $\phi_i = 180^o$. (a) Magnitude (b) Phase.

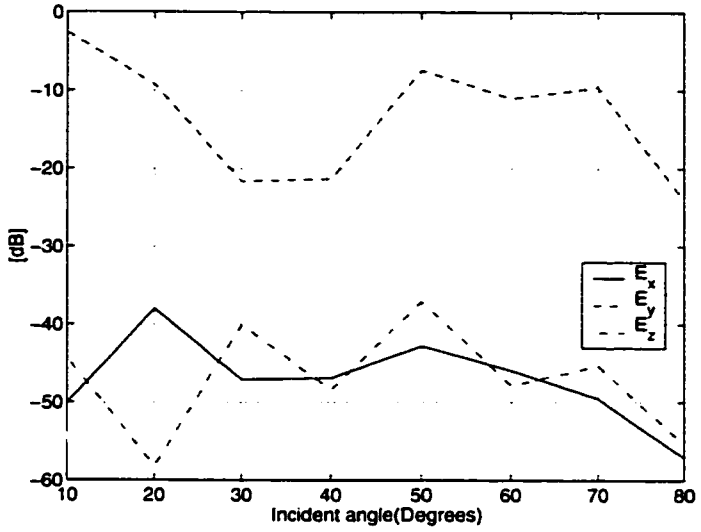

(a)

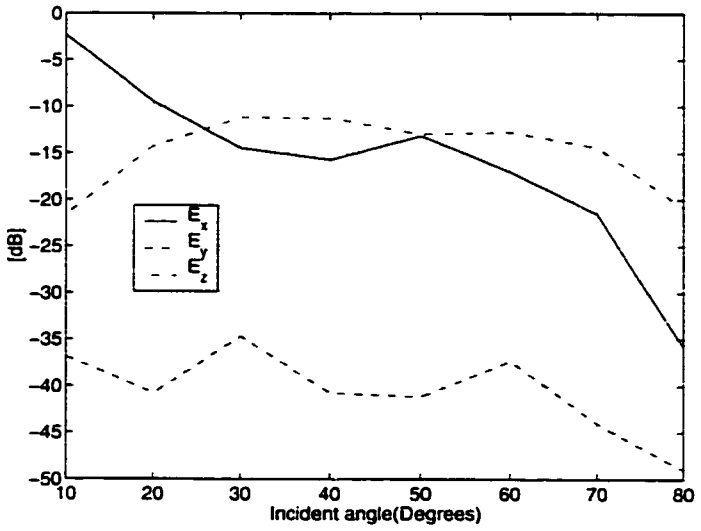

(b)

Figure 4.8: Mean of total field at z = 1m under pine trees as a function of incidence angle. The trees are located randomly with a density, $0.1/m^2$. (a) The incident wave is h-polarized. (b) The incident wave is v-polarized.

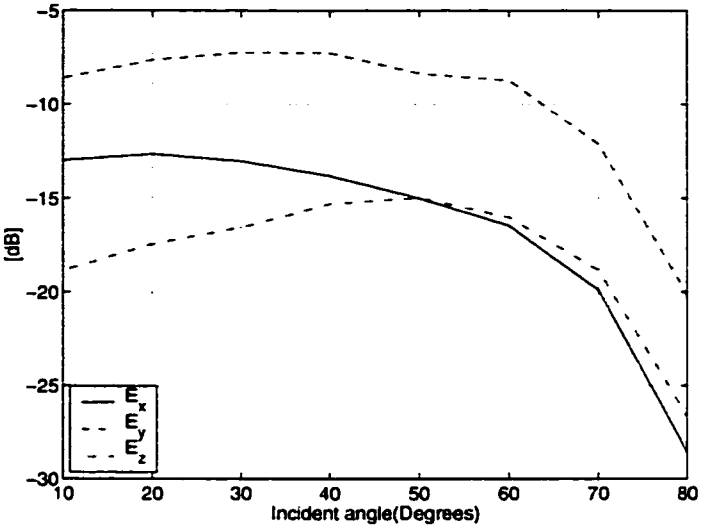

(a)

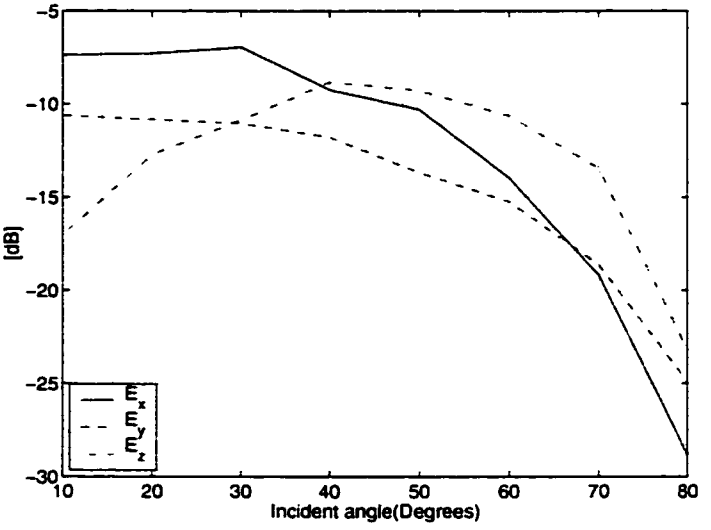

(b)

Figure 4.9: Standard deviation of total field at z = 1m under pine trees as a function of incidence angle. The trees are located randomly with a density, $0.1/m^2$. (a) The incident wave is h-polarized. (b) The incident wave is v-polarized.

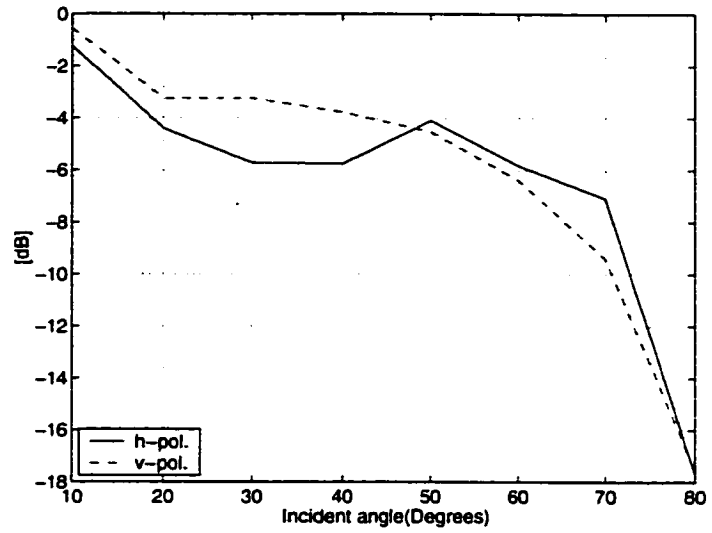

(a)

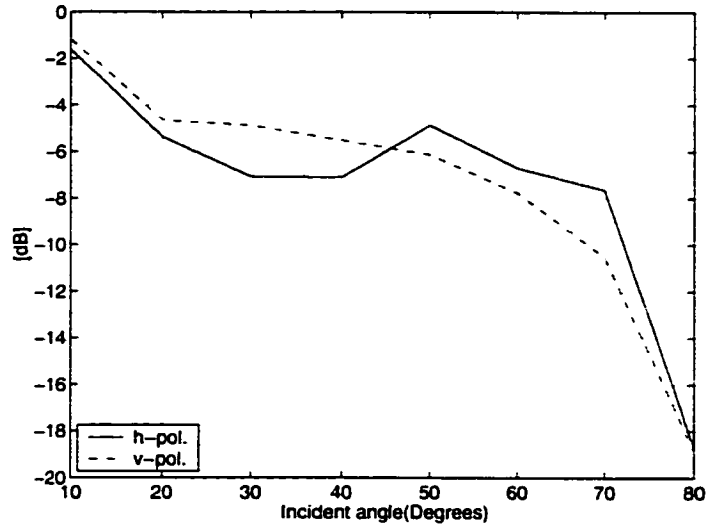

(b)

Figure 4.10: Total and received power at z = 1m under pine trees as a function of incidence angle. The trees are located randomly with a density, $0.1/m^2$. (a) $\langle |E|^2 \rangle$ (b) Path-loss.

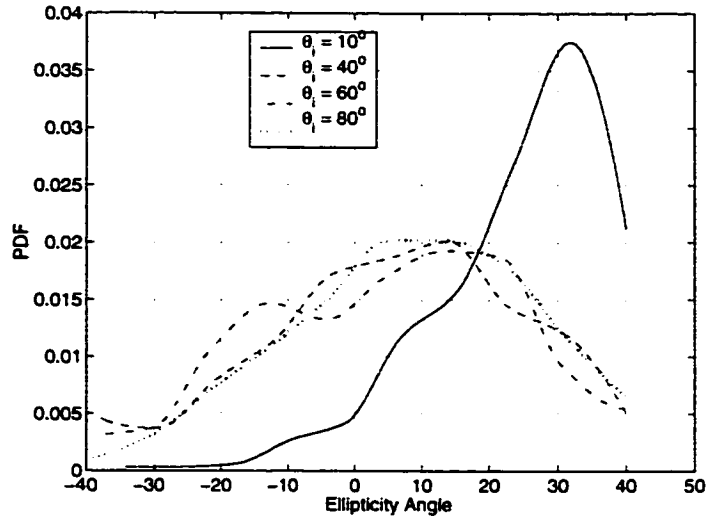

(a)

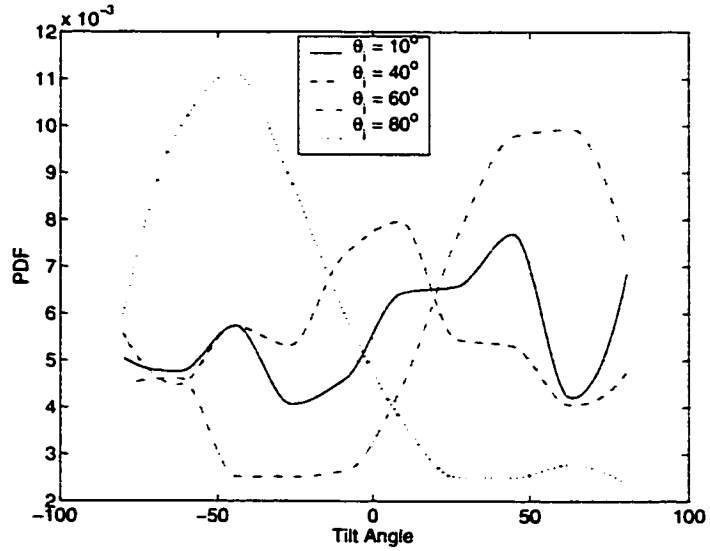

(b)

Figure 4.11: Probability density function (PDF) of polarization of the received signal at z = 1m under pine trees. Four results are plotted whose incidence angles are 10^o, 40^o, 60^o, and 80^o. (a) PDF of ellipticity angle (b) PDF of tilt angle.

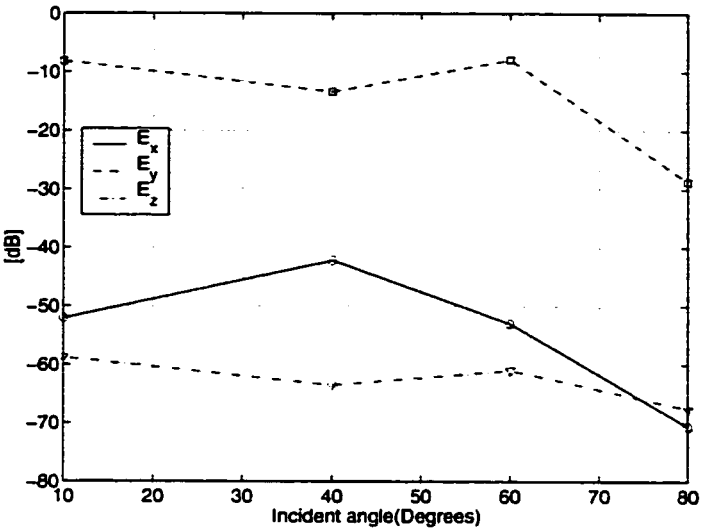

(a)

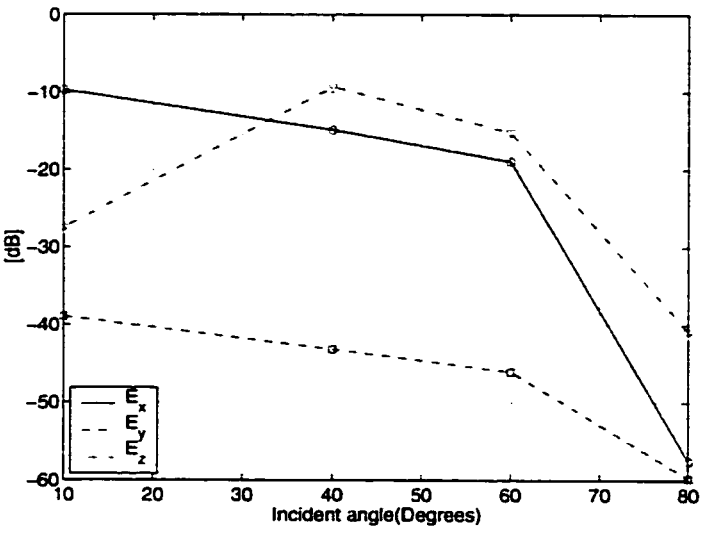

(b)

Figure 4.12: Mean of total field at z = 1m under deciduous trees as a function of incidence angle. The trees are located randomly with a density, $0.1/m^2$, and the results include the effects of leaves. (a) The incident wave is h-polarized. (b) The incident wave is v-polarized.

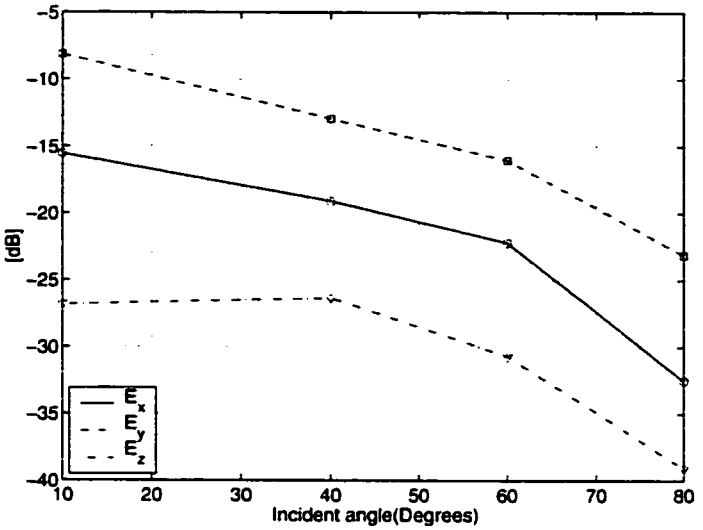

(a)

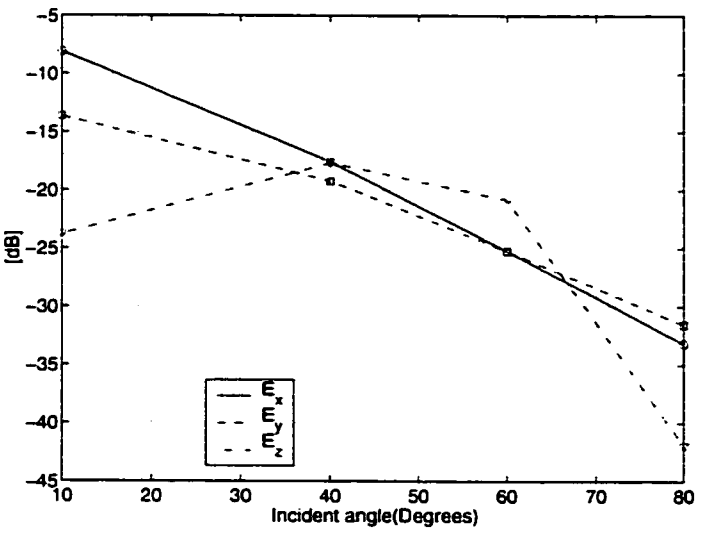

(b)

Figure 4.13: Standard deviation of total field at z = 1m under deciduous trees as a function of incidence angle. The trees are located randomly with a density, $0.1/m^2$, and the results include the effects of leaves. (a) The incident wave is h-polarized. (b) The incident wave is v-polarized.

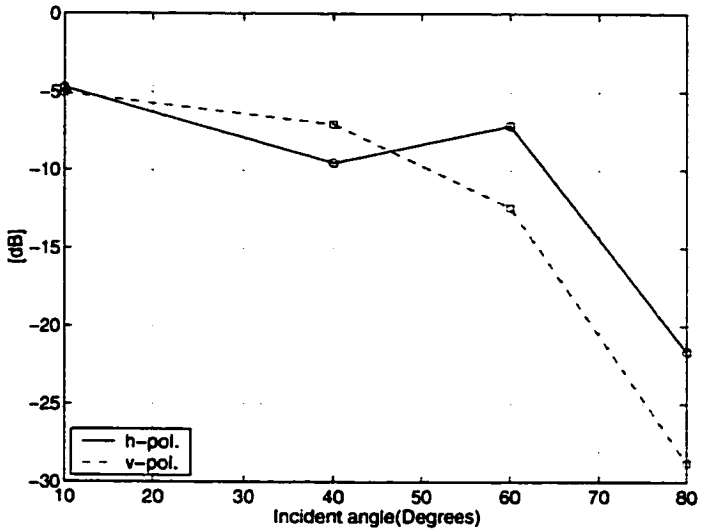

(a)

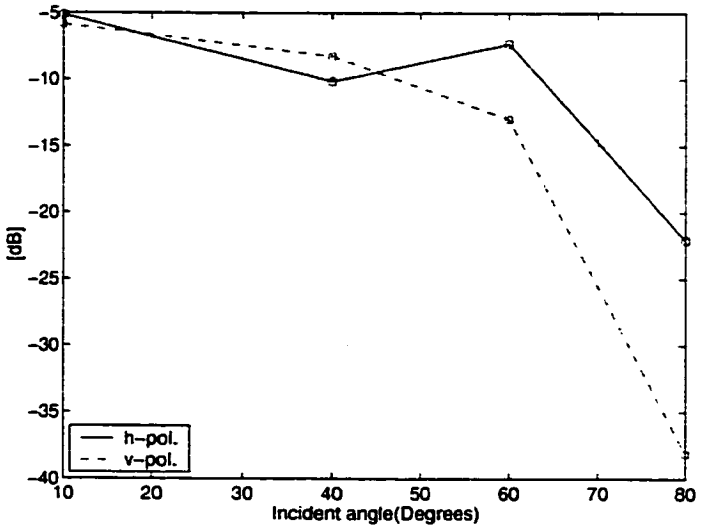

(b)

Figure 4.14: Total and received power at z = 1m under deciduous trees as a function of incidence angle. The trees are located randomly with a density, $0.1/m^2$. 'o', and '□' are results that include the effects of leaves. (a) $\langle |E|^2 \rangle$ (b) Path-loss.

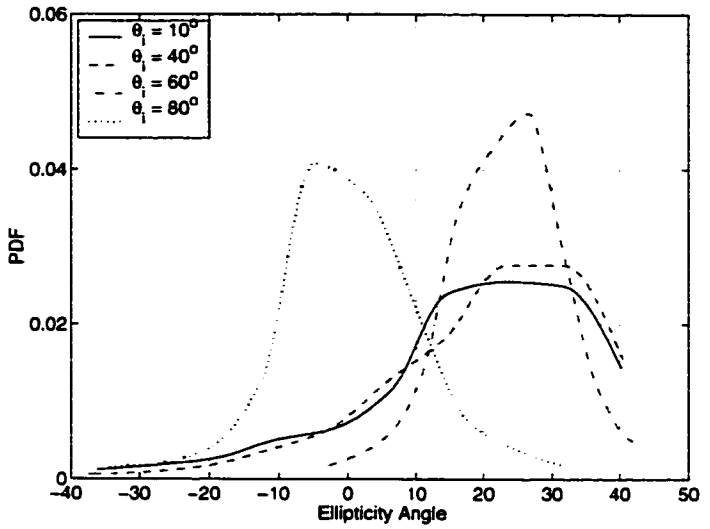

(a)

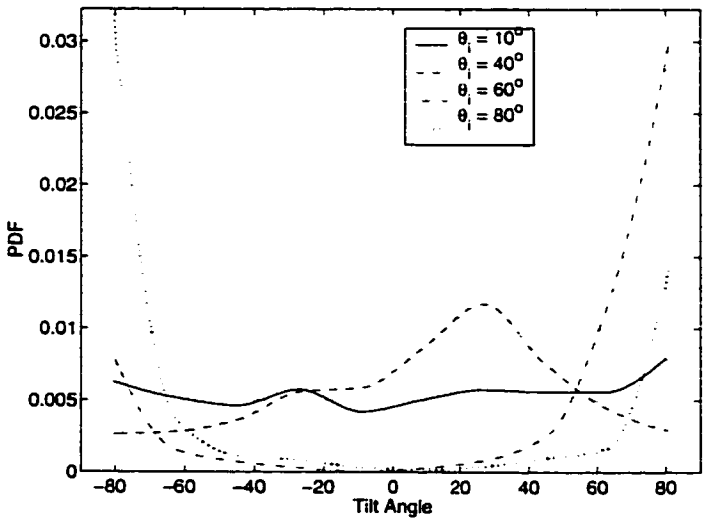

(b)

Figure 4.15: Probability density function (PDF) of polarization of the received signal at z = 1m under deciduous trees. Four results are plotted whose incidence angles are 10^o, 40^o, 60^o, and 80^o. (a) PDF of ellipticity angle (b) PDF of tilt angle.

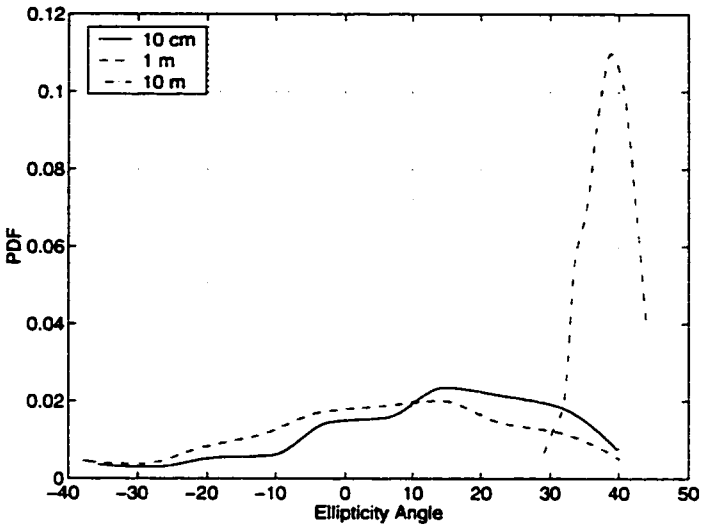

(a)

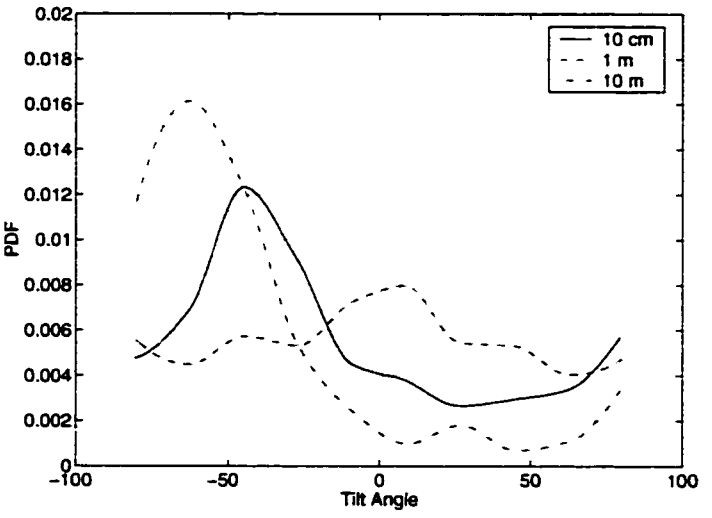

(b)

Figure 4.16: Probability density function (PDF) of polarization of the received signal at z = 1m under pine trees. Three results are plotted whose receiver heights are 0.1m, 1m, and 10m. (a) PDF of ellipticity angle (b) PDF of tilt angle.

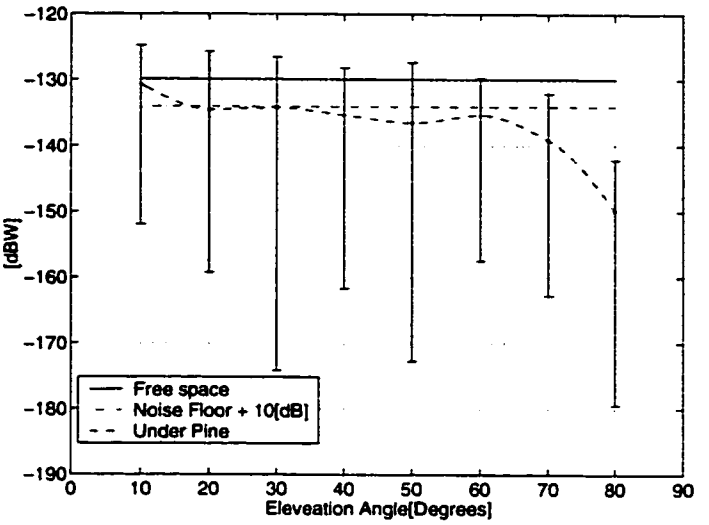

(a)

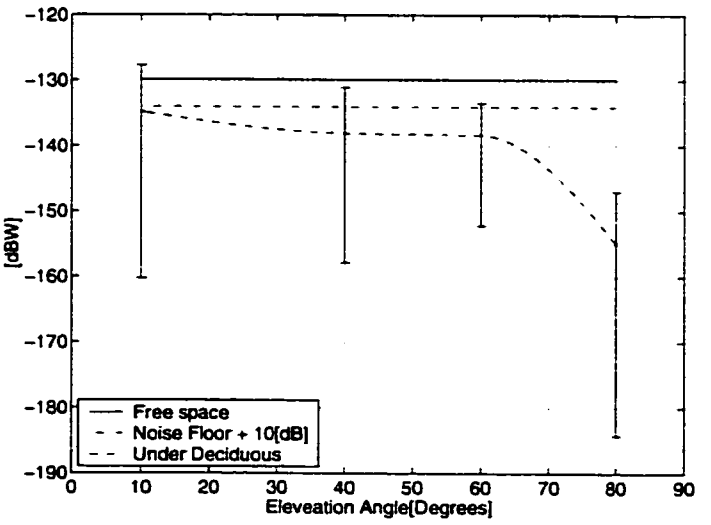

(b)

Figure 4.17: Plot of the received signal power under pine and deciduous forest with a density of $0.1/m^2$ and the received signal in free space. 'I' is the range of the received power. (a) Under pine trees (b) Under deciduous trees.

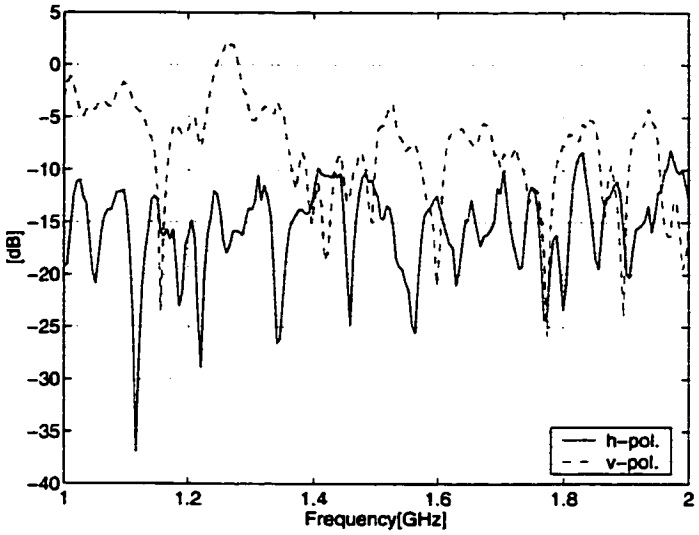
5
0
-5
-10
-15
-20
-25
-30
-35
-40
[dB]
1
1.2
1.4
1.6
1.8
2
Frequency[GHz]
h-pol.
v-pol.

(a)

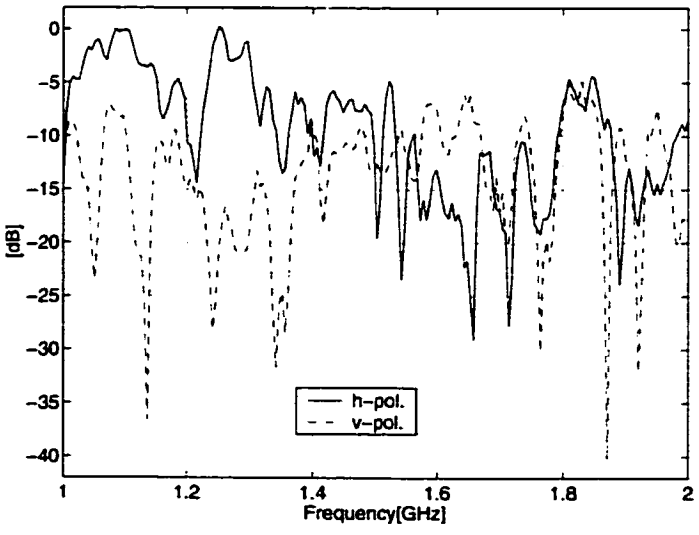
0
-5
-10
-15
-20
-25
-30
-35
-40
[dB]
1
1.2
1.4
1.6
1.8
2
Frequency[GHz]
h-pol.
v-pol.

(b)

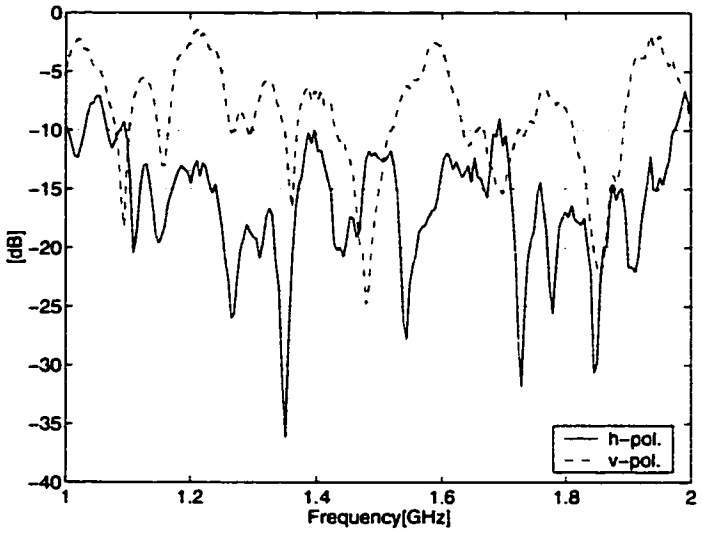

(c)

Figure 4.18: Frequency response of a pine forest over 1GHz bandwidth (1-2GHz) when a plane wave is incident at 40^o. The receiver is 1m over the ground plane. Effect of 20 trees near a receiver is considered. (a) E_x. (b) E_y. (c) E_z.

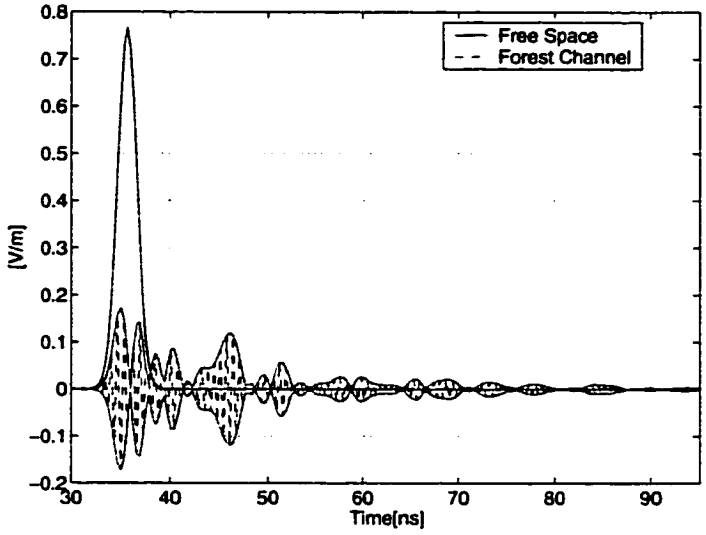
Free Space
Forest Channel
[V/m]
Time[ns]
0.8
0.7
0.6
0.5
0.4
0.3
0.2
0.1
0
−0.1
−0.2
30
40
50
60
70
80
90

(a)

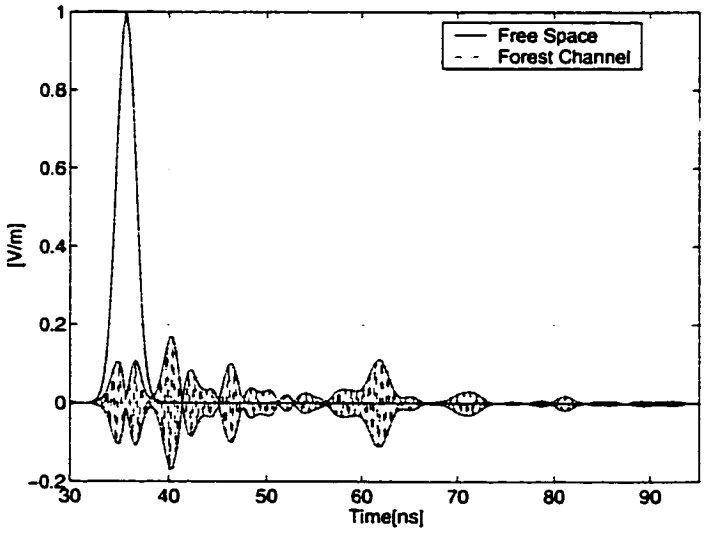
Free Space
Forest Channel
[V/m]
Time[ns]
1
0.8
0.6
0.4
0.2
0
−0.2
30
40
50
60
70
80
90

(b)

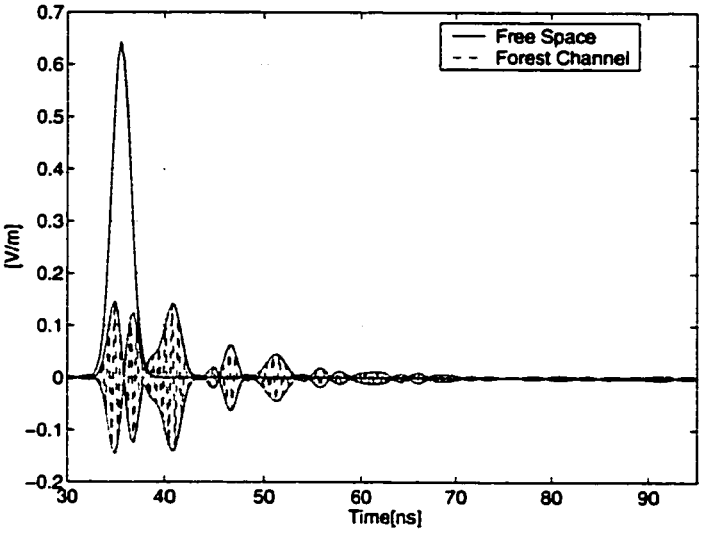

(c)

Figure 4.19: Time-domain response of a narrow pulse transmission through a pine forest. The pulse is incident at 40^o. (a) E_x. (b) E_y. (c) E_z.

CHAPTER 5

Application: A Hierarchical Time-Domain Modulation Scheme for Wideband Communications

5.1 Introduction

Ultra-wideband (UWB) communication is an emerging wireless technology where modulation schemes that make use of very large fractional bandwidths are proposed for transmitting information. In recent years the application of ultra-wideband communication has achieved a significant prominence because it offers many capabilities that are attractive in tactical communication and radar. These include resistance to jamming and cosite interference, exceptional multipath resolution (precise ranging), simple system implementation, and very low probabilities of signal interception and detection [51]. Recently Federal Communications Commission (FCC) allocated a frequency band, 3.1 - 10.5 GHz, for commercial applications. Depending on the application, the range of frequency band used, and the propagation channel, it is possible to transmit UWB signals whose spectrum would fall below the thermal noise of most existing systems at observation points sufficiently far from the transmitter. To date most research on UWB communications has focused on a few specific modulation techniques, such as impulse radio.

Basic idea of the ultra-wideband communication is that if a very narrow pulse is trans-

mitted, a direct pulse from a transmitter arrives a receiver point, and then pulses from scatterers in a channel. Therefore if the pulse width is narrow enough, the pulses are not overlapped in time domain, and so the direct pulse can be easily separated from other pulses. Hence performance of UWB systems is much less affected by the undesired channel characteristics such as fading, when compared with conventional narrow band modulation schemes. Another advantage of this technique is that there is no carrier involved. Therefore required complexity of a communication system can be reduced considerably. For example, estimation of channel characteristics becomes excessive, which is necessary for signal processing block (equalizer) in a conventional communication system. Since there is no need for down converting process mixers and local oscillators can be eliminated from a RF front end. However, it is required for all components in the RF front end to operate in ultra-wide band mode. To achieve optimal performance the antennas and amplifiers have to be very wideband and dispersionless. Known candidates among wideband antennas are spiral, or log-periodic, etc., however, although these antannas are wideband they are not dispersionless. Since in general frequency responses of antennas are very strongly dependent on their geometries, it seems practically impossible to make dispersionless and efficient very wideband antennas. Electrically small antennas, by definition, are dispersionless, but they are power inefficient and the required matching network over a wide range of frequency is complicated and may be ddispersive Therefore the ultra-wideband communication scheme may convey the overall system complexity to the complexity of each component. For example efficient ultra-wideband antennas can be designed by applying the same linearization techniques ssimilarto those used for power amplifiers which includes sophisticated signal processing and the associated hardware. A different way for implementing an ultra-wideband system be that a narrow pulse is synthesized in space by many narrow band sub-systems like what is currently available for wideband power amplifiers.

Based on this observation a novel UWB modulation scheme is proposed which allows

for transmission of data according to a user defined hierarchical scheme which is influenced by the channel characteristics. In this approach, the available bandwidth is divided into many sub-bands with linearly increasing bandwidths. The bandwidth allocation scheme is compatible with the design of scalable filters and antennas. For example if the size of an antenna or the capacitances and inductances of a filter are scaled, the center frequency and bandwidth of the antenna or the filter will scale accordingly. For a specific filter or antenna the ratio of the bandwidth to the center frequency is unchanged in a scaling process. This allows for the simple generation of a set of orthogonal waveforms that can carry independent data sets and can be transmitted simultaneously. The impulse response of these filters can be regarded as a set of multi-resolution wavelets. As these waveforms propagate through the channel, depending on the channel characteristics, and the frequency content of each waveform, they experience distortion due to multipath, dispersion, and attenuation. Using this proposed scheme information can be compressed into a narrow pulse while the impulse radio send a bit per one pulse. To assess the performance of this system an accurate propagation model for a forest environment is used which is explained in Chapter 3. Transmission of an image through the forest is simulated, for the proposed modulation scheme and an impulse radio scheme and quality of the received images for both receivers is compared.

5.2 Basic Idea

The impulse response of a wireless communication channel can be determined by transmitting a narrow pulse through it. At the receiver the transmitted pulse may be broadened due to dispersive effect, frequency components may be absent due to significant multi-path fading, and attenuation of the signal may occur [38]. In general high frequency components of the pulse tend to be more affected by these channel characteristics than low frequency components. Based on this, the UWB hierarchical communication scheme is proposed.

This proposed system is described in Fig. 5.1. A pulse generator produces a very narrow

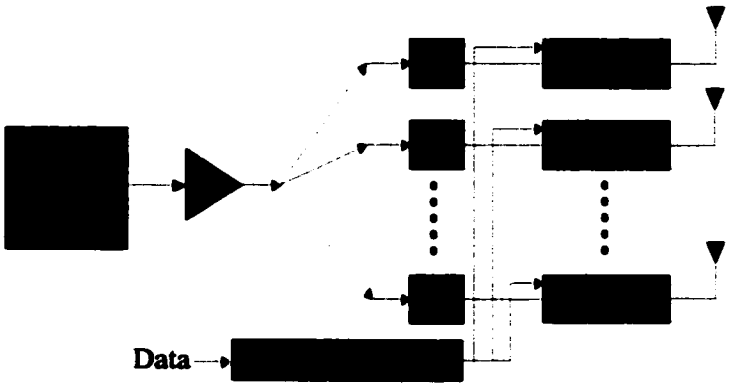

Figure 5.1: Block diagram of a transmitter.

pulse that is fed through a bank of scaled bandpass filters (BPF). The waveforms are modulated by a data stream according to a hierarchical scheme. For example, the most important data is modulated on the lowest order waveform (lowest frequency), the next most important data is modulated by the following order waveform, and so on. Each modulated signal is radiated independently by its own antenna as shown in Fig. 5.1. These antennas are also scaled versions of the antenna for the lowest order waveform. The block diagram of the receiver is the same as that of the transmitter, but the order of components is reversed. Each antenna receives a signal, and the received signal goes through a similar bank of filters to separate each waveform before demodulation. One important advantage of this scheme is that each carrier is approximately orthogonal to the rest in both the time and frequency domains. The degree of orthogonality of these waveforms will depend on the separation between the center frequencies and the order of these filters.

To obtain a set of scalable filters, the center frequencies of the filters are determined using the following procedure:

$$f_1 = \frac{f_s}{1 - \frac{Q}{2-\alpha}}, \qquad f_n = f_{n-1} \cdot g \tag{5.1}$$

where f_n is the center frequency of the nth filter, $g = \frac{1+\frac{Q}{2-\alpha}}{1-\frac{Q}{2}}$, Q is the percent bandwidth,

f_s is the lowest frequency of the system, and α is an isolation factor that determines the spacing between two adjacent center frequencies (> 1).

5.3 Numerical Simulation

In this section, assessment of the proposed system in a forested area is considered. For this simulation 200MHz bandwidth (10MHz - 210MHz), 20% filter bandwidth ($Q = 0.2$), and $\alpha = 1.2$ are assumed. Figure 5.2 shows the frequency responses of bandpass filters (12th order Butterworth) designed using (5.1). A physics-based propagation model which is developed in Chapter 3 is used to estimate the frequency characteristics of a forest channel with tree density of $0.05/m^2$. To include the effect of multiple scatters 30 trees near the transmitter, and 20 trees around the receiver are considered. Effective dielectric constant of the forest is assumed to be $1.03 + i0.006$, and the average height of the forest is 20m. Dielectric constant of a tree trunk is $5 + i$, its radius is assumed to be 25cm, and the average trunk height is 15m. The transmitter is located 17m below the top of the forest, and the receiver is 1000m distant. The transmitter and receiver antennas are both vertical infinitesimal dipoles. Two communication scenarios are considered. The first case is that of a transmitter distant from any trees (> 1m) so that a transmitted pulse will not be severely distorted by the trees. Figure 5.3(a) shows the time domain response for this case, which clearly indicates some small distortion and ringing due to the multipath effect. The second case is that of a transmitter near a tree (10cm distant from the tree). The proximity of the tree significantly distorts the pulse as seen in figure 5.3(b). For this case the effect of multipath is much stronger, and preserved for a longer time than the previous case as seen in the figure. The time domain channel responses for the both cases are calculated from only 300 frequencies points (using a non-uniform sampling method (see Chapter 3)). To minimize the number of frequency points, the time domain response of the channel is first calculated using Gauss quadrature [39] and from the time domain

response the frequency domain response is reconstructed with more frequencies points. Since the Gauss quadrature technique puts less sampling points near edges of the integral, interpolation of the low and high frequency portion is not as accurate as for the center frequency portion of the simulated frequency band. Figures 5.4 and 5.5 show comparisons of calculated channel responses using a Gaussian pulse transmission with uniform sampling compared with results using non-uniform scheme. The two results are well matched, and as mentioned earlier, at the edge of frequency band small discrepancies are observed. For the second case, seen in figure 5.5, the difference is greater because in the time domain the ringing due to the interaction among trees is preserved over a longer time span, and hence for 300 frequency points, small ripples (high order interactions among tree trunk) may be missed. However the interpolated responses are still acceptable.

In the next figure 5.6 the received waveforms are compared with the transmitted waveforms. One is a waveform for the first sub-band (lowest frequency), and the other for the 7th sub-band. As seen in the figure it is clearly observed that the first sub-band is not significantly affected by the communication channel as expected, but the 7th sub-band is severely distorted by the channel for the second case. The magnitude of individual waveform is scaled to unity for the purpose of comparison. The next figure 5.7 shows an actual image compared with a transformed image using a two level wavelet transform of the original image with the Daubechies wavelet. The transformed image consists of 7 sub images, and is transmitted over 7 sub-bands by the following rule. The lowest frequency portion of the image with fewer pixels is sent over the lowest frequency transmission band, the next lowest portion over the next lowest frequency band, and so on. To demodulate the received data, a coherent demodulation scheme is used for both the proposed system and the impulse radio scheme [38]. At the receiver Gaussian noise is assumed and added to the received signal. Its variance is determined by the receiver noise temperature. For the proposed system, the variance can be calculated by the formula, $KT_e \cdot SNR \cdot B$. Here K is Boltzmann's constant, T_e is the efficient temperature, SNR is signal-to-noise ratio that is

assumed to be 10dB, and B is the system bandwidth. For a calculation of T_e a noise figure of 1.5dB, and a room temperature of $290°K$ are assumed. For the impulse radio scheme, the variance is computed by $\frac{\sqrt{\pi}}{6}KT_e \cdot SNR \cdot B$. Amplitude shift keying (ASK) modulation is used as a modulation scheme. This allows the optimal demodulation algorithm to be known theoretically. If the noise level is less than half of the received signal level, correct data can be restored, otherwise an error is occurred [38]. Applying this rule the transmitted images can be demodulated, and results are plotted in figure 5.8, which are received by the impulse radio receiver. For this case transmitter power is assumed to be 5mW. A similar demodulation was done for the proposed system and is shown that the image with a minimum distortion can be reconstructed. In the next figure 5.9 mean square error (MSE) is plotted as a function of the transmitter power. The mean square error is defined as

$$MSE = \frac{1}{N}\sum_i \sum_j |Y_{ij} - Y'_{ij}|^2 / |Y_{ij}|^2$$

where Y_{ij} is the original image, Y'_{ij} is the received image, and N is the total number of pixels in the image. As seen in figure 5.9 the mean square error of the proposed system for the second case is a little smaller than for the first case at very low transmitted power. This is because the nearby tree can act as a large antenna, and so more power is received at low frequency with the tree in close proximity than when the tree is absent. The low frequency bands contain more critical data for reconstruction of the original image. As mentioned, in order to compare the performance of the proposed system with that of the impulse radio system, ASK is used. However if another modulation scheme such as phase shifting keying (PSK) is used, the performance of the proposed system should become much better [38].

5.4 Conclusion

A novel signaling scheme was proposed for ultra-wideband communications. This scheme divides the whole frequency band into many sub-bands. Unlikely conventional

orthogonal frequency division multiplexing (OFDM), the bandwidth of each individual sub-band is linearly proportional to frequency. Due to the scalability of BPFs and antennas at the lowest frequency the impulse responses of BPFs can be directly used as carriers which are orthogonal to each other in both time and frequency domains.

To assess performance of the proposed system, a communication scenario in a forest was considered in which a transmitter sends an image to a receiver imbedded in the forest using two signaling schemes, the proposed one and the impulse radio method. A hierarchical scheme is applied which transforms the image using wavelets which divides the image into several sub-images according to its frequency component. In the presence of thermal noise the transmitted image was restored as the transmitted power was varied. This simulation showed that the performance of the proposed system is much less sensitive to transmitted power fluctuation.

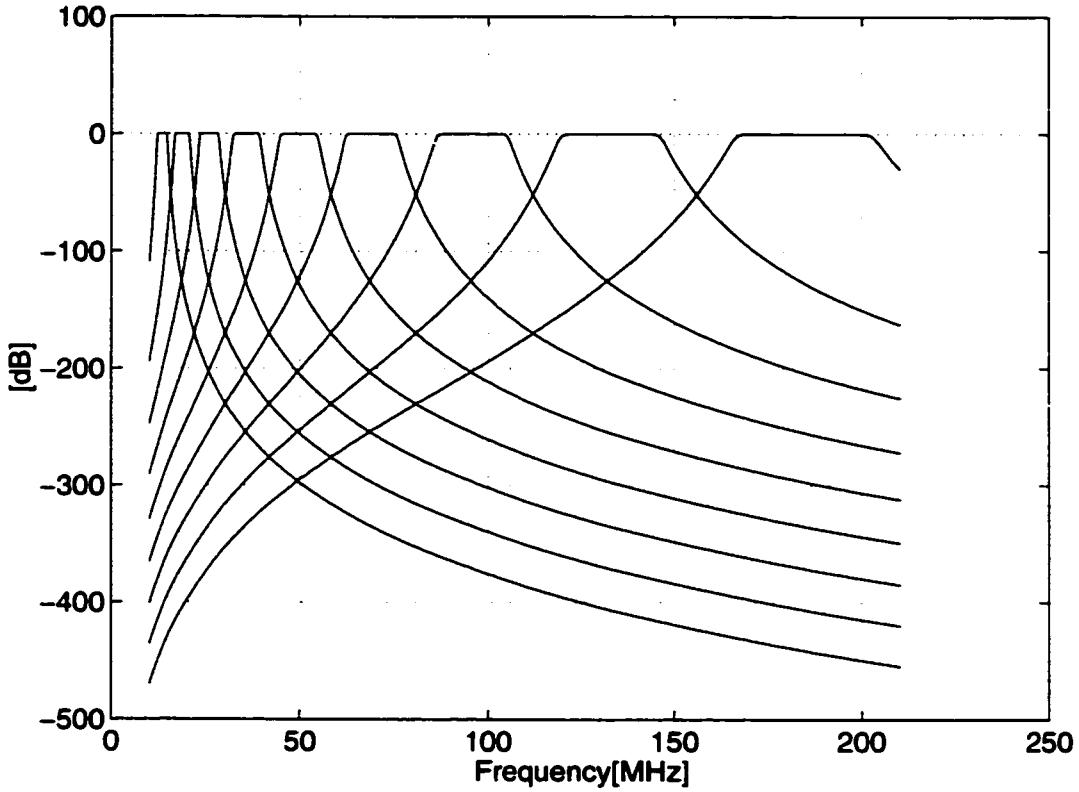

Figure 5.2: Frequency responses of 9 Butterworth filters of 12th order with a maximum inter-channel cross-talk of better than 80dB.

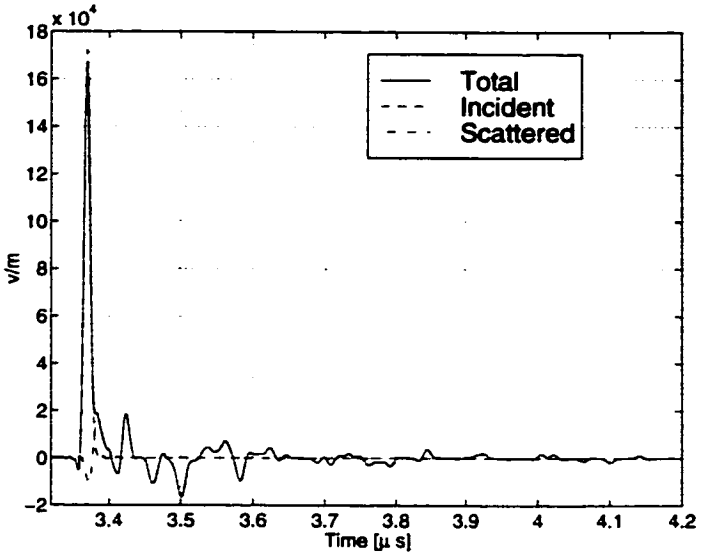

(a)

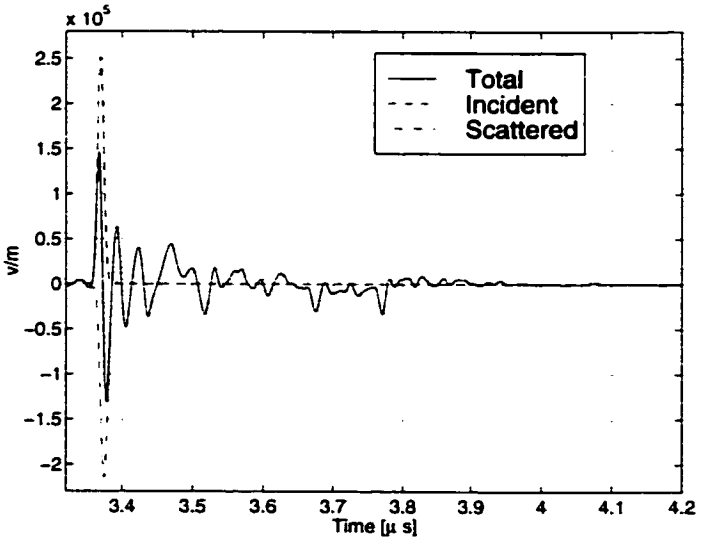

(b)

Figure 5.3: Plots of time domain responses of the forest channel at the receiver. Incident, scattered, and total field are plotted. (a) When the transmitter is away from trees (b) When the transmitter is very close to a tree.

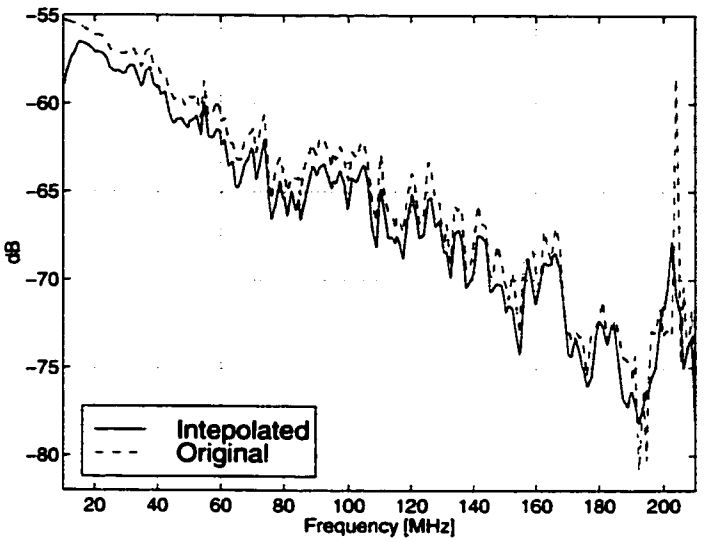

(a)

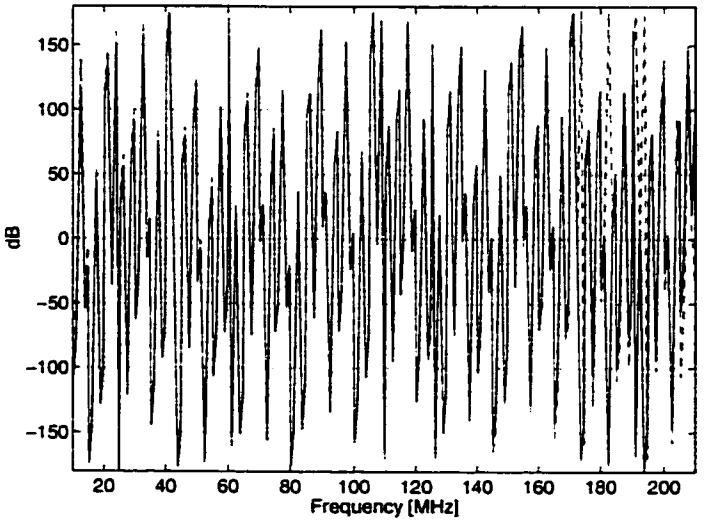

(b)

Figure 5.4: Comparison of the originally calculated channel response in the frequency domain with the interpolated channel response when the transmitter is away from trees. (a) Magnitude (b) Phase.

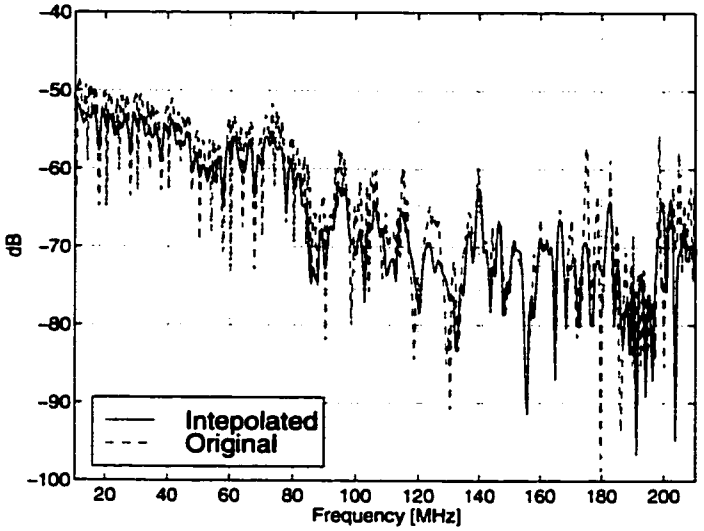

(a)

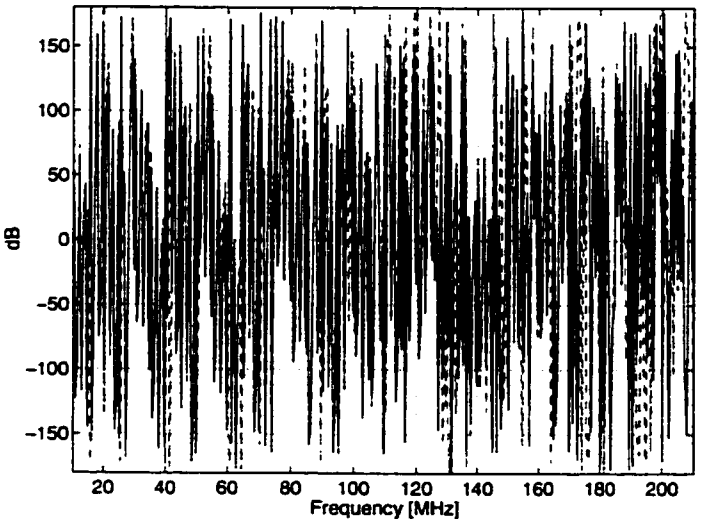

(b)

Figure 5.5: Comparison of the originally calculated channel response in the frequency domain with the interpolated channel response when the transmitter is very close a tree. (a) Magnitude (b) Phase.

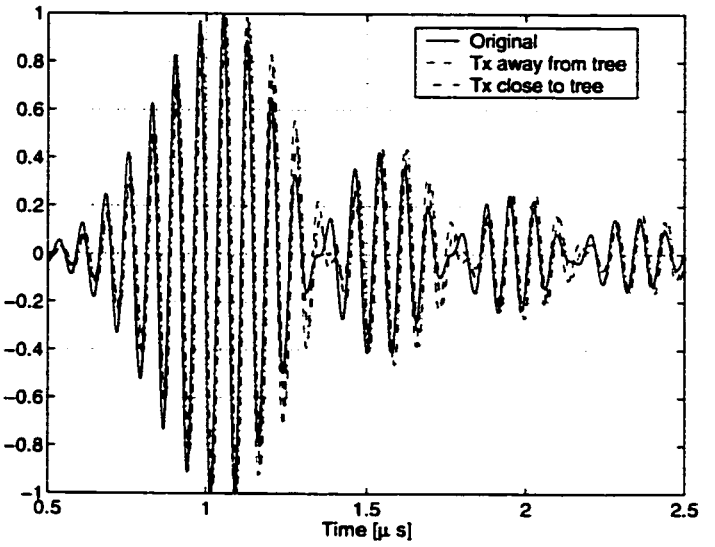

(a)

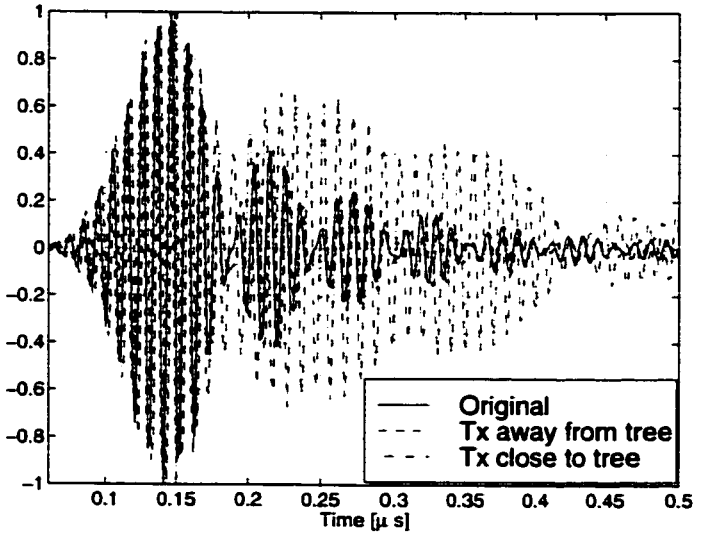

(b)

Figure 5.6: Comparisons of the waveforms at the transmitter with those at the receiver for two situations. All signals are scaled to unity. (a) The first sub-band (b) The 7th sub-band.

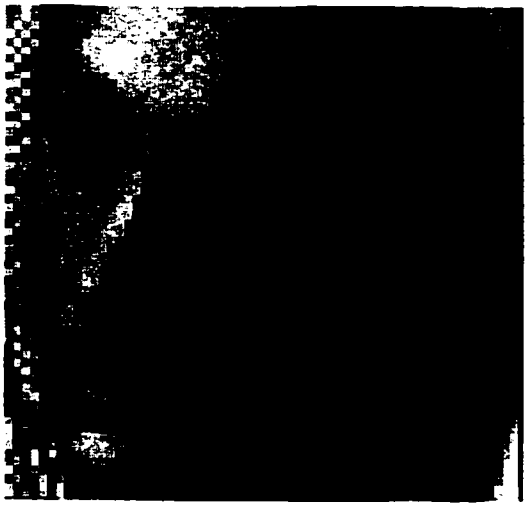

(a)

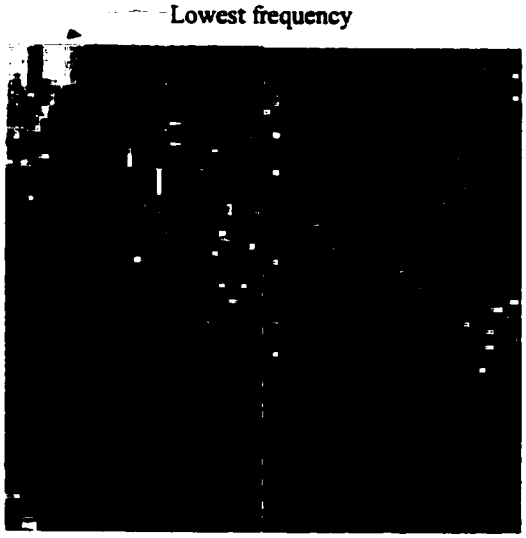

(b)

Figure 5.7: Plots of the original image and transformed image using the second level wavelet transform with Daubechies wavelet. (a) Original image (b) Transformed image.

(a)

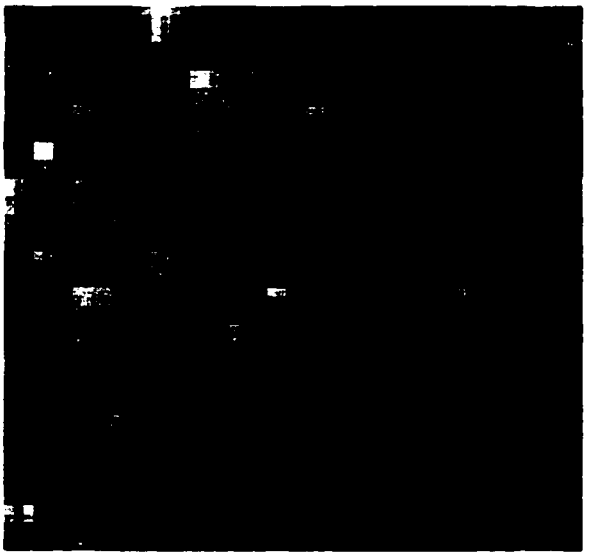

(b)

Figure 5.8: Received images by the impulse radio for the two situations. (a) When the transmitter is away from trees (MSE = 1.1752) (b) When the transmitter is very close to a tree (MSE = 1.1869).

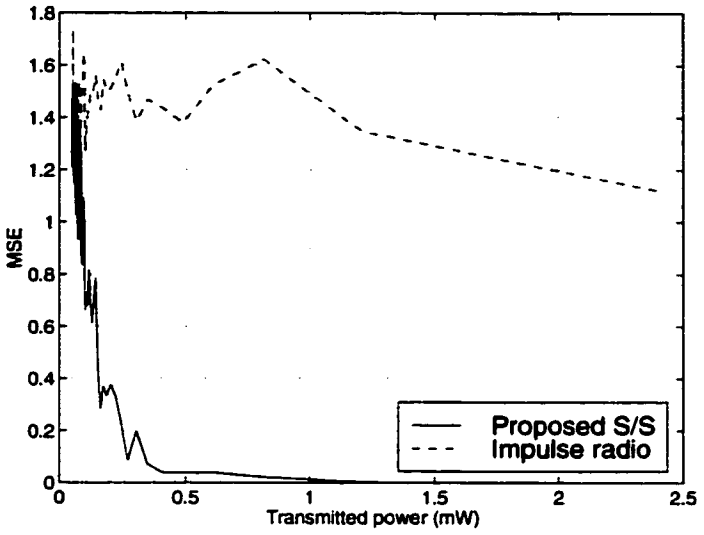

(a)

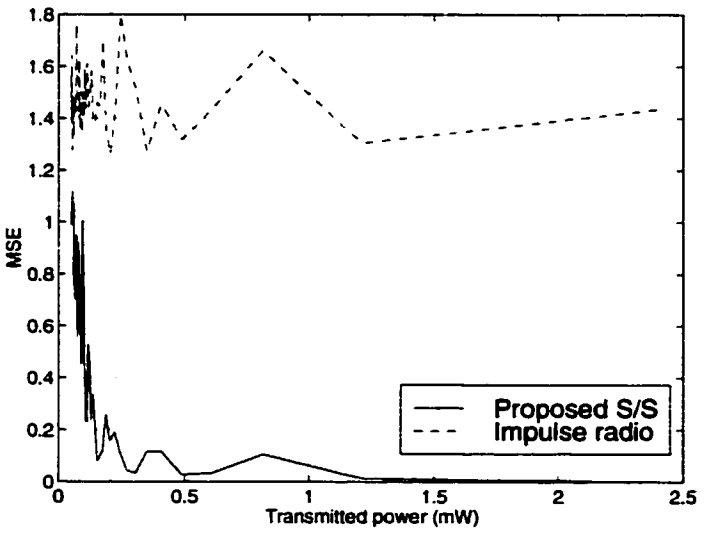

(b)

Figure 5.9: Plots of the mean square error of the received image by the proposed system and the impulse radio as a function of transmitted power. (a) When the transmitter is away from trees (b) When the transmitter is very close to a tree.

CHAPTER 6

Channel Model for Urban Areas

6.1 Introduction

A scenario of interest in wireless communications is urban environment which consists mainly of building structure. The complexity of wave propagation problem in urban environment is beyond the capability of full-wave analysis. Therefore, as mentioned in Chapter 1, ray tracing techniques are commonly adopted for characterizing urban channels. However in order to apply the ray tracing method, the geometry of channel constituents such as buildings, bridges, etc. are simplified and their surface are assumed to be flat and non-penetrating. The assumption about uniform and flat building surfaces results in an excessive and unrealistic reflected field along the specular direction. Since the technique uses successive calculation of reflected field from many building surfaces between the transmitter and receiver the errors become accumulated and will degenerate the accuracy of the method. To examine the accuracy of basic assumptions in ray tracing method the scattered fields from realistic building surfaces must be calculated in an accurate fashion. In this thesis Method of Moments (MoM) is used for this purpose. Generally, buildings are electrically very large, and hence a fast solver like fast multipole method (FMM) is needed to calculate scattering and diffraction from buildings. FMM formulation exists for free space problems. In this Chapter an efficient FMM identity is formulated for scattering problems

where objects are above or on an impedance surface. Using conventional MoM the problem of cosite interference in Direct Sequence Code Division Multiple Access (DSCDMA) system is simulated.

6.1.1 Fast Multipole Method Based on Exact Image Theory

The Sommerfeld problem, radiation of a short dipole above an infinite dielectric half-space, is a classic problem in electromagnetics that has received significant attention through the years and because of its importance has remained contemporary. The formal solution is represented by integrals whose integrands are highly oscillatory and slowly decaying. These properties make direct numerical integration computationally very inefficient. For impedance surfaces however, an efficient method known as exact image theory has been implemented [52]. Since this formula replaces the poorly converging integrands of the Sommerfeld integral with exponentially decaying integrands, calculation of the fields from an arbitrary source above an impedance surface can be performed very efficiently, independent of the relative locations of the source and observation points. Hence based on this exact image theory it is much easier to compute scattering from a complex object above an impedance half-space using a common numerical method such as the method of moments (MoM). However numerical complexity of MoM is at best $O(N^2)$, which prohibits the method to be applied to electrically large objects. To overcome this difficulty, in recent years several methods have been proposed. These include fast multipole method (FMM) [53], adaptive integral method (AIM) [54], and many other variations of FMM and AIM. FMM has been rigorously formulated for the free-space Green's function, and successfully applied to a large class of problems ranging from passive circuit analysis to computation of the radar cross section (RCS) of complex objects. In recent years the FMM algorithm has been extended to include scattering problems in the presence of a dielectric half space using the method of complex images [55]. The method of complex images approximates part of the integrand of the Sommerfeld integral by Prony's method in terms of a summation

of exponential functions which can then be integrated analytically. The result is a summation of discrete image points in the complex Z-plane. The drawback of this method is that depending upon the location of observation point and source points (especially if they are close to the surface) the number of exponential terms in the Prony's approximation needs to be increased. In this Chapter using the exact image formulation, an efficient multipole representation of the Green's function for impedance surfaces is obtained and is shown to be very accurate for all locations of source and observation points.

6.1.2 Cosite Interference for DSCDMA System

The spread spectrum signals have been very popular and have found various applications, ranging from radars for obtaining a fine resolution and low peak power, to communications for anti-jamming capabilities and suppressing the effects of interference. From early 1950s a communication scheme has been studied by various research groups [56] which is now known as code division multiple access (CDMA). In modern CDMA schemes all users share the entire frequency band that is allocated for the service, and the individual users are distinguished by their own unique code which is called pseudo-random, or pseudo-noise (PN) code. Unfortunately correlation between two PN codes is not exactly zero. Hence the so-called cosite or co-channel interference (CCI) is the most dominant factor in limiting user capacity, while other schemes such as TDMA and FDMA are limited by the bandwidth [56]. In general cosite interference occurs when several nearby terminals communicate with a base station simultaneously. In this case each terminal receives not only the signal from the base station, but also the signals from the transmitter in their proximity. In spite of the fact that the base station is located atop of a building or a tower, and transmits high power signal with a high gain antenna, the signals from nearby transmitters may be much stronger than the power from the base station due to shadowing and multipath. Because of the non-zero correlation property of PN code, the desired signal can be much weaker than the undesired interfering signals. This phenomenon is known as cosite

interference or CCI for CDMA systems.

Because of its importance this topic has received much attention in recent years [56]. To study and treat this problem, so far simple channel models which have a very limited range of accuracy and are inherently narrow bandwidth have been used. It is clear that accuracy of the cosite interference analysis is strongly dependent on the accuracy of the channel model used. Therefore in this Chapter a full-wave solution based on a Method of Moments (MoM) is applied to calculate field behavior in a channel which includes a number of transmitters and scatterers above an impedance surface. Based on this field calculation cosite interference for a DSCDMA system is simulated using a Monte Carlo simulation.

6.2 Overview of Fast Multipole Method

Fast Multipole Method (FMM) was first formulated by Rokhlin [57] for 2D acoustic scattering problems. Over the past decade the FMM formulation has been applied to a wide range of problems, such as analysis of electromagnetic scattering from large objects to computation of gravitational interactions among many bodies. FMM is applied to the discretized form of an integral equation, such as the method of moments (MoM), whose solution is sought using iterative approach. In this approach the MoM mesh (discretized domain) is grouped into many subdomains (FMM clusters), and then the far-field interactions among centers of FMM clusters are calculated exactly. Next these interactions are translated to interactions between actual MoM cells by a properly defined translation operator. Addition theorem for the integral kernel, in electromagnetics Green's function, is used to diagonalize the translation operator. Following this procedure the computational complexity can be reduced from $O(N^2)$ to $O(N^{4/3})$ for 2D problems, and to $O(N^{3/2})$ for 3D problems if the number of groups is chosen to be proportional $\sqrt{N}$ [53, 58]. To further reduce the complexity the FMM idea is combined with the multilevel algorithms to be able

to achieve $O(N\log N)$ or $O(N)$ complexity [58, 59].

According to addition theorem, the scalar Green's function in free space can be written as [59]

$$\frac{e^{jk|\vec{X}+\vec{d}|}}{|\vec{X}+\vec{d}|} \approx \frac{jk}{4\pi}\int d^2\hat{k}e^{j\vec{k}\cdot\vec{d}}T_L(kX,\hat{k}\cdot\hat{X}) \tag{6.1}$$

where $T_L(\cdot)$ is a truncated infinite series given by $T_L(kX,\cos\theta)=\sum_{l=0}^{L} j^l(2l+1)h_l(kX)P_l(\cos\theta)$, and $\vec{X}$. Here P_l, and h_l are Legendre and spherical Bessel function, respectively, and $\vec{d}$ are defined in Fig. 6.1. The nmth element of an impedance matrix of a MoM formulation can be simply expressed with a proper linear operator (£) and using (6.1) the source and observation coordinates can be separated using vector relationship, $\vec{r}_n-\vec{r}_m=\vec{X}+\vec{d}_1-\vec{d}$, like

$$Z_{nm}=£_{nm}\frac{e^{jk|\vec{r}_n-\vec{r}_m|}}{|\vec{r}_n-\vec{r}_m|}=\frac{jk}{4\pi}\int d^2\hat{k}£_n\cdot T_L(kX_p,\hat{k}\cdot\hat{X}_p)\cdot £_m$$

where $£_n$, and $£_m$ are dependent only on the source and observation coordinate, respectively, and represented by $£_m=\int_{s'} ds'[\bar{\bar{I}}-\hat{k}\cdot\hat{k}]e^{j\vec{k}\cdot\vec{d}}\vec{f}_m$ where $\vec{f}_m$ is a basis function. Specifying the

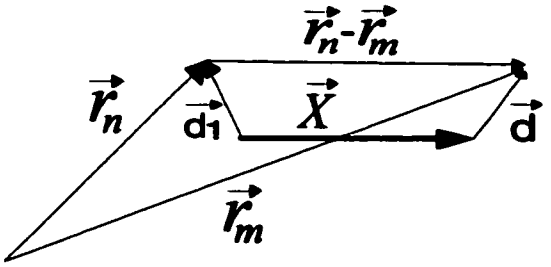

Figure 6.1: Relation of vectors, $\vec{X}$, $\vec{d}$, $\vec{r}_n$, and $\vec{r}_m$.

unknown vector by I (induced surface or polarization current), and the excitation vector by V, the integral equation in the MoM reduces to $ZI=V$. If the total number of unknowns is denoted by N and the number of unknowns in each subdomain is represented by N_s, then there are N/N_s FMM clusters and the matrix-vector multiplication can be written

mathematically as

$$\tilde{V}_n = \sum_{m=1}^{N} Z_{nm}\tilde{I}_m = \sum_{m=1}^{N} \pounds_{nm}\frac{e^{jk|\vec{r}_n-\vec{r}_m|}}{|\vec{r}_n-\vec{r}_m|}\tilde{I}_m$$
$$= \frac{jk}{4\pi}\int d^2\hat{k}\sum_{r=1}^{N_s}\pounds_n \cdot \sum_{p=1}^{N/N_s} T_L(kX_p,\hat{k}\cdot\hat{X}_p)\cdot\sum_{q=1}^{N_s}\pounds_m I_{pq} \qquad (6.2)$$

$T_L(\cdot)$, and $e^{i\vec{k}\cdot\vec{d}_{pq}}$ are pre-calculated in k space ($\hat{k}$) and stored. To reduce the complexity of matrix-vector multiplication first the third summation in (6.2), $\sum_{q=1}^{N_s}\pounds_m I_{pq}$, is calculated for each FMM cluster, and stored. This step requires $O(KN)$ operations. Next the second summation in (6.2), $\sum_{p=1}^{N/N_s} T_L(kX_p,\hat{k}\cdot\hat{X}_p)$, is performed between every FMM clusters. The number of required operators for this step is $O(K\frac{N^2}{N_s^2})$ where K is a number for calculation of the double integration, which may approach asymptotically N_s. Finally the first summation and integration, $\int d^2\hat{k}\sum_{r=1}^{N_s}\pounds_n$, are performed for every MoM cells. It needs $O(KN)$ operations. Hence the total number of multiplication required for the matrix-vector product is $O(KN+K\frac{N^2}{N_s^2}+KN = KN+K\frac{N^2}{N_s^2})$. To minimize the value, $KN+K\frac{N^2}{N_s^2} = N_sN+\frac{N^2}{N_s}$, N_s is chosen to be $\sqrt{N}$, and total number of multiplication is reduced to $O(N^{3/2})$ from $O(N^2)$.

6.3 Fast Multipole Representation of Impedance Surface Green's Function

For an infinitesimal dipole located at (x',y',z') above an surface with a normalized impedance of η, the total field can be written [52] as (See Appendix D)

$$\begin{aligned}\vec{\mathbf{E}} =& \vec{\mathbf{E}}^d + \vec{\mathbf{E}}^i + j2k_0Z_0\left[\frac{e^{jk_0R}}{4\pi R} - \alpha\int_0^\infty e^{-\alpha\xi}\frac{e^{jk_0R'}}{4\pi R'}d\xi\right](l_x\hat{x}+l_y\hat{y}) - \\ & j2Z_0\eta l_z\hat{z}\left[\left(j\frac{\partial}{\partial z}+\beta\right)\frac{e^{jk_0R}}{4\pi R} + (k_0^2-\beta^2)\int_0^\infty e^{-\beta\xi}\frac{e^{jk_0R'}}{4\pi R'}d\xi\right] + \\ & 2Z_0\eta\hat{l}\times\left(\frac{\partial}{\partial y}\hat{x}-\frac{\partial}{\partial x}\hat{y}\right)\left[\frac{e^{jk_0R}}{4\pi R} - \beta\int_0^\infty e^{-\beta\xi}\frac{e^{jk_0R'}}{4\pi R'}d\xi\right] + \\ & j\frac{2Z_0\eta}{1-\eta^2}\left\{\frac{\partial^2}{\partial x^2}l_x\hat{x}+\frac{\partial^2}{\partial y^2}l_y\hat{y}+\frac{\partial^2}{\partial x\partial y}(l_y\hat{x}+l_x\hat{y})\right\}\int_0^\infty(e^{-\alpha\xi}-\eta^2e^{-\beta\xi})\frac{e^{jk_0R'}}{4\pi R'}d\xi\end{aligned} \tag{6.3}$$

where $\vec{\mathbf{E}}^d$ and $\vec{\mathbf{E}}^i$ are fields from the dipole itself and its image in a perfect conductor, respectively. Also in (6.3) $\alpha = k_0/\eta$, $\beta = k_0\eta$, $R' = \sqrt{(x-x')^2+(y-y')^2+(z+z'+j\xi)^2}$, $R = \sqrt{(x-x')^2+(y-y')^2+(z+z')^2}$, and $\hat{l}$ is the orientation of the dipole. For $\vec{\mathbf{E}}^d$ and $\vec{\mathbf{E}}^i$, the well-known FMM algorithm can be used [53]. However for the rest of equation (6.3), a new multipole representation is needed in order to separate the Green's function in terms of sum of the products of two functions one dependent on the source coordinate and the other dependent on the observation coordinate. To achieve this goal, a multipole expansion of $I = \int_0^\infty e^{-p\xi}\frac{e^{jk_0R'}}{R'}d\xi$ is needed ($p = \alpha$ or β). One can attempt to express $\frac{e^{jk_0R'}}{R'}$ in the integrand of I in terms of its multipole expansion. However since the domain of ξ extends to infinity such substitution is not rigorously justified. However noting that there is another exponentially decaying function in the integrand the integral range can be truncated i.e.,

$$I = \int_0^\infty e^{-p\xi}\frac{e^{jk_0R'}}{R'}d\xi \approx \int_0^a e^{-p\xi}\frac{e^{jk_0R'}}{R'}d\xi \tag{6.4}$$

where a is chosen so that

$$e^{\Re[jk_0R'-p\xi]}|_{\xi=a} = e^{-\frac{k_0}{\sqrt{2}}\sqrt{\sqrt{(R^2-a^2)^2+4R^2a^2\cos^2\theta}-R^2+a^2}-\Re[p]a} << 1$$

This choice of a also satisfies the condition for which the following addition theorem for the scalar Green's function is valid. Using the Gegenbauer's addition theorem, the integrand (scalar Green's function with complex range function) is expanded as

$$\frac{e^{jk_0R'}}{R'} = jk_0\sum_{n=0}^{\infty}(-1)^n(2n+1)P_n(\cos\theta_2)h_n(k_0X)j_n(k_0d) \tag{6.5}$$

where P_n is the Legendre polynomial, and h_n and j_n are the spherical Bessel functions.

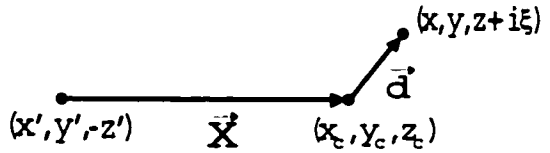

Figure 6.2: Definition of vectors, $\vec{X}$, and $\vec{d}$.

Also $X = \sqrt{(x_c-x')^2+(y_c-y')^2+(z_c+z')^2}$, $d = \sqrt{(x-x_c)^2+(y-y_c)^2+(z-z_c+j\xi)^2}$, and θ_2 is a complex angle between $\vec{X}$ and $\vec{d}$ vectors given by $\theta_2 = \cos^{-1}(\hat{X}\cdot\hat{d})$ (see Fig. 6.2). This expansion is valid for the condition $|X| > |de^{\pm j\theta_2}|$. Using the plane wave expansion representation of P_nj_n

$$P_n(\cos\theta_2)j_n(k_0d) = \frac{(-j)^n}{4\pi}\int_{4\pi}d^2\hat{k}e^{j\vec{k}\cdot\vec{d}}P_n(\hat{k}\cdot\hat{X}) \tag{6.6}$$

where $\vec{k} = k_0(\sin\nu\cos\psi\hat{x}+\sin\nu\sin\psi\hat{y}+\cos\nu\hat{z})$ and $\hat{k} = \vec{k}/k_0$. Substituting (6.6) in (6.5) and (6.4) and then performing integration with respect to ξ, I can be written as

$$I \approx \frac{jk_0}{4\pi}\sum_{n=0}^{\infty}j^n(2n+1)h_n(k_0X)\int_{4\pi}d^2\hat{k}P_n(\hat{k}\cdot\hat{X})e^{j\vec{k}\cdot\vec{d}_1}\frac{1-e^{-(k_0\cos\nu+p)a}}{k_0\cos\nu+p}$$

where $\vec{d}_1 = (x-x_c)\hat{x}+(y-y_c)\hat{y}+(z-z_c)\hat{z}$. In limit as a goes to infinity

$$I = \frac{jk_0}{4\pi}\sum_{n=0}^{\infty} j^n(2n+1)h_n(k_0X)\int_{4\pi} d^2\hat{k}P_n(\hat{k}\cdot\hat{X})\frac{e^{j\vec{k}\cdot\vec{d}_1}}{k_0\cos\mathrm{v}+p} \tag{6.7}$$

As will be shown later identity (6.7) converges very quickly when $|p/k| > 1$. This is the case for horizontal polarization ($p = \alpha = k_0/\eta$) and when the magnitude of the surface normalized impedance is less than unity $|\eta| < 1$. These values of surface normalized impedance corresponds to impedance of ground at UHF band and below or water surfaces below 10 GHz.

Unfortunately, the series convergence may become rather poor for vertical dipole when $p = \beta$ a case where $|\eta/k_0| < 1$. As $\Re[p]$ decreases, each term in the summation decays slowly as n increases, and the partial summation starts to oscillate. This increases the required number of terms in the summation needed for convergence and hence the expansion becomes numerically unstable. To examine the validity of (6.7) a different approach is used. Integrating I by parts and using the fact, $\frac{\partial}{\partial\xi}\frac{e^{jk_0R'}}{R'} = j\frac{\partial}{\partial z'}\frac{e^{jk_0R'}}{R'}$, the following differential equation for I is obtained:

$$\frac{\partial I}{\partial z'} + jpI = j\frac{e^{jk_0R}}{R} \tag{6.8}$$

Multiplying (6.8) by $e^{jpz'}$, I can be written as

$$I = je^{-jpz'}\int \frac{e^{jk_0R}}{R}e^{jpz'}dz'$$

By expanding the integrand with (6.5) and performing integration with respect to z' the same formulation given by (6.7) is obtained. Therefore it can be concluded that the expansion (6.7) is exact when it converges. For $p = \beta$ and in situation when convergence is poor (the region of poor convergence will be specified later) an approximate identity can be formulated. This approximate formulation is much less efficient than the expansion given

by (6.7). Using a Gaussian quadrature numerical integration, I can be approximated as a finite summation of the form that resembles the method of complex images, i.e.,

$$I \approx \sum_{n=1}^{N} w_i e^{-p\xi_i} \frac{e^{jk_0 R_i'}}{R_i'} \tag{6.9}$$

where $R_i' = \sqrt{(x-x')^2+(y-y')^2+(z+z'+j\xi_i)^2}$ with w_i and ξ_i being its weighting factor and zero of the Legendre Polynomial of *nth* order. The term of $\frac{e^{jk_0 R_i'}}{R_i'}$ can be expanded using (6.5). Because of exponential decay in the integrand ($e^{-p\xi}$), the order N can be chosen so that the accuracy of (6.9) is independent of source and observation point coordinates.

6.4 Simulation Results for FMM Representation

For frequency of 50MHz, and a normalized surface impedance (η) of $0.3 - j0.1$ the FMM expressions for I when $p = \alpha$ and $p = \beta$ are compared with numerical calculations. For simplicity $(x', y', -z')$ is located at (0,0,0) and (x_c, y_c, z_c) is at (7,0,2.2). Figure 6.3 shows the magnitude of each term of the summation given by (6.7) for $p = \alpha$ as a function of n for two different surface impedances, $\eta = 0.3 - j0.1$ ($\Re[p] = 3.14$), and $\eta = 0.8 - j0.1$ ($\Re[p] = 1.3$). It is clearly shown in Figure 6.3 that as the real part of p decreases, the convergence of the summation also decreases (terms decay much slower), and begins to oscillate as mentioned earlier. The rest of the figures show comparisons of the results obtained from the FMM expression based on (6.7) and (6.9) with those obtained from direct numerical integration. Consider the following identity defined from (6.7).

$$\frac{e^{jk_0 R}}{4\pi R} - p\int_0^{\infty} e^{-p\xi} \frac{e^{jk_0 R'}}{4\pi R'} d\xi = \frac{jk_0}{(4\pi)^2} \sum_{n=0}^{\infty} j^n (2n+1) h_n(k_0 X) \int_0^{2\pi} \int_0^{\pi} P_n(\hat{k}\cdot\hat{X}) \frac{k_0 e^{j\vec{k}\cdot\vec{d}_1} \cos\nu}{k_0 \cos\nu + p} \sin\nu d\nu d\psi \tag{6.10}$$

Figure 6.4 is a plot of difference between the direct numerical integration (left-handside of (6.10)) and its FMM representation (right-hand side of (6.10)) results as a function of real,

and imaginary part of p/k. For this calculation observation point is fixed at (7.5,0,2.2), and the number of summation terms (N) is 10. As seen in this figure except for the case of $\Im[p/k] < 0.3$ and $\Re[p/k] < 1.2$ the expansion given by (6.7) gives an very accurate result. Hence for practical purposes the identity, (6.7), or (6.10) can be used for all cases except when $\Re[p/k] < 1.2$ and $\Im[p/k] < 0.3$, for which cases the less efficient formula, (6.9) may be used. For a comparison as a function of observation point, the observation point is moved along a parameterized curve $x = x_c + 0.5\cos\phi$, $y = y_c + 0.5\sin\phi$, and $z = z_c$. Figure 6.5 shows comparisons of magnitude, and phase of the two results for $p = \alpha$, respectively. These two results are in an excellent agreement. The next figure shows the same comparisons for $p = \beta$. For this case (choosing $N = 10$), discrepancies of less than 0.2 dB in the magnitude and 1° in phase are observed.

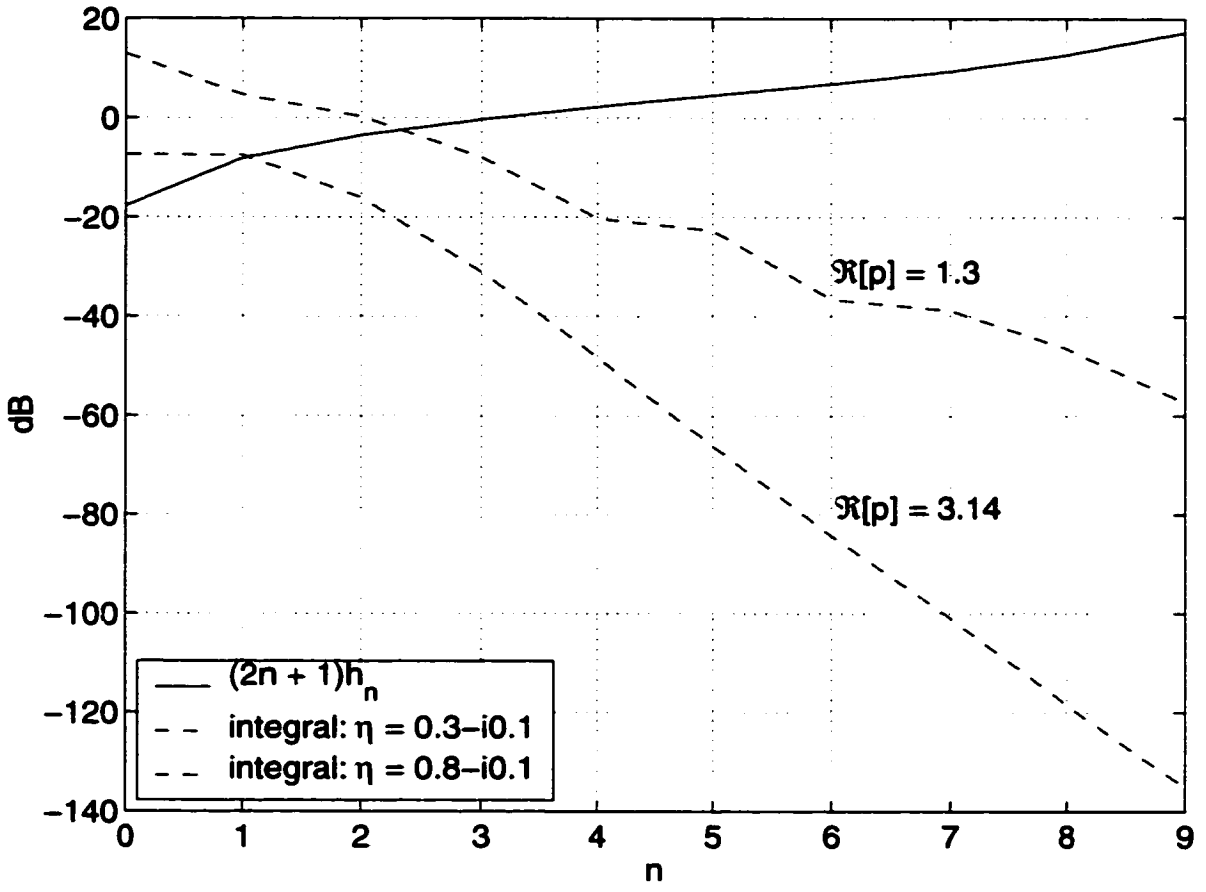

Figure 6.3: Convergence behavior of (6.7) as a function of $\Re[p]$. Magnitude of each term of the summation is shown.

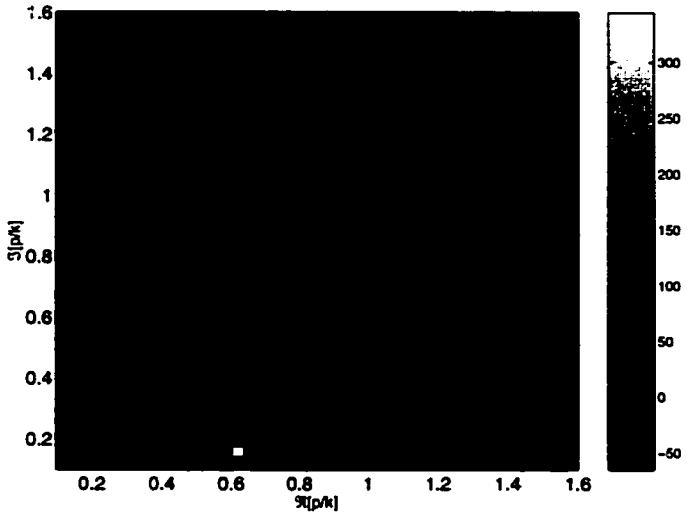

(a)

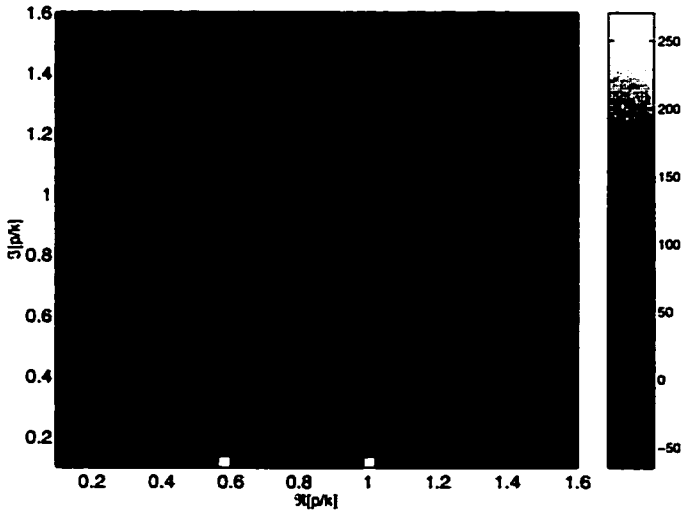

(b)

Figure 6.4: Error between LHS of (6.10) (numerical integration) and RHS of (6.10) (FMM identity) as a function of p/k at 50MHz. Observation point is fixed at (7.5,0,2.2). (a) Relative error of magnitude (b) Phase difference.

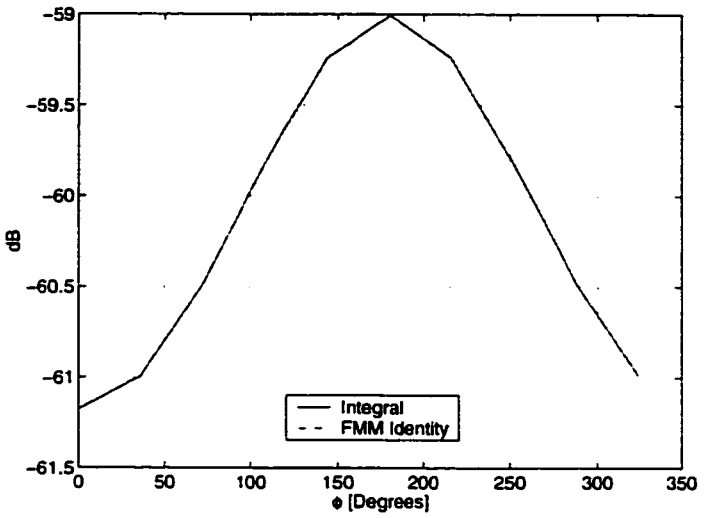

(a)

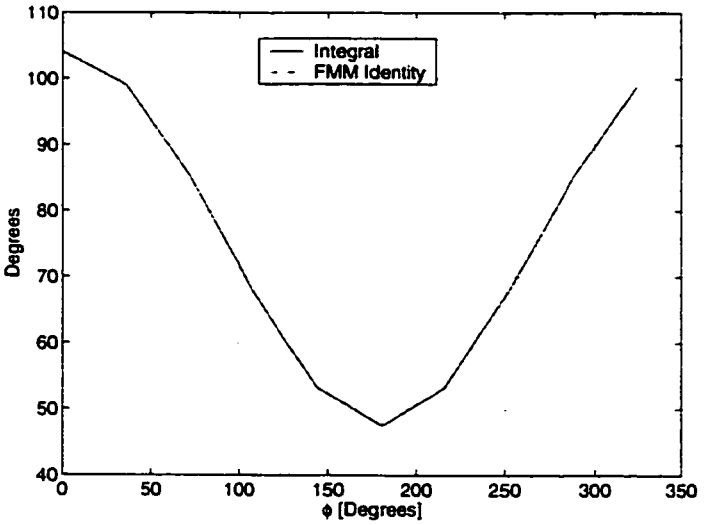

(b)

Figure 6.5: Comparison of LHS of (6.10) (numerical integration) and RHS of (6.10) (FMM identity) when $p = \alpha = 3.14 + 1.05j$ as a function of observation point position, $(7 + 0.5\cos\phi, 0.5\sin\phi, 2.2)$. (a) Magnitude (b) Phase.

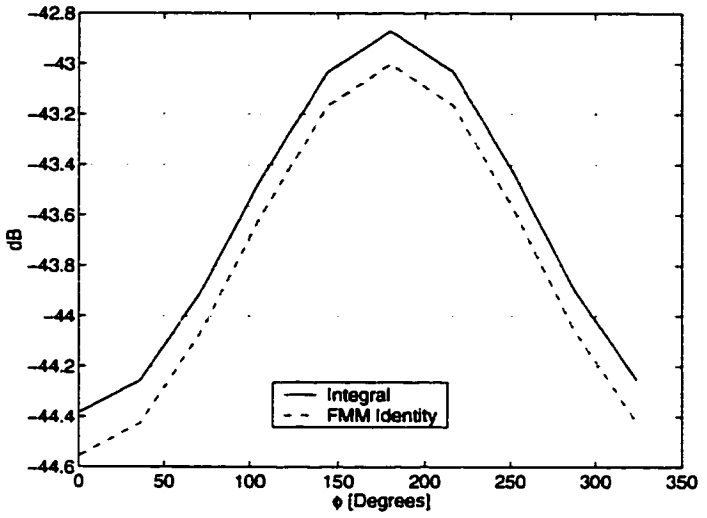

(a)

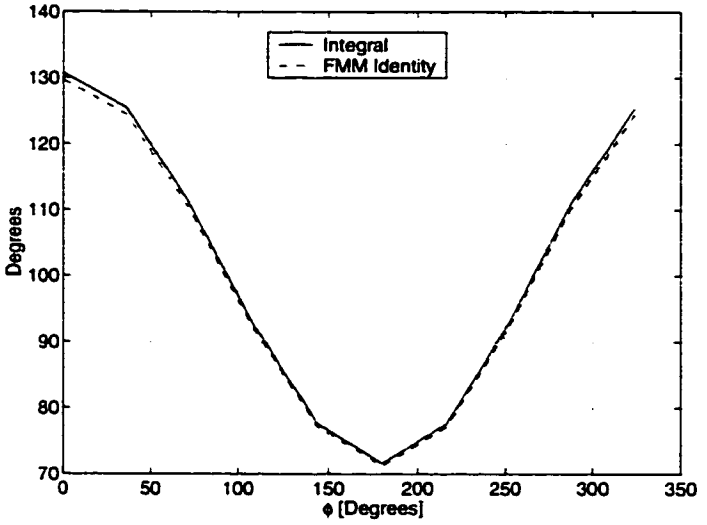

(b)

Figure 6.6: Comparison of LHS of (6.10) (numerical integration) and RHS of (6.10) (FMM identity) when $p = \beta = 0.31 - 0.11j$ as a function of observation point position, $(7 + 0.5\cos\phi, 0.5\sin\phi, 2.2)$. (a) Magnitude (b) Phase

6.5 MoM Formulation Using Exact Image Theory

As mentioned in Chapter 1 the accuracy of the ray-tracing technique is questionable for the case where fields can penetrate the objects and in situations where the object surface is rough. At HF through VHF significant signal penetration through building and objects takes place. In addition typical dimensions of the building surface may not be very large compared to a wavelength. Hence in stead of the ray-tracing MoM is used to calculated scattered fields from objects over an impedance surface. MoM used here is based on a volumetric integral equation in which the Green's function is efficiently calculated using the exact image theory, equation (6.3). For the examples considered here, it was determined that MoM in conjunctions with exact image formulation for half-space impedance surface is sufficient in terms of computational capability. However, for large scatterers the FMM developed in the previous section must be implemented. Pulse basis function and point matching are used to discretize the objects. Matrix elements are formulated analytically by expanding $f = \frac{e^{ikr}}{r}$ by Taylor series. For example,

$$\int_{-\Delta x}^{\Delta x}\int_{-\Delta y}^{\Delta y}\int_{-\Delta z}^{\Delta z}\frac{e^{jkr_m}}{r_m}dz'dy'dx' \approx 4\frac{e^{jkr_{mn}}}{r_{mn}}\Delta x\Delta y\Delta z + \frac{2A_{mn}}{3}\Delta x^3\Delta y\Delta z + \frac{2B_{mn}}{3}\Delta x\Delta y^3\Delta z + \frac{2C_{mn}}{3}\Delta x\Delta y\Delta z^3 \tag{6.11}$$

where

$$\begin{aligned}
A_{mn} &= \frac{\partial^2 f}{\partial x^2} = \frac{e^{jkr_{nm}}}{r_{nm}}\left[\left(\frac{jk}{r_{mn}} - \frac{1}{r_{mn}^2}\right) + \frac{(x-x')^2}{r_{mn}^2}\left(-k^2 - \frac{3jk}{r_{mn}} + \frac{3}{r_{mn}^2}\right)\right] \\
B_{mn} &= \frac{\partial^2 f}{\partial y^2} = \frac{e^{jkr_{nm}}}{r_{nm}}\left[\left(\frac{jk}{r_{mn}} - \frac{1}{r_{mn}^2}\right) + \frac{(y-y')^2}{r_{mn}^2}\left(-k^2 - \frac{3jk}{r_{mn}} + \frac{3}{r_{mn}^2}\right)\right] \\
C_{mn} &= \frac{\partial^2 f}{\partial z^2} = \frac{e^{jkr_{nm}}}{r_{nm}}\left[\left(\frac{jk}{r_{mn}} - \frac{1}{r_{mn}^2}\right) + \frac{(z-z')^2}{r_{mn}^2}\left(-k^2 - \frac{3jk}{r_{mn}} + \frac{3}{r_{mn}^2}\right)\right] \\
r_m &= \sqrt{(x_m - x_n - x')^2 + (y_m - y_n - y')^2 + (z_m - z_n - z')^2} \\
r_{mn} &= \sqrt{(x_m - x_n)^2 + (y_m - y_n)^2 + (z_m - z_n)^2}
\end{aligned}$$

The exact image theory contains a term like $\int_0^\infty \frac{e^{jkR'}}{R'} e^{-p\xi} d\xi$ where R' is $\sqrt{(x-x')^2+(y-y')^2+(z+z'+j\xi)^2}$. Matrix element due to this integral is easily calculated using (6.11) and numerical integration with the respect to ξ as shown below:

$$\int_0^\infty \int_{v'} \frac{e^{jkR'}}{R'} e^{-p\xi} dv' d\xi \approx 4\Delta x\Delta y\Delta z \int_0^\infty \frac{e^{jkR_{mn}}}{R_{mn}} e^{-p\xi} d\xi + \frac{2}{3}\Delta x^3\Delta y\Delta z \int_0^\infty A'_{mn} e^{-p\xi} d\xi + \frac{2}{3}\Delta x\Delta y^3\Delta z \int_0^\infty B'_{mn} e^{-p\xi} d\xi + \frac{2}{3}\Delta x\Delta y\Delta z^3 \int_0^\infty C'_{mn} e^{-p\xi} d\xi$$

Here $R_{mn} = \sqrt{(x_m-x_n)^2+(y_m-y_n)^2+(z_m+z_n+j\xi)^2}$, and A'_{mn}, B'_{mn}, and C'_{mn} are similar to A_{mn}, B_{mn}, and C_{mn}, respectively in which r_{mn} is replaced with R_{mn}. Based on this formulation other elements are easily derived. For self-cell where $m = n$ the above expressions are not valid due to the singularity of the Green's function. Since cell size is very small compared to the wavelength, small argument expansion of the scalar Green's function can be used.

$$\begin{aligned}
\int_{v'} \frac{e^{jkr_m}}{r_m} dv' &\approx \int_{v'} \left(\frac{1}{r_m} + jk\right) dv' \approx 8\Delta y\Delta z \sinh^{-1}\frac{\Delta x}{\Delta y} - 2\pi(\Delta z)^2 + jk8\Delta xyz \\
\frac{\partial^2}{\partial x^2}\int_{v'} \frac{e^{jkr_m}}{r_m} dv' &\approx \left(4k^2(\Delta x)^2 - 8\right)\tan^{-1}\left(\frac{\Delta y\Delta z}{\Delta x\Delta_{xyz}}\right) - 4k^2\Delta x\Delta z \sinh^{-1}\frac{\Delta y}{\Delta_{xz}} + jk8\Delta xyz
\end{aligned}$$

where $\Delta_{opq} = \sqrt{\Delta o^2+\Delta p^2+\Delta q^2}$. Formulation for $\frac{\partial^2}{\partial y^2}\int_{v'} \frac{e^{jkr_m}}{r_m} dv'$, and $\frac{\partial^2}{\partial z^2}\int_{v'} \frac{e^{jkr_m}}{r_m} dv'$ are easily obtained by exchanging Δx with Δy, or Δz, respectively.

If there are several transmitters, an iterative solver such as conjugate gradient method (CG) may be inefficient and therefore direct inversion method can be used. Since building, or building wall are separated a more efficient approach may is derived, which reduce s the complexity of the method $O(N^3)$. Consider two distinct scatterers where matrix represen-

tation has the form

$$\mathbf{Z}\cdot\vec{V} = \begin{pmatrix} Z_{11} & Z_{12} \\ Z_{21} & Z_{22} \end{pmatrix} \begin{pmatrix} V_1 \\ V_2 \end{pmatrix} = \begin{pmatrix} I_1 \\ I_2 \end{pmatrix}$$

This equation can be solved analytically to find

$$V_1 = Z_{11}^{-1}(I_2 - Z_{12}V_2), \qquad V_2 = \left(Z_{22} - Z_{21}Z_{11}^{-1}Z_{12}\right)^{-1}\left(I_2 - Z_{21}Z_{11}^{-1}I_1\right)$$

This procedure contains two inversions of half-size matrices. Hence the asymptotic complexity is $\frac{1}{4}O(N^3)$ compared with the original complexity $O(N^3)$. This procedure can be followed in a successive manner by reducing each subdomain into small subdomains and so on.

6.6 Simulation Result for Cosite Interference

Figure 6.7 shows the configuration of a propagation scenario where there are three transmitters near a receiver inside a building and a base station 200m away. The location

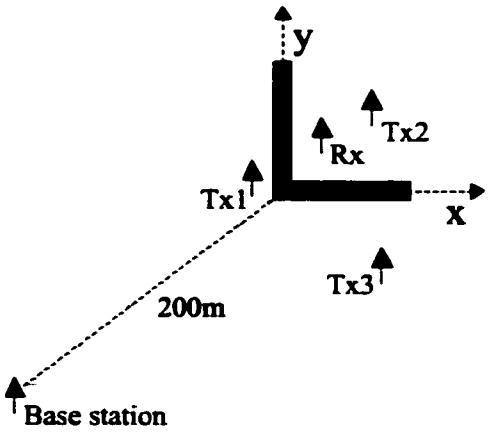

Figure 6.7: Simulation situation where base station is far away from the receiver and three transmitters are in proximity of the receiver. A big object block the LOS between the receiver and base station.

of the base station is chosen at (-180,-88,2), and interferers are at (-21,1,1), (21,7,1.3), and (20,-14,1.7), respectively. Also the receiver is located at (10,6,1). The building structure consists of two big walls perpendicular to each other that block the line-of-sight (LOS) between the base station and the receiver. All transmitters and base station are assumed to send the same power level through infinitesimal dipoles. The dielectric constant of the walls is assumed to be $4 + j0.3$, and the ground is modeled by an impedance surface whose normalized impedance is $0.3 - j0.1$. The right-angled corner consists of two identical walls whose length, height, and thickness are 18m, 12m, and 35cm, respectively. All transmitters operate at 50MHz (center frequency), and system bandwidth is chosen to be 4MHz. Data transmission rate is assumed 16.9k bps, and 63 chip per symbol Gold code is used for the PN code. Therefore a minimum bandwidth of 1.0647MHz ($= 63 \times 16.9k$) is occupied by the signal. This Gold code can be generated sequentially by combining two shift registers [38] that is designed by nth order (for this case 6th order) primitive polynomial [60]. For signaling method binary phase shift keying (BPSK) is used. Figure 6.8 shows block diagrams for the transmitter and receiver. To limit the bandwidth a bandpass filter (BPF) is

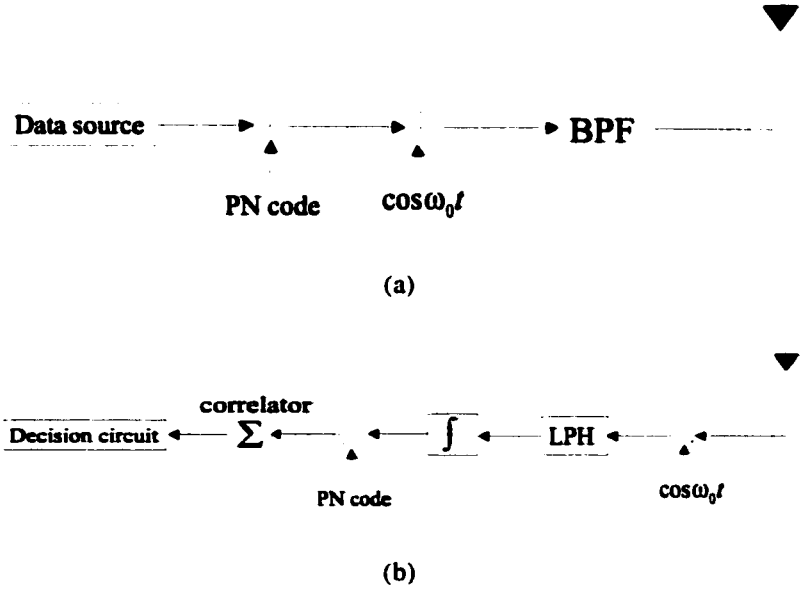

Figure 6.8: Block diagram of transmitter and receiver. (a) Transmitter (b) Receiver.

used at the transmitter, which is a second order Butterworth filter whose 3dB points are at 48.9353MHz, and 51.0647MHz, respectively.

The transmitters are assumed to send random bits. These signals reach the receiver attenuated and distorted by the scatterers. To demodulate the signal a coherent scheme is used, and synchronization is achieved by time shifting the received data to obtain maximum value. To calculate the received signal first the frequency response of the transmitted signal is calculated from its time domain response. Next the channel response is determined from the full-wave channel model in frequency domain. Then frequency responses of the channel and transmitted signals are multiplied and Fourier transformed back to time domain. Finally the time domain response of the received signal is passed though the correlator. Channel response in frequency domain for each transmitters are calculated every 1MHz from 48MHz to 52MHz. Figures 6.9 and 6.10 show the fields at the receiver as a function of frequencies. These show clearly that the signal from the base station is much lower than those from other near-by transmitters as expected. Figure 6.11 shows the low pass signal from the base station in time domain, which represents 63-bit of complete PN code. This is compared with an ideal PN code that is used in the base station where the level is adjusted for the mean pathloss in the channel. The distortion of the signal at the receiver is due to combined filter and channel response. In the next figure (Fig. 6.12) a probability density function (PDF) of output power of the correlator is plotted for each transmitters. These power levels are normalized by the power received from the base station. To obtain the PDF a Monte Carlo simulation is carried out where the codes of interferers are randomly changed. In this simulation 500 realizations are used. Since processing gain due to the PN code is just around 36dB ($20\log_{10}63$), it is obvious that the receiver can't restore the desired signal unless the power, the gain, and the base station antenna height are increased.

6.7 Conclusions

Multipole representation of the exact image theory is formulated, which is suitable for application of FMM algorithm to scattering problems in presence of an impedance surface. This formulation is very efficient and valid for the range where $\Re[p/k] > 1.2$ and $\Im[p/k] < 0.3$. In situations where $\Re[p/k] < 1.2$ and $\Im[p/k] > 0.3$ an alternative, but less computationally efficient multipole formulation is also derived using Gaussian quadrature method. These representations are verified by comparing the results with the direct numerical integration.

An efficient MoM formulation appropriate for objects on an impedance surface was also formulated using the exact image theory. This numerical tool was used to simulate cosite interference among a number of transmitters and a receiver for a DSCDMA. A simple environment was considered in which one base station is far away from the receiver, and three transmitters and an obstacle placed near the receiver. A 63-chip Gold code was used as the PN code, and a Monte Carlo simulation was carried out to calculate the PDF of the interfering signals at the receiver output. This PDF clearly shows that for a reliable communication the base station transmitter power, antenna gain, and/or antenna height must be increased.

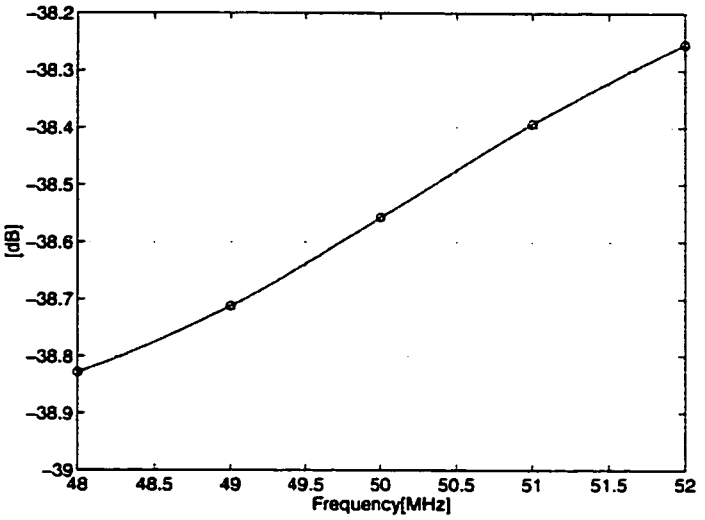

(a)

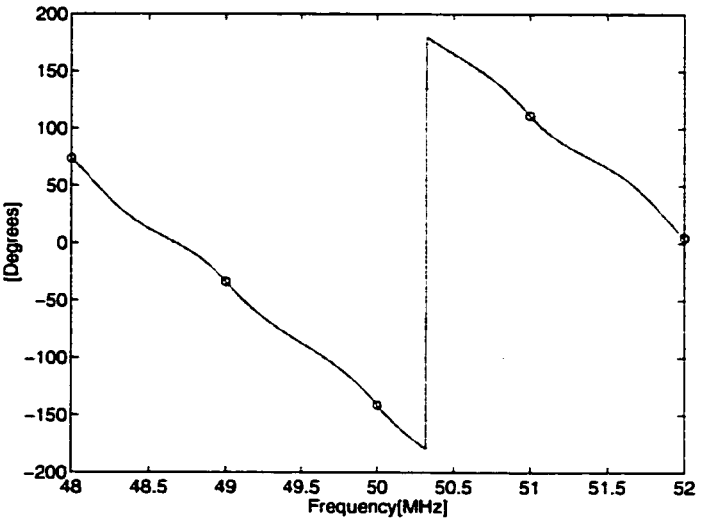

(b)

Figure 6.9: Channel response of base station at the receiver point. Field is calculated every 1MHz from 48MHz to 52MHz, and interpolated. (a) Magnitude (b) Phase.

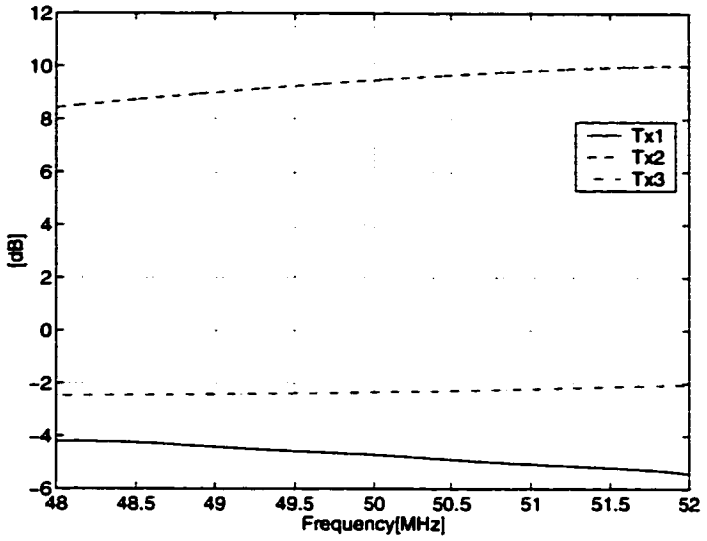

(a)

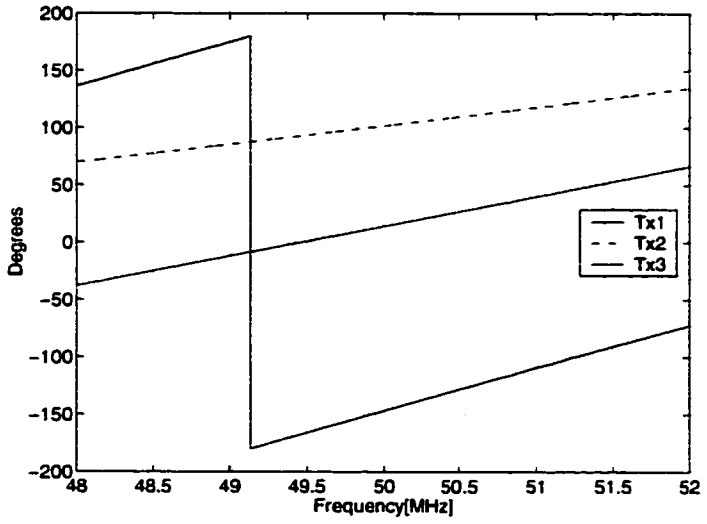

(b)

Figure 6.10: Channel response for transmitters in proximity of the receiver. Fields are calculated every 1MHz from 48MHz to 52MHz, and interpolated.

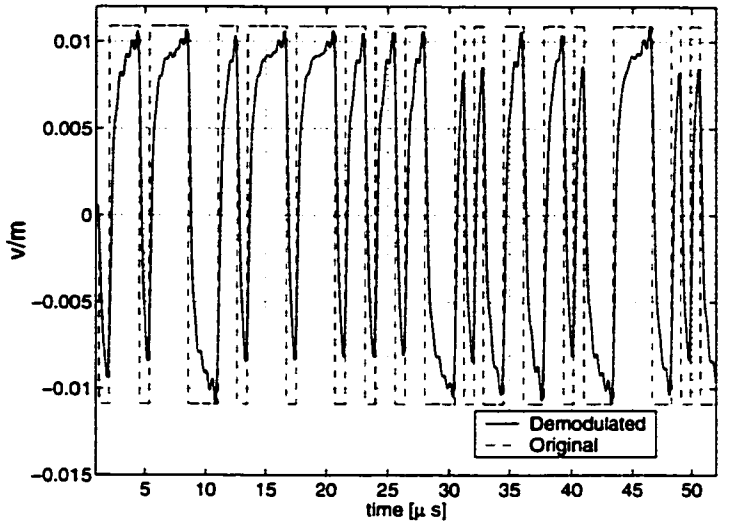

Figure 6.11: Plot of time domain signal from the base station. It is compared with the originally transmitted data. It shows one complete set of PN code.

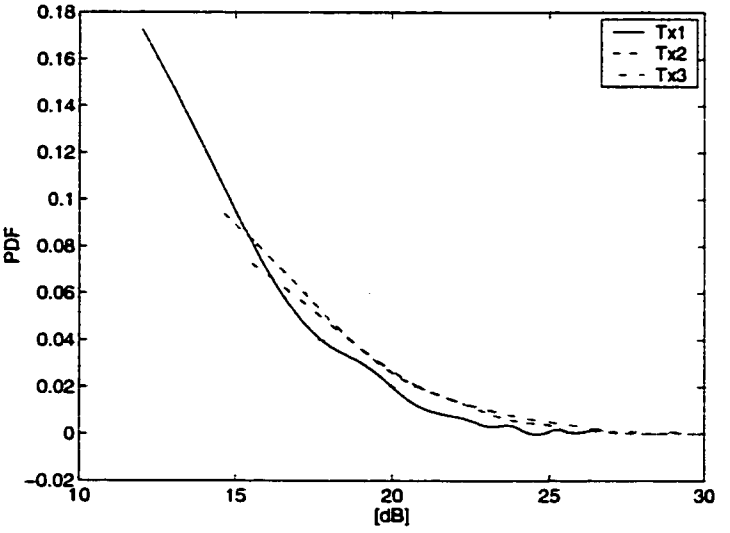

Figure 6.12: Probability density function (PDF) of output power of the correlator is plotted for each transmitters. The power is normalized by the power of the base station.

CHAPTER 7

Conclusions & Future Works

7.1 Conclusions

This thesis presented in depth investigation towards the development of a set of electromagnetic models suitable for the prediction of channel effects in wireless communication systems including both rural and urban environments. A physics-based methodology was applied in order to develop models that are both accurate and general, and provide an end to end simulation tool for the prediction of mean path-loss, field fluctuations and assessment of system peformance, for example various system modulation schemes. In Chapter 2 a model was developed to predict point-to-point propagation between two antennas embedded in a forest at HF through VHF frequencies. A three layer model, originally developed by Tamir [9] and which assumes a flat interface between air and tree canopy, was extended to account for the effects of a rough interface. The canopy roughness was assumed to have a Gaussian profile, and the distorted Born approximation was applied to obtain an analytical solution for the canopy with rough interface. An analytical solution that accounts for the effects of surface roughness was developed for the first time. The resulting formulation contains a partial second-order solution to account for the Brewster effect (Brewster angle). Results confirm that a lateral wave propagating along the canopy-air interface and shedding energy at critical angle is the dominant contributor to long distance transmission.

A sensitivity study in which dielectric constant, location of the dipoles, canopy roughness, etc. were varied, shows that even for moderate roughness the lateral wave is still the dominant contributor to long distance communication. In Chapter 3 this model for transmitter/receiver embedded in a forest environment was extended to account for the effect of the tree trunks, the main cause of field fluctuations. The tree trunk is modeled as a circular dielectric cylinder. These cylinders are embedded inside the canopy layer. Interactions among the tree trunks are calculated using conventional MoM. To reduce computational complexity three schemes were used. The first is the decomposition of the MoM matrix into several small matrices, which reduces the required memory size for storage of the matrix. The second is an introduction of a statistical equivalent model. It was shown that except for a small number of trees in the proximity of the transmitter and receiver the remaining trunks could be replaced with an equivalent dielectric medium, while still retaining the statistical fluctuations of the received field in an accurate fashion. Hence this method reduces significantly the total number of cylinders needed, and eventually the memory and speed required for calculation. The computational complexity of the problem was farther reduced by application of reciprocity. Since the receiver in general is far away from the transmitter, the incident wave on tree trunks around the receiver can be approximated locally by a plane wave. Reciprocity allows after interchange of the source and receiver the polarization currents inside these finite cylinders can be approximated by those of infinite cylinders. This procedure reduced the size of the final MoM matrix significantly. The effects of ground reflection of the fields scattered from the cylinders are also included in the model. As with all the models in this thesis desired statistics can be generated by using a Monte Carlo simulation. Applying this model, performance of a single antenna and also of antenna arrays were assessed. Basic statistics such as spatial correlation were calculated. In order to efficiently convert the wide-band frequency response to time-domain response, a non-uniform sampling scheme based on Gaussian quadrature was implemented. Applying this scheme the required sampling points to avoid aliasing was reduced from over 340

points for regular FFT to 40 points. In Chapter 4 a model for air-to-ground communications in a rural environment was introduced. This model is based on a fractal tree model which provides a detailed description of natural trees, and the application of single scattering theory. An analytic solution was first derived for scattering from a finite cylinder based on the assumption that the surface currents on a finite cylinder with large length to diameter ratio, are the same as those on an infinite one whose radius and dielectric constant are the same as those of the finite one. This formulation is valid for both near- and far-field regions. To include the effect of the ground, 4 G.O. components are included in the final solution. Using this model the performance of GPS systems under two types of forests, coniferous and deciduous, were assessed as a function of the location of the GPS satellites (incident angle). The ultra-wide band characteristics of coniferous forest channel also investigated.

In Chapter 5 a new modulation scheme was proposed for ultra-wide band communications. This scheme divides the required frequency band into many sub-bands proportional to frequency. This is different from the conventional OFDM. The output of a set of BPFs are directly used as carriers for each sub-band, which form a set of orthogonal waveforms in both time- and frequency-domain. This scheme allows data categorization according to a specific hierarchy. Performance of this system was assessed based on the model for transmitter and receiver in a forest, developed in Chapter 3, and compared with that of an impulse radio modulation scheme. Two situations were considered. The first is that of transmitter distant from any trees, and the second is that of the transmitter in close proximity to a tree so that the direct field is distorted severely by the scattered field from the near-by tree. The new hierarchical scheme showed significantly improved results over that of the impulse radio scheme.

In Chapter 6 a FMM formulation was implemented using an exact image formulation as a Green's function. An original exact image formulation for a small dipole radiating above an impedance half-space was simplified to a compact form, which separates P.E.C. image terms from the perturbed field caused by the impedance surface in Appendix D. Simulation

of cosite interference for a DSCDMA (Direct Sequence CDMA) system also was carried out for a simple environment in which a base station is located far away from transmitters and receiver. A large scatterer blocks the LOS between the base station and the receiver, and the transmitters are located in proximity of the receiver. Characteristics of the channel were calculated by MoM based on the exact image theory because the operating frequency is so low that the penetrating field through the scatterer is very important. This is a scenario which in an accurate fashion can't be dealt with by the ray-tracing techniques. Using Monte Carlo simulation the output powers of the correlator of the receiver were computed for the base station and the other transmitters.

7.2 Future Work

The prediction of radio wave propagation is an ongoing effort with the eventual goal of an end to end tool for accurate, general and efficient channel characterization and channel effects on a communication system. With this in mind there are several interesting research issues which are an outgrowth of this thesis work.

1. **Inclusion of Field Fluctuation Caused by Canopy Roughness.**

   In chapter 2 a formulation was developed for calculating the effect of interface canopy on propagation. This formulation accounted for the effect of the forest and used a first order distorted Born approximation to account for canopy roughness in a mean sense. A proposed extension of this model is to one which includes the statistical variation in the received fields caused by the canopy roughness. This investigation would include determining the correlation between two points on the rough surface as well as investigating the appropriate pdf's for the canopy roughness. Basically the second moments of the field component at the receiver point should be evaluated.

2. **Extension of Forest Model to the Case of Transmitter and Receiver in Close Proximity.**

In Chapter 3 a complete model was developed to predict stochastic behavior of a forest channel for the ground-to-ground communications based on MoM, reciprocity, and Monte Carlo simulation. This model is valid only for long distance communication. However to access performance of cosite interference for DSCDMA a channel model for the case of a transmitter and a receiver in close proximity is required.Therefore an extension of the developed model is proposed. Additionally the model assumes a flat boundary between the air and canopy interface, and hence the rough interface model that was developed in Chapter 2 should be included as an extension to the existing model.

3. **Extension of Forest Model for Air-to-Ground Communication in a Rural Environment**

   In Chapter 4 a model was developed based on a fractal tree model and single scattering theory. In addition an analytical formulation for scattering from each component of a tree structure was derived. This model is valid theoretically for any frequency band, but as frequency increases the exact solution for cylinder used in this model very rapidly becomes inefficient. For higher frequencies an alternative approach is needed, such as PO. An other important issue is related to the accuracy of single scattering theory at high frequency. Single scattering theory dose not account for the interaction between leaves and needles in clusters. These clusters are packed so densely that the interactions cannot be ignored. Therefore a method to account for these higher order interactions is proposed. However it is noted that the computation time will drastically be increased if second order effects need be accounted for.

4. **Model for Urban Environments**

   In Chapter 6 an FMM identity was formulated based on exact image theory. Hence implementation of an FMM type solver for scattering problems of objects above and on an impedance surface can clearly be an additional next research topic. Another

important issue is a development of an efficient model which combines the formulated MoM in this work and other techniques like the ray-tracing.

Additionally to enhance the accuracy of the proposed models realistic features should be included, such as the roughness of the ground plane. Integrating of the developed rural and urban models is also an important issue, in addition to effects such as the effect of roadside trees in an urban area. It is recommended that the developed models be extended to include new scenarios like:

1. **A Discontinuous Forest**

   This model would include the scenarios of one terminal outside a forest, and near the ground, and another inside. The forest may be split by roads, streams, and so on.

2. **Trees on Hilly Surface**

   In this thesis work the forest model is only for a flat ground. An interesting problem is one in which a forest is placed on a convex or concave surface such as a hill. Another important topic is the effect that trees on the top of a hill have wave propagation when either of transmitter or receiver are beyond the hill.

APPENDICES

Appendix A

Calculation of Scattered Field from a Finite Cylinder Using 2D MoM Currents

As mentioned previously in Chapter 3 for solutions where a receiver or a transmitter is in close proximity of a tree canopy, near-field effects of large tree scatterers, such as tree trunks must be accounted for. In modeling forest scatterers at lower frequencies tree trunks are modeled by strait dielectric cylinders. In this appendix an efficient formulation, valid for near-field to far-field regions, for the calculation of scattered fields from dielectric cylinders is provided. With the help of the Hertz potential, electric field can be easily computed from a known current distribution, $\vec{\mathbf{J}}$, using $\vec{\mathbf{E}} = \nabla(\nabla \cdot \vec{\Pi}_e) + k_1^2 \vec{\Pi}_e$. The electrical Hertz vector is represented by

$$\vec{\Pi}_e = -\sum_n \frac{1}{4\pi j\omega\epsilon} \int_{v'} \vec{\mathbf{J}}_n e^{-jk_{z'}^l z'} \frac{e^{jk|\vec{r}-\vec{r}'|}}{|\vec{r}-\vec{r}'|} dv' \tag{A.1}$$

The integral in (A.1) can be evaluated in an approximate fashion if we assume the vector current $\vec{\mathbf{J}}_n$ is constant across an small (MoM) cell whose dimensions are much smaller than a wavelength. Let $I = \int_{s_n'} \frac{e^{jk|\vec{r}-\vec{r}'|}}{|\vec{r}-\vec{r}'|} e^{-jk_{z'}^l z'} dx'dy'$. where s_n' is a cell area. For small pixel area

and using mid-point integration

$$I \approx \triangle^2 \frac{e^{jkr_n}}{r_n}$$

where $r_n = \sqrt{(x-x_n)^2+(y-y_n)^2+(z-z')^2}$. Based on this, all terms of $\vec{\mathbf{E}}$ can be evaluated in an analytic fashion. To calculate $\vec{\mathbf{E}}$ the following terms are needed.

$$\begin{aligned}
I_{xx} &= \frac{\partial^2}{\partial x^2} I \approx \triangle^2 \frac{e^{jkr_n}}{r_n}(jkr_n - 1)\left[\frac{1}{r_n} - \frac{3\cos^2\theta_n}{r_n} + jk\cos^2\theta_n\right] \\
I_{yy} &= \frac{\partial^2}{\partial y^2} I \approx \triangle^2 \frac{e^{jkr_n}}{r_n}(jkr_n - 1)\left[\frac{1}{r_n} - \frac{3\sin^2\theta_n}{r_n} + jk\sin^2\theta_n\right] \\
I_{zz} &= \frac{\partial^2}{\partial z^2} I \approx \triangle^2 \frac{e^{jkr_n}}{r_n}(jkr_n - 1)\left[\frac{1}{r_n} - \frac{3\cos^2\theta_n}{r_n} + jk\cos^2\theta_n\right] \\
I_u &= \frac{\partial}{\partial u} I \approx \triangle^2 \frac{jkr_n - 1}{r_n^2} e^{jkr_n} \begin{cases} \cos\theta_n & u = x \\ \sin\theta_n & u = y \end{cases}
\end{aligned}$$

The remaining components of $\vec{\mathbf{E}}$ can be evaluated using

$$\begin{aligned}
I_{xy} &= \triangle^2 \left[\frac{e^{jkr_n^{--}}}{r_n^{--}} - \frac{e^{jkr_n^{-+}}}{r_n^{-+}} - \frac{e^{jkr_n^{+-}}}{r_n^{+-}} + \frac{e^{jkr_n^{++}}}{r_n^{++}}\right] \\
\int_0^L I_{xz} dz' &= \frac{\partial^2}{\partial x \partial z}\int_0^L I dz' = I'_{xz} - jk'_z \int_0^L \left(\triangle^2 \cos\theta_n \frac{e^{jkr_n}}{r_n^2}(jkr_n - 1)\right) e^{-jk'_z z'} dz' \\
\int_0^L I_{yz} dz' &= \frac{\partial^2}{\partial y \partial z}\int_0^L I dz' = I'_{yz} - jk'_z \int_0^L \left(\triangle^2 \sin\theta_n \frac{e^{jkr_n}}{r_n^2}(jkr_n - 1)\right) e^{-jk'_z z'} dz'
\end{aligned}$$

where

$$
\begin{aligned}
I'_{xz} &= \triangle^2 \frac{e^{jkr_{n0}}}{r_{n0}}(jkr_{n0}-1)\cos\theta_{n0} - \triangle^2 \frac{e^{jkr_{nl}}}{r_{nll}}(jkr_{nl}-1)\cos\theta_{nl}e^{-jk'_z L} \\
I'_{yz} &= \triangle^2 \frac{e^{jkr_{n0}}}{r_{n0}}(jkr_{n0}-1)\cos\theta_{n0} - \triangle^2 \frac{e^{jkr_{nl}}}{r_{nll}}(jkr_{nl}-1)\cos\theta_{nl}e^{-jk'_z L} \\
r_n^{\pm\pm} &= \sqrt{(x-x_n \pm \triangle/2)^2 + (y-y_n \pm \triangle/2)^2 + (z-z')^2} \\
r_{n0} &= \sqrt{(x-x_n)^2 + (y-y_n)^2 + z^2} \\
r_{nl} &= \sqrt{(x-x_n)^2 + (y-y_n)^2 + (z-L)^2} \\
\cos\theta_{n0} &= z/r_{n0}, \quad \cos\theta_{nl} = (z-L)/r_{n0}
\end{aligned}
$$

Therefore the final expression for the electrical, $\vec{\mathbf{E}}$ field that includes the effect of ground reflection is given by

$$
\begin{aligned}
\vec{\mathbf{E}} \approx -\frac{1}{4\pi jw\varepsilon}\sum_n \int_0^L [\, & \{(R_h+1)(I_{xx}+k_1^2 I)l_x + (R_h+1)I_{xy}l_y + (R_v+1)I_{xz}l_z\}\hat{x} + \\
& \{(R_h+1)I_{xy}l_x + (R_h+1)(I_{yy}+k_1^2 I)l_y + (R_v+1)I_{yz}l_z\}\hat{y} + \\
& \{(R_h+1)I_{xz}l_x + (R_h+1)I_{yz}l_y + (R_v+1)(I_{zz}+k_1^2 I)l_z\} + \\
& \hat{R}_h(I_{xz}\hat{x} + I_{yz}\hat{y} + I_{zz}\hat{z})(\cos\varphi l_x + \sin\varphi l_y)]\, dz'
\end{aligned}
\tag{A.2}
$$

where L is lenght of cylinder, the summation is over all cells in all cylinders and R_h, and R_v are the ground Fresnel reflection coefficient and also $\hat{R}_h = \sin 2\theta \frac{\cos\theta - \sqrt{\kappa - \sin^2\theta}}{\kappa\cos\theta + \sqrt{\kappa - \sin^2\theta}}$ [61].

Appendix B

Low Frequency Scattering from a Circular Cylinder

In order to improve the computation time of scattered field calculation in a forested environment using Monte Carlo simulations, scattering models should be computationally as efficient as possible. Analytical formulations in these regard are very attractive. In this appendix scattering from a very thin circular cylinder is formulated based on the volumetric integral equation. If the radius of a cylinder is small ($|\varepsilon_r a| << 1$), the polarization current inside the cylinder can be approximated by a constant vector. Therefore from equation (3.2) the polarization current can be written as

$$\vec{\mathbf{J}} \approx -jk_0 Y_0(\varepsilon_r - 1)\left[1 - (\varepsilon_r - 1)\int_{s'} \bar{\bar{G}}(|\vec{\rho} - \vec{\rho}'|)ds'\right]^{-1} \cdot \vec{\mathbf{E}}^i \tag{B.1}$$

$$= -jk_0 Y_0(\varepsilon_r - 1)\begin{bmatrix} P_{xx} & P_{xy} & P_{xz} \\ P_{yx} & P_{yy} & P_{yz} \\ P_{zx} & P_{zy} & P_{zz} \end{bmatrix} \vec{\mathbf{E}}^i = -jk_0 Y_0(\varepsilon_r - 1)\bar{\bar{\mathbf{P}}} \cdot \vec{\mathbf{E}}^i \tag{B.2}$$

$\bar{\bar{G}}$ is defined in (3.3). Analytically to evaluate the integral in (B.1) $H_0^{(1)}(k_\rho|\vec{\rho} - \vec{\rho}'|)$ is expanded by the addition theorem [31], and after analytically evaluating the double integral

with the respect to ϕ the integral is reduced to

$$\int_0^{2\pi}\int_0^a H_0^{(1)}(k_\rho|\vec{\rho}-\vec{\rho}'|)\rho' d\rho' d\phi' = \int_0^\rho H_0^{(1)}(k_\rho\rho)J_0(k_\rho\rho')\rho' d\rho' + \int_\rho^a H_0^{(1)}(k_\rho\rho')J_0(k_\rho\rho)\rho' d\rho' \tag{B.3}$$

Using the integral identity, $\int_0^z t^\nu J_{\nu-1}(t)dt = z^\nu J_\nu(z)$ [62], the integrals in (B.3) are evaluated and expressed as

$$\begin{aligned}\int_0^\rho J_0(k_\rho\rho')\rho' d\rho' &= \frac{\rho}{k_\rho}J_1(k_\rho\rho)\\ \int_\rho^a H_0^{(1)}(k_\rho\rho')\rho' d\rho' &= \frac{a}{k_\rho}H_1^{(1)}(k_\rho a) - \frac{\rho}{k_\rho}H_1^{(1)}(k_\rho\rho)\end{aligned}$$

Using the above results, applying the Wronskians and small argument expansion of the Bessel function ($J_0(k_\rho\rho)\approx 1$)

$$\begin{aligned}\int_0^{2\pi}\int_0^a H_0^{(1)}(k_\rho|\vec{\rho}-\vec{\rho}'|)\rho' d\rho' d\phi' &= j\frac{4}{k_\rho^2} + \frac{2\pi a}{k_\rho}J_0(k_\rho\rho)H_1^{(1)}(k_\rho a)\\ &\approx j\frac{4}{k_\rho^2} + \frac{2\pi a}{k_\rho}H_1^{(1)}(k_\rho a)\end{aligned} \tag{B.4}$$

Based on (B.4) derivatives of the integral that appear in (3.3) can be easily carried out. For example the term, $\frac{\partial^2}{\partial x^2}\int_0^{2\pi}\int_0^a H_0^{(1)}(k_\rho|\vec{\rho}-\vec{\rho}'|)\rho' d\rho' d\phi'$ can be computed using the following equation;

$$\frac{\partial^2}{\partial x^2}J_0(k_\rho\rho) = -k_\rho^2\cos^2\phi J_0(k_\rho\rho) + \frac{k_\rho}{\rho}(\cos^2\phi - \sin^2\phi)J_1(k_\rho\rho) \sim -\frac{k_\rho^2}{2}$$

Following a similar procedure for other derivatives the components of polarizability tensor are obtained, and are given by

$$\begin{aligned} P_{xx} &= P_{yy} = \frac{1}{1-\frac{j}{4}(\varepsilon_r-1)\left[j\frac{4}{\sin^2\theta}+\frac{2\pi k_\rho a}{\sin^2\theta}H_1^{(1)}(k_\rho\rho)-\pi k_\rho a H_1^{(1)}(k_\rho\rho)\right]} \\ P_{zz} &= \frac{1}{1-\frac{j}{4}(\varepsilon_r-1)\left[j4+2\pi k_\rho a H_1^{(1)}(k_\rho a)\right]} \\ P_{xy} &= P_{yx} = P_{xz} = P_{yz} = P_{zx} = P_{zy} = 0 \end{aligned}$$

Using the small argument expansion of the Hankel function, $H_1^{(1)}(k_\rho a) \sim -j\frac{2}{\pi k_\rho a}$, the polarizability tensor can be reduced to the more familiar form [18] as

$$P_{xx} = P_{yy} = \frac{2}{\varepsilon_r+1}, \quad P_{zz} = 1$$

For the far-field region, the scattered field from a very thin finite cylinder is easily calculated based on the resulting polarizability tensor, and can be written as

$$\vec{\mathbf{E}}^s \sim -\frac{e^{ik_0 r}}{4\pi r}\pi(k_0 a)^2 l \ \text{sinc}\left[\frac{(\hat{k}^i+\hat{k}^s)\cdot\hat{l}}{2}\right]\left[\hat{k}_s(\hat{k}_s\cdot\vec{P})-\vec{P}\right]$$

where l is the length of the cylinder, $\hat{k}_s$ is a unit vector between the center position of the cylinder and the observation, $k_z^s = \vec{k}_s\cdot\hat{z}$, $\vec{P}$ is defined as $P_{xx}\hat{x}+P_{yy}\hat{y}+P_{zz}\hat{z}$, and $\text{sinc}(z) = \frac{\sin z}{z}$.

Appendix C

Scattering from a Thin Dielectric Disk

In Chapter 4 a model for characterizing wave propagation through foliage was described. In this model flat leaves are presented by thin dielectric disks. At low frequencies Rayleigh-Gans approximation is used for the calculation of scattered field. At higher frequencies where typical dimensions of this leaf are comparable to or larger than a wavelength the low-frequency model fails. In this appendix high frequency scattering from a thin dielectric disk is considered. Here it is assumed that one dimension (the z-dimension as seen in Figure C.1) of the disk is thin compared to the wavelength, and the other two dimensions are comparable to or larger than a wavelength. The polarization current inside the finite dielectric slab can be approximated by that of an infinite slab whose dielectric constant and thickness are the same as those of the finite one, if the dielectric is loss enough. The polarization current inside the slab can be expressed by equation (B.2). Total fields in-

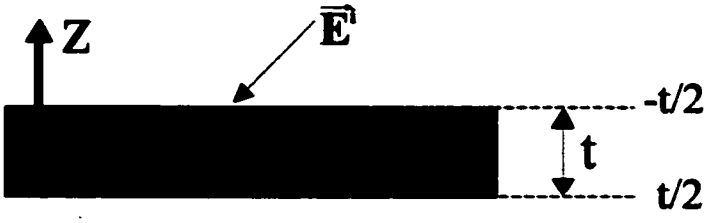

Figure C.1: Infinite dielectric slab.

side the slab can be analytically computed and are given in [19, 18]. From this total field the polarization current can be obtained using $\vec{\mathbf{J}} = -jk_0 Y_0(\varepsilon_r - 1)\vec{\mathbf{E}}^t$ which in turn can be used to find the far-field expression. These currents are known as volumetric integral physical optic (VIPO) currents [18]. It turns out that the far-field expression for the scattered field from an elliptical disk whose major and minor axis are denoted as a and b, respectively, is given by: [49, 63]

$$\vec{\mathbf{E}} \sim -\frac{e^{jk_0 r}}{r}\frac{k_0^2}{4\pi}\hat{k}_s \times \hat{k}_s \times (\bar{\bar{\mathbf{P}}} \cdot \vec{\mathbf{E}}^i)\frac{2A_d J_1\left(\sqrt{(aA)^2+(bB)^2}\right)}{\sqrt{(aA)^2+(bB)^2}}$$

where A_d is the area of the disk, $A = k_0(\hat{k}_i - \hat{k}_s)\cdot\hat{x}$, and $B = k_0(\hat{k}_i - \hat{k}_s)\cdot\hat{y}$. $\bar{\bar{\mathbf{P}}}$ here is similar to the polarizability tensor in the Rayleigh-Gans solution, however, it does not have physical definition. The elements of tensor ($\bar{\bar{\mathbf{P}}}$) can easily be obtained and for an h-polarized incident wave are given by

$$\begin{aligned} P_{xx} &= P_{yy} = \frac{2tk_z}{\triangle}\left[(k_z + k_z')e^{-jk_z' t/2} - (k_z - k_z')e^{jk_z' 3t/2}\right]e^{-jk_z t/2} \\ P_{xy} &= P_{yx} = P_{xz} = P_{yz} = P_{zx} = P_{zy} = 0 \end{aligned}$$

where $\triangle = (k_z + k_z')^2 - (k_z - k_z')^2 e^{j2k_z' t}$, and $k_z'^2 = \varepsilon_r k_0^2 - k_x^2 - k_y^2$. P_{zz} is defined arbitrarily because the z-directed component of the incident wave is zero. For a v-polarized incident wave,

$$\begin{aligned} P_{xx} &= P_{yy} = \frac{2tk_z'}{\triangle}\left[(\varepsilon_r k_z + k_z')e^{-jk_z' t/2} - (\varepsilon_r k_z - k_z')e^{jk_z' 3t/2}\right]e^{-jk_z t/2} \\ P_{zz} &= \frac{2tk_z}{\triangle}\left[(\varepsilon_r k_z + k_z')e^{-jk_z' t/2} - (\varepsilon_r k_z - k_z')e^{jk_z' 3t/2}\right]e^{-jk_z t/2} \end{aligned}$$

where $\triangle = (\varepsilon_r k_z + k_z')^2 - (\varepsilon_r k_z - k_z')^2 e^{j2k_z' t}$. If the thickness ($t$) approaches zero the resulting currents reduce to the well-known Rayleigh-Gans PO current which is expressed as

$$P_{xx} = P_{yy} = t, \quad P_{zz} = t/\varepsilon_r$$

Figure C.2 shows an examination of the accuracy of the VIPO and Rayleigh-Gans PO by comparison with MoM result. For this comparison S_{hh} is calculated for forward scattering with a normal incident wave from a circular disk whose radius is a, thickness 0.02cm, and dielectric constant $27.6 + i11.54$. As seen in the figure the Rayleigh-Gans PO becomes inaccurate as $k_0 a$ increases while VIPO still gives an accurate result.

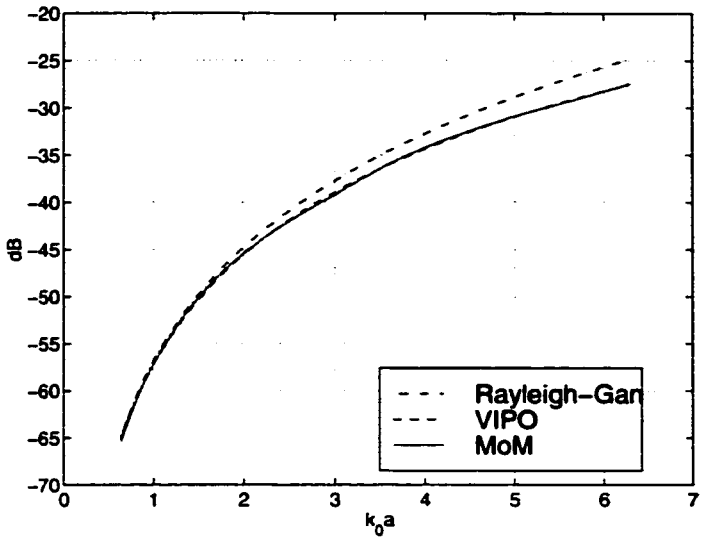

(a)

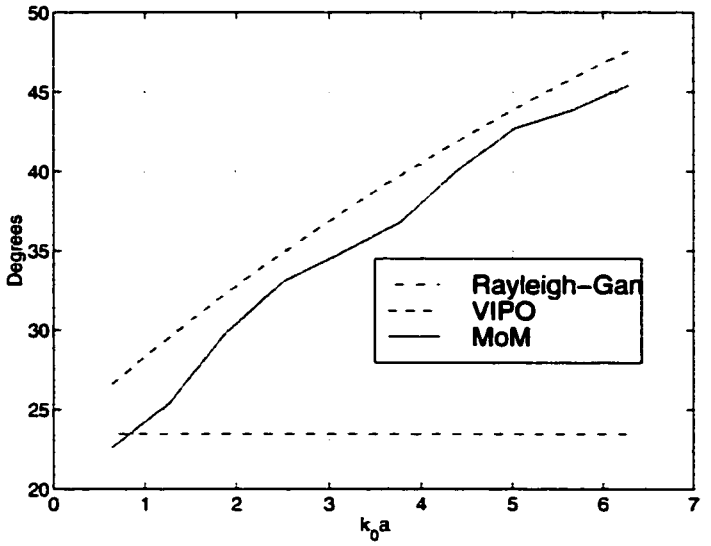

(b)

Figure C.2: Comparison of forward scattering from a circular disk calculated by Rayleigh-Gans PO and VIPO with results from a MoM formulation as a function of k_0a. (a) Magnitude (b) Phase

Appendix D

Simplification of the Exact Image Formulation

In this appendix the original exact image formualtion is simplified to a more compact form. If a vertical infinitesimal dipole is located at (x',y',z') above an impedance surface whose normalized impedance is η. Diffracted field is represented as [52]

$$\mathbf{E}_v^d(\mathbf{r},\mathbf{r}') = \frac{jZ_0 I}{4\pi k}\, l_z \left\{ \frac{\partial^2}{\partial x \partial z}\hat{x} + \frac{\partial^2}{\partial y \partial z}\hat{y} - \left(\frac{\partial^2}{\partial x^2} + \frac{\partial^2}{\partial y^2} \right)\hat{z} \right\} \left[\frac{e^{jkR}}{R} - 2\beta \int_0^\infty e^{-\beta\xi} \frac{e^{jkR'(\xi)}}{R'(\xi)}\, d\xi \right] \tag{D.1}$$

For a horizontal dipole the expresseion is more complex, and the x-component of the diffracted field is written as

$$\begin{aligned} \mathbf{E}_h^d(\mathbf{r},\mathbf{r}')\cdot\hat{x} = jkZ_0 I \Bigg\{ & l_x \left(\frac{\partial^2}{\partial x^2} + \frac{\partial^2}{\partial y^2} \right) \int_0^\infty \left[\frac{1-\eta}{2k(1+\eta)} \frac{e^{jkR''(\xi)}}{4\pi R''(\xi)} + \frac{1+\eta}{2k(1-\eta)} \frac{e^{jkR'(\xi)}}{4\pi R'(\xi)} \right] e^{-k\xi} d\xi - \\ & l_x \frac{2\eta}{k(1-\eta^2)} \int_0^\infty \left[e^{-\alpha\xi} \frac{\partial^2}{\partial y^2} \frac{e^{jkR'(\xi)}}{4\pi R'(\xi)} + e^{-\beta\xi} \frac{\partial^2}{\partial x^2} \frac{e^{jkR'(\xi)}}{4\pi R'(\xi)} \right] d\xi - \\ & \frac{1}{k^2} \left(l_x \frac{\partial^2}{\partial x^2} + l_y \frac{\partial^2}{\partial x \partial y} \right) \left[\frac{e^{jkR}}{4\pi R} - 2k\eta \int_0^\infty e^{-\beta\xi} \frac{e^{jkR'(\xi)}}{4\pi R'(\xi)}\, d\xi \right] + \\ & l_y \frac{\partial^2}{\partial x \partial y} \left(\frac{2\eta}{k(1-\eta^2)} \right) \int_0^\infty (e^{-\alpha\xi} - e^{-\beta\xi}) \frac{e^{jkR'(\xi)}}{4\pi R'(\xi)}\, d\xi \Bigg\}, \end{aligned} \tag{D.2}$$

the y-component is expressed as

$$\mathbf{E}_h^d(\mathbf{r},\mathbf{r}')\cdot\hat{y}=jkZ_0I\Bigg\{l_y\left(\frac{\partial^2}{\partial x^2}+\frac{\partial^2}{\partial y^2}\right)\int_0^\infty\left[\frac{1-\eta}{2k(1+\eta)}\frac{e^{jkR''(\xi)}}{4\pi R''(\xi)}+\frac{1+\eta}{2k(1-\eta)}\frac{e^{jkR'(\xi)}}{4\pi R'(\xi)}\right]e^{-k\xi}d\xi-$$
$$l_y\frac{2\eta}{k(1-\eta^2)}\int_0^\infty\left[e^{-\alpha\xi}\frac{\partial^2}{\partial x^2}\frac{e^{jkR'(\xi)}}{4\pi R'(\xi)}+e^{-\beta\xi}\frac{\partial^2}{\partial y^2}\frac{e^{jkR'(\xi)}}{4\pi R'(\xi)}\right]d\xi-$$
$$\frac{1}{k^2}\left(l_y\frac{\partial^2}{\partial y^2}+l_x\frac{\partial^2}{\partial x\partial y}\right)\left[\frac{e^{jkR}}{4\pi R}-2k\eta\int_0^\infty e^{-\beta\xi}\frac{e^{jkR'(\xi)}}{4\pi R'(\xi)}d\xi\right]+$$
$$l_x\frac{\partial^2}{\partial x\partial y}\left(\frac{2\eta}{k(1-\eta^2)}\right)\int_0^\infty(e^{-\alpha\xi}-e^{-\beta\xi})\frac{e^{jkR'(\xi)}}{4\pi R'(\xi)}d\xi\Bigg\}, \tag{D.3}$$

and finally the z-component is given by

$$\mathbf{E}_h^d(\mathbf{r},\mathbf{r}')\cdot\hat{z}=-jkZ_0I\left\{\frac{1}{k^2}\left(l_x\frac{\partial^2}{\partial x\partial z}+l_y\frac{\partial^2}{\partial y\partial z}\right)\left[\frac{e^{jkR}}{4\pi R}-2\beta\int_0^\infty e^{-\beta\xi}\frac{e^{jkR'(\xi)}}{4\pi R'(\xi)}d\xi\right]\right\} \tag{D.4}$$

where $R''(\xi)=\sqrt{(x-x')^2+(y-y')^2+(z+z'-j\xi)^2}$, and other quantities are defined in Chapter 6.

To explain the peculiar behavior of the exponentially diverging image current for a horizontal dipole an alternative representation is derived. It is shown that the exponentially diverging image current represents the contribution from the mirror image (or perfect conductor) which can be extracted. The exact image formulation can be further simplified by observing the behavior of the x component of the electric field expressions for the perfect electric conducting (PEC) case, ($\eta=0$). For the PEC case (D.1), and (D.2) reduce to

$$\mathbf{E}^d(\mathbf{r},\mathbf{r}')\cdot\hat{x}=\frac{jZ_0I}{k}\left[-l_x\frac{\partial^2}{\partial x^2}-l_y\frac{\partial^2}{\partial x\partial y}+l_z\frac{\partial^2}{\partial x\partial z}\right]\frac{e^{jkR}}{4\pi R}+$$
$$\frac{jZ_0I}{2}l_x\left(\frac{\partial^2}{\partial x^2}+\frac{\partial^2}{\partial y^2}\right)\int_0^\infty e^{-k\xi}\left[\frac{e^{jkR''}}{4\pi R''}+\frac{e^{jkR'}}{4\pi R'}\right]d\xi \tag{D.5}$$

According to image theory [34], this diffracted field component should be equal to the x

component of the electric field radiated from an image dipole, given by

$$\mathbf{E}^{is}(\mathbf{r},\mathbf{r}')\cdot\hat{x}=\frac{jZ_0I}{k}\left[-l_x\left(k^2+\frac{\partial^2}{\partial x^2}\right)-l_y\frac{\partial^2}{\partial x\partial y}+l_z\frac{\partial^2}{\partial x\partial z}\right]\frac{e^{jkR}}{4\pi R}, \tag{D.6}$$

where the superscript *is* implies image source. Setting (D.5) equal to (D.6) the following relationship is obtained,

$$\left(\frac{\partial^2}{\partial x^2}+\frac{\partial^2}{\partial y^2}\right)\int_0^\infty e^{-k\xi}\frac{e^{jkR''}}{4\pi R''}d\xi=-2k\frac{e^{jkR}}{4\pi R}-\left(\frac{\partial^2}{\partial x^2}+\frac{\partial^2}{\partial y^2}\right)\int_0^\infty\frac{e^{jkR'}}{4\pi R'}e^{-k\xi}d\xi \tag{D.7}$$

Applying (D.7), and after some algebraic manipulation the expressions for diffracted fields (equations (D.1), (D.2), (D.3), and (D.4)) can be rewritten in a more compact form as

$$\begin{aligned}\mathbf{E}^d(\mathbf{r},\mathbf{r}')=&\mathbf{E}^{is}(\mathbf{r},\mathbf{r}')+\mathbf{E}^{es}(\mathbf{r},\mathbf{r}')+\frac{2jkZ_0I\eta}{1-\eta^2}\Big[l_x\hat{x}\cdot\\&\left\{\frac{\partial^2}{\partial x^2}\int_0^\infty(e^{-k\xi}-\eta^2e^{-\beta\xi})\frac{e^{jkR'}}{4\pi R'}d\xi+\frac{\partial^2}{\partial y^2}\int_0^\infty(e^{-k\xi}-e^{-\alpha\xi})\frac{e^{jkR'}}{4\pi R'}d\xi\right\}+\\&l_y\hat{y}\left\{\frac{\partial^2}{\partial x^2}\int_0^\infty(e^{-k\xi}-e^{-\alpha\xi})\frac{e^{jkR'}}{4\pi R'}d\xi+\frac{\partial^2}{\partial y^2}\int_0^\infty(e^{-k\xi}-\eta^2e^{-\beta\xi})\frac{e^{jkR'}}{4\pi R'}d\xi\right\}+\\&\frac{\partial^2}{\partial x\partial y}\int_0^\infty(e^{-\alpha\xi}-\eta^2e^{-\beta\xi})\frac{e^{jkR'}}{4\pi R'}d\xi(l_y\hat{x}+l_x\hat{y})\Big]-\\&2jZ_0I\eta l_z\left(\frac{\partial^2}{\partial x\partial z}\hat{x}+\frac{\partial^2}{\partial y\partial z}\hat{y}\right)\int_0^\infty e^{-\beta\xi}\frac{e^{jkR'}}{4\pi R'}d\xi+\\&2jZ_0\eta\hat{z}\left[l_x\frac{\partial^2}{\partial x\partial z}+l_y\frac{\partial^2}{\partial y\partial z}+l_z\left(\frac{\partial^2}{\partial x^2}+\frac{\partial^2}{\partial y^2}\right)\right]\int_0^\infty e^{-\beta\xi}\frac{e^{jkR'}}{4\pi R'}d\xi,\end{aligned} \tag{D.8}$$

where $\mathbf{E}^{is}(\mathbf{r},\mathbf{r}')$ is the electric field radiated from the image source and given in (D.6), and $\mathbf{E}^{es}(\mathbf{r},\mathbf{r}')$, is given by $\frac{2jkZ_0I\eta}{1+\eta}\frac{e^{jkR}}{4\pi R}(l_x\hat{x}+l_y\hat{y})$, and can be interpreted as the electric field radiated from an electrostatic image source.

To further simplify the diffracted field expressions in (D.8) consider the integral, $I=\int_0^\infty e^{-p\xi}\frac{e^{jkR'}}{4\pi R'}d\xi$. Integrating I by parts, and using the identity $\frac{\partial}{\partial\xi}\frac{e^{jkR'}}{4\pi R'}=j\frac{\partial}{\partial z}\frac{e^{jkR'}}{4\pi R'}$, an analytic

expression, in terms of the derivative of I with a respect to z is obtained:

$$I = -\frac{1}{p}\int_0^\infty \frac{e^{jkR'}}{4\pi R'}\frac{\partial}{\partial \xi}e^{-p\xi}d\xi = \frac{1}{p}\left(\frac{e^{jkR}}{4\pi R} + j\frac{\partial I}{\partial z}\right). \tag{D.9}$$

Therefore,

$$\frac{\partial I}{\partial z} = j\frac{e^{jkR}}{4\pi R} - jpI. \tag{D.10}$$

Taking the derivative of (D.9) with respect to z and using (D.10), it can easily be shown that

$$I = \left(j\frac{\partial}{\partial z} + p\right)\frac{e^{jkR}}{4\pi R} - p^2 I \tag{D.11}$$

In a source free region, according to the Helmholtz equation, $\left(\frac{\partial^2}{\partial x^2} + \frac{\partial^2}{\partial y^2} + \frac{\partial^2}{\partial z^2} + k^2\right)\frac{e^{jkR'}}{4\pi R'} = 0$. This expression can be used to simplify (D.8) by replacing expressions containing $\frac{\partial^2}{\partial x^2} + \frac{\partial^2}{\partial y^2}$ with $-\frac{\partial^2}{\partial z^2} - k^2$. Applying the identities of (D.10) and (D.11), the first two lines in (D.8) are reduced to

$$-\left(\frac{\partial^2}{\partial z^2} + k^2\right) f_1(l_x\hat{x} + l_y\hat{y}) + \nabla_t\nabla_t\cdot(f_2\hat{l}), \tag{D.12}$$

where $\nabla_t = \frac{\partial}{\partial x}\hat{x} + \frac{\partial}{\partial y}\hat{y}$, $f_1 = \int_0^\infty (e^{-k\xi} - e^{-\alpha\xi})\frac{e^{jkR'}}{4\pi R'}d\xi$, and $f_2 = \int_0^\infty (e^{-\alpha\xi} - \eta^2 e^{-\beta\xi})\frac{e^{jkR'}}{4\pi R'}d\xi$. In order to evaluate the $\frac{\partial^2}{\partial x\partial z}$ and $\frac{\partial^2}{\partial y\partial z}$ terms in (D.8), they are rewritten as

$$\begin{aligned}\left(\frac{\partial^2}{\partial x\partial z}\hat{x} + \frac{\partial^2}{\partial y\partial z}\hat{y}\right)\int_0^\infty e^{-\beta\xi}\frac{e^{jkR'}}{4\pi R'}d\xi &= \nabla_t\frac{\partial}{\partial z}\int_0^\infty e^{-\beta\xi}\frac{e^{jkR'}}{4\pi R'}d\xi \\ &= j\nabla_t\left(\frac{e^{jkR}}{4\pi R} - \beta\int_0^\infty e^{-\beta\xi}\frac{e^{jkR'}}{4\pi R'}d\xi\right).\end{aligned} \tag{D.13}$$

Applying (D.10) (D.11) to (D.12) and (D.13), the diffracted field expressions of (D.8), can

be expressed as

$$\begin{aligned}\mathbf{E}^d(\mathbf{r},\mathbf{r}') =& \mathbf{E}^{is}(\mathbf{r},\mathbf{r}') + \mathbf{E}^{es}(\mathbf{r},\mathbf{r}') - \\ & \frac{2jZ_0I\eta}{1-\eta^2}(l_x\hat{x}+l_y\hat{y})\left[(k-\alpha)\frac{e^{jkR}}{4\pi R} - (k^2-\alpha^2)\int_0^\infty e^{-\alpha\xi}\frac{e^{jkR'}}{4\pi R'}d\xi\right] + \\ & 2Z_0I\eta l_z\nabla\frac{e^{jkR}}{4\pi R} - 2jZ_0I\eta l_z\hat{z}\left[\beta\frac{e^{jkr}}{4\pi r} + (k^2-\beta^2)\int_0^\infty e^{-\beta\xi}\frac{e^{jkR'}}{4\pi R'}d\xi\right] + \\ & \frac{2jZ_0I\eta}{1-\eta^2}\nabla_t\nabla_t\cdot(f_2\hat{l}) - 2Z_0\eta\left[\hat{z}\nabla_t(\frac{e^{jkR}}{4\pi R}\hat{l}) + \beta\left\{l_z\nabla_t f_3 - \hat{z}\nabla_t\cdot(f_3\hat{l})\right\}\right],\end{aligned} \tag{D.14}$$

where $f_3 = \int_0^\infty e^{-\beta\xi}\frac{e^{jkR'}}{4\pi R'}d\xi$.

Now by applying the identity $\hat{l}\times(a\hat{x}-b\hat{y}) = b(l_z\hat{x}-l_x\hat{z}) + a(l_z\hat{y}-l_y\hat{z})$, the last term in (D.14) can be rewritten as

$$l_z\nabla_t f_3 - \hat{z}\nabla_t\cdot(f_3\hat{l}) = \hat{l}\times\left(\frac{\partial}{\partial y}\hat{x} - \frac{\partial}{\partial x}\hat{y}\right)f_3 \tag{D.15}$$

The final simplified form of the exact image expressions for the diffracted field from a small dipole of arbitrary orientation are given by,

$$\begin{aligned}\mathbf{E}^d(\mathbf{r},\mathbf{r}') =& \mathbf{E}^{is}(\mathbf{r},\mathbf{r}') + 2jkZ_0I\left[\frac{e^{jkR}}{4\pi R} - \alpha\int_0^\infty e^{-\alpha\xi}\frac{e^{jkR'}}{4\pi R'}d\xi\right](l_x\hat{x}+l_y\hat{y}) - \\ & 2jZ_0I\eta l_z\hat{z}\left[\left(j\frac{\partial}{\partial z}+\beta\right)\frac{e^{jkR}}{4\pi R} + (k^2-\beta^2)\int_0^\infty e^{-\beta\xi}\frac{e^{jkR'}}{4\pi R'}d\xi\right] + \\ & 2Z_0I\eta\hat{l}\times\left(\frac{\partial}{\partial y}\hat{x} - \frac{\partial}{\partial x}\hat{y}\right)\left[\frac{e^{jkR}}{4\pi R} - \beta\int_0^\infty e^{-\beta\xi}\frac{e^{jkR'}}{4\pi R'}d\xi\right] + \\ & \frac{2jZ_0I\eta}{1-\eta^2}\left\{\frac{\partial^2}{\partial x^2}l_x\hat{x} + \frac{\partial^2}{\partial y^2}l_y\hat{y} + \frac{\partial^2}{\partial x\partial y}(l_y\hat{x}+l_x\hat{y})\right\}\int_0^\infty(e^{-\alpha\xi}-\eta^2e^{-\beta\xi})\frac{e^{jkR'}}{4\pi R'}d\xi,\end{aligned} \tag{D.16}$$

where it is noted that the diverging exponential in the original expressions for the diffracted fields from a horizontal dipole, as well as the resulting static image charge that appeared from this expression has vanished in the final formulation given here.

BIBLIOGRAPHY

BIBLIOGRAPHY

[1] S. Tabbane, *Handbook of Mobile Radio Networks*, Artech House, Norwood, 2000.

[2] H. L. Bertoni, *Radio Propagation for Modern Wireless Systems*, Prentice-Hall, New Jersey, 2000.

[3] W. C.Y.Lee, *Mobil Communication Engineering*, McGRAW-HILL, New York, 1998.

[4] N. Blaustein, *Radio Propagation in Celluar Network*, Artech House, Boston, 2000.

[5] M. D. Yacoub, *Foundations of Mobile Radio Engineering*, CRC Press, Bocs Raton, 1993.

[6] Y. Karasawa and H. Iwai, "Formulation of Spatial Correlation Statistics in Nakagami-Rice Fading Environments," *IEEE Trans. Antennas Propagat.*, vol. 48, no. 1, pp. 12–18, January 2000.

[7] M. D. Yacoub, "Fading Diatributions and Co-Channel Interference in Wireless Systems," *IEEE Antennas and Propagation Magazine*, vol. 42, no. 1, February 2000.

[8] D. Didascalou J. Maurer and W. Wiesbeck, "Subway Tunnel Guided Electromagnetic Wave Propagation at Mobile Communications Frequencies," *IEEE Trans. Antennas Propagat.*, vol. 49, no. 11, pp. 1590–1596, November 2001.

[9] T. Tamir, "On Radio-Wave Propagation in Forest Environments," *IEEE Trans. Antennas Propagat.*, vol. AP-15, pp. 1967, November 1967.

[10] G.P.S. Cavalcante D.A. Rogers and A.J. Giardola, "Radio Loss in Forests Using a Model with Four Layered Media," *Radio Sci.*, vol. 18, no. 5, pp. 691–695, September-October 1983.

[11] M.A. Weissberger, "An Initial Critical Summary of Models for Predicting the Attenuation of Radio Waves by Trees," Tech. Rep. ESD-TR-81-101, EMC Analysis Center, Annapolis MD USA, 1982.

[12] S.A. Torrico and R.H. Lang, "Bistatic Scattering Effects from a Tree in a Vegetated Residential Environment," *Proc. of National URSI Meeting*, pp. 24–25, 1998.

[13] S.A. Torrico H.L. Bertoni and R.H. Lang, "Modeling Tree Effect on Path Loss in a Residential Environment," *IEEE Trans. Antennas Propagat.*, vol. 46, no. 6, pp. 872–880, June 1998.

[14] L. Linchun, "A New MF and HF Ground-Wave Model for Urban Areas," *IEEE Antennas and Propagation Magazine*, vol. 42, no. 1, February 2000.

[15] Y. Asano, "Proposed of Method for Estimating Received Signal Characteristics in Mobile Communication Environments," *IEEE Trans. Antennas Propagat.*, vol. 48, no. 4, pp. 539–546, April 2000.

[16] Y. Wang S. N. Safieddin and S. K. Chaudhuri, "A Hybrid Technique Based on Combining Ray Tracing and FDTD Methods for Site-Specific Modeling of Indoor Radio Wave Propagation," *IEEE Trans. Antennas Propagat.*, vol. 48, no. 5, pp. 743–754, May 2000.

[17] Y. C. Lin, *A Fractal-Based Coherent Scattering and Propagation Model for Forest Canopies*, Ph.D. thesis, University of Michigan, Ann Arbor, MI, 1997.

[18] K. Sarabandi, *Electromagnetic Scattering from Vegetation Canopies*, Ph.D. thesis, University of Michigan, Ann Arbor, MI, 1989.

[19] F. T. Ulaby R.K. Moore and A.K. Fung, *Microwave Remote Sensing Active and Passive*, Arthech House, Norwood, 1982.

[20] D. Polder and J.H. van Santen, "The Effective Permeability of Mixture of Solids," *Physica*, vol. 12, pp. 257.

[21] L. L. Foldy, "The Multiple Scattering of Waves," *Phys. Rev.*, vol. 67, pp. 107–119, 1945.

[22] A. Tavakoli K. Sarabandi and F.T. Ulaby, "Microwave Propagation Constant for a Vegetation Canopy at x-band," *Radio Sci.*, vol. 28, no. 4, pp. 549–588, 1993.

[23] L. Armand and E. Mougin, "Microwave Coherent Propagation in Cylindrical-Shape Forest Components: Interpretation of Attenuation Observation," *IEEE Trans. on Geoscience and Remote Sensing*, vol. 28, no. 3, pp. 315–324, May 1990.

[24] L.B.Felsen and N.Marcuvitz, *Radiation and Scattering of Waves*, Prentice-Hall, New Jersey, 1973.

[25] L. Brekhovskikh, *Waves in Layered Media*, Academic Press, New York, 1960.

[26] L. W. Li T. S. Yeo P. S. Kooi and M. S. Leong, "Radio Wave Propagation Along Mixed Paths Through a Four-Layered Model of Rain Forest: An Analytic Approach," *IEEE Trans. Antennas Propagat.*, vol. 46, no. 7, pp. 1098–1110, November 1998.

[27] G.P.S. Cavalcante and A.J. Giardala, "Optimization of Radio Communication in Media with Three Layers," *IEEE Trans. Antennas Propagat.*, vol. AP-31, no. 1, pp. 141–145, January 1983.

[28] S.S. Seker, "Radio Pulse Transmission along Mixed Paths in a Stratified Forest," *IEE Proceedings, Part H-Microwave, Antennas and Propagat.*, vol. 136, no. 1, pp. 13–18, February 1989.

[29] K. Sarabandi and T. Chiu, "Electromagnetic Scattering from Slightly Rough Surfaces with Inhomogeneous Dielectric Profiles," *IEEE Trans. Antennas Propagat.*, vol. 45, no. 9, pp. 1419–1430, September 1997.

[30] L.Tsang J.Kong and R.T.Shin, *Theory of Microwave Remote Sensing*, Wiley, New York, 1985.

[31] M. Abramowitz and I. A. Stegun, *Handbook of mathematical functions with formulas, graphs, and mathematical tables*, Wiley, New York, 1972.

[32] K. Sarabandi and P. Siquera, "Numerical Scattering Analysis for two Dimensional Dense Random Media: Characterization of Effective Permittivity," *IEEE Trans. Antennas Propagat.*, vol. 45, no. 5, pp. 858–867, April 1997.

[33] G.F. Carey and J.T. Oden, *Finite Elements*, Prentice-Hall, New Jersey, 1984.

[34] R. F. Harrington, *Time-Harmonic Electromagnetic Fields*, McGraw-Hill, New York, 1961.

[35] K. Sarabandi P.F. Polatin and F.T. Ulaby, "Monte Carlo Simulation of Scattering from a Layer of Vertical Cylinder," *IEEE Trans. Antennas Propagat.*, vol. 41, no. 4, pp. 465–475, April 1993.

[36] W.L.Stutzman and G.A. Thiele, *Antenna Theory and Design*, John Wiley, New York, 1981.

[37] A. Papoulis, *Probability, Random Variables, and Stochastic Process*, McGraw-Hill, New York, 1984.

[38] J. G. Proakis, *Digital Communications*, McGraw-Hill, New York, 1989.

[39] W.H. Press B.P. Flannery S.A. Teukolsky and W.T. Vetterling, *Numerical Recipes in C*, Cambrige University, Cambrige, 1988.

[40] W. C. Jakes, *Microwave Mobile Communications*, IEEE Press, New York, 1994.

[41] P. Enge and P. Misra, "Special Issue on Global Positioning System," *Proceedings of the IEEE*, vol. 87, no. 1, pp. 3–15, January 1999.

[42] U.S. Coast Guard, *Global Positioning System Standard Positioning Service Signal Specification*, 2nd Edition 1995.

[43] Y. C. Lin and K. Sarabandi, "Monte Carlo Coherent Scattering Model for Forest Canopies Using Fractal-Generated Trees," *IEEE Trans. on Geoscience and Remote Sensing*, vol. 37, no. 1, pp. 440–451, January 1999.

[44] M. A. Karam A. K. Fung and Y. M. M. Antar, "Electromagnetic Wave Scattering from Some Vegetation Samples," *IEEE Trans. on Geoscience and Remote Sensing*, vol. 26, no. 6, pp. 799–808, November 1988.

[45] P. L. E. Uslenghi, "The Backscattering Radar Cross Section of Long Thin Dielectric Bodies of Revolution on a Metal Plane," *Can. J. Phys.*, vol. 43, pp. 1164–1167, 1965.

[46] K. Sarabandi and I. Koh, "Effect of Canopy-Air Interface Roughness on HF-UHF Wave Propagation in Forest," *Accepted for publication in IEEE Trans. Antennas Propagat.*

[47] K. Sarabandi and I. Koh, "A Complete Physics-Based Channel Parameter Simulation for Wave Propagation in a Forest Environment," *IEEE Trans. Antennas Propagat.*, vol. 49, no. 2, pp. 260–271, February 2001.

[48] R. E. Collin, *Field Theory of Guided Waves*, IEEE Press, New York, 1990.

[49] R. Schiffer and K. O. Thielheim, "Light Scattering by Dielectric Needles and Disks," *J. Appl. Physics*, vol. 50, no. 4, pp. 2476 – 2483, April 1979.

[50] R. E. Collin and F. J. Zucker, *Antenna Theory*, McGraw-Hill, New York, 1969.

[51] M. Z. Win and R. A. Scholtz, "Ultra-wide Bandwidth Time-hopping Spread-spectrum Impulse Radio For Wireless Multiple-access Communications," *IEEE Trans. Commun.*, vol. 48, no. 4, pp. 679–691, April 2000.

[52] K. Sarabandi M. D. Casciato and I. Koh, "Efficient Calculation of the Field of a Dipole Radiating Above an Impedance Surface," *Accepted for publication in IEEE Trans. Antennas Propagat.*

[53] R. Coifman V. Rokhlin and S. Wandzura, "The Fast Multipole Method for the Wave Equation:A Pedestrian Prescription," *IEEE Antennas and Propagation Magazine*, vol. 35, no. 3, pp. 7–12, June 1993.

[54] E. Bleszynski M. Bleszynski and T. Jaroszewicz, "AIM: Adaptive integral method for solving large-scale electromagnetic scattering and radiation problems," *Radio Sci.*, vol. 31, no. 5, pp. 1225–1251, September - October 1996.

[55] N. Geng A. Sullivan and L. Carin, "Fast Multipole Method for Scattering form an Arbitrary PEC Target Above or Buried in a Lossy Half Space," *IEEE Trans. Antennas Propagat.*, vol. 49, no. 5, pp. 740–748, May 2001.

[56] S. G. Glisic and P. A. Leppanen, *Code Division Access Commnunications*, Kluwer Academic Publishers, Dordrecht, 1995.

[57] V. Rokhlin, "Rapid Solution of Integral Equations of Scattering Theory in Two Dimensions," *Journal of Computational Physics*, vol. 86, no. 2, pp. 414 – 439, 1990.

[58] W. C. Chew J. Jin C. Lu E. Michielssen and J. M. Song, "Fast Solution Methods in Electromagnetics," *IEEE Trans. Antennas Propagat.*, vol. 45, no. 3, pp. 533–543, March 1987.

[59] X. Sun and N. P. Pitsianis, "A Matrix Version of the Fast Multipole Method," *Siam Review*, vol. 43, no. 2, pp. 289–300, June 2001.

[60] S. Lin and D. J. Costello, *Error Control Coding: Fundamentals and Application*, Prentice-Hall, New Jersey, 1983.

[61] K.A. Michalski, "On the Effective Evaluation of Integrals Arising in the Sommerfeld Half-Space Problem," *IEE Proceedings, Part H-Microwave, Antennas and Propagat.*, vol. 132, no. 5, pp. 312–318, August 1985.

[62] I. S. Gradshteyn and I. M. Ryzhik, *Table of Integrals, Series, and Products*, Academic Press, New York, 2000.

[63] T. C. Chiu, *Electromagnetic Scattering from Rough Surface Covered with Short Branching Vegetation*, Ph.D. thesis, University of Michigan, Ann Arbor, MI, 1998.